5-2019

Computational modeling of cell mechanics and binding kinetics at T-cell interfaces

Robert Henry Pullen III
University of Tennessee

To the Graduate Council:

I am submitting herewith a dissertation written by Robert Henry Pullen III entitled "Computational modeling of cell mechanics and binding kinetics at T-cell interfaces." I have examined the final electronic copy of this dissertation for form and content and recommend that it be accepted in partial fulfillment of the requirements for the degree of Doctor of Philosophy, with a major in Chemical Engineering.

Steven M. Abel, Major Professor

We have read this dissertation and recommend its acceptance:

Francisco Barrera, Eric T. Boder, Manolis Doxastakis

Accepted for the Council:

Dixie L. Thompson

Vice Provost and Dean of the Graduate School

(Original signatures are on file with official student records.)

Computational modeling of cell mechanics and binding kinetics at T-cell interfaces

A Dissertation Presented for the

Doctor of Philosophy

Degree

The University of Tennessee, Knoxville

Robert Henry Pullen, III

May 2019

To my parents and sister.

Thank you for your constant reinforcement and support.

Acknowledgements

I would like to thank my advisor, Dr. Steve Abel, for helping my professional development. I truly believe that over the course of my graduate research, I can now convey scientific information in a readily digesitible manner for a wide range of audiences thanks to your help. I will be sure to remember many of your pieces of advice as I continue foward. On a side note, two of my favorites are "Follow your heart . . . " for kinetic parameterization and "If you must include an outline slide in your presentation, do not put the term 'outline' on the slide itself."

Within the Abel research group, I have been able to work with great undergraduate and graduate students during my time here in Knoxville. In particular, Sina Mirzaeifared, Dr. Tyler Cosby, Dr. Paul Mlynarczyk, and Dr. Aaron Prescott helped me navigate through many research problems and greatly accelerated my technical skills, especially during the early tenure of my graduate school career. I would like to thank all my friends from Maryland and Tennessee as well as my family for their support, and ensuring I kept some appreciable sense of sanity.

Ten years ago if you told me I would complete a dissertation that primarily focuses on the integration of biology and computational methods in Knoxville, TN, I would have most likely smiled and nodded along. This of course would be my attempt to hide the fact I'm actively trying to leave the conversation as soon as possible because I was clearly engaging with someone out of whack. I was relatively uninterested in biology and had trouble with all computer-related tasks throughout high school. And I sure as hell didn't know much about Knoxville, TN. But, that all changed very quickly.

Going to the Volunteers football season-opener in August 2013 completely changed my perspective on the Knoxville community. Walking outside on a Saturday and joining a sea of easily 150,000 Vols fans in orange was both inspirational and an atmosphere that I will never forget. I knew right then that attending the University of Tennessee in pursuit of my doctoral

degree would not only lend itself to career advancement opportunities, but also lead to a great deal of fun on Fall weekends. Attending graduate school and becoming a Vols fan has really ingrained me within this community on a level that I had never experienced. These last several years were truly unforgettable and I am happy to look forward to the next chapter in my life. I would like to thank the National Institute of Mathematical and Biological Synthesis, the National Science Foundation, and the University of Tennessee for their financial support of this research. As always, Go Vols!

Abstract

T cells orchestrate adaptive immunity, yet how they recognize and respond to small numbers of antigenic ligands remains an open question. T cells use surface receptors (TCRs) to engage membrane-presented ligands (pMHCs) on antigen-presenting cells (APCs). Recent experiments have illuminated the significance of mechanical forces, spatial organization, and dynamics of key proteins at cell-cell interfaces in immunology. For example, studies have shown T cells use actin-based microvillar protrusions to actively search APCs and stimulatory TCR-pMHC bonds exhibit catch-bond behavior, with an average bond lifetime that initially increases with increasing tensile force. It is unclear how mechanical forces at the cell-cell interface and force-dependent TCR-pMHC dissociation kinetics regulate antigen discrimination. Experimental observations raise the interesting question of whether T cells can exploit catch-bond behavior of stimulatory bonds as a physical mechanism in the search of rare antigenic ligands.

In this dissertation, we employ computational methods to explore (i) the impact of TCR-pMHC bond formation on the spatial organization and shape of membranes at the cell-cell interface, (ii) the dynamics of TCR cluster formation, and (iii) the mechanical feedback between receptor-ligand binding and active force generation by scanning T-cell microvilli. We find the formation of individual TCR-pMHC bonds drives changes in the membrane organization and shape, leading to time-dependent forces on TCR-pMHC bonds. Using force-dependent lifetime data for TCRs bound to various ligands, we show that stimulatory catch bonds have a markedly enhanced average lifetime compared with non-stimulatory pMHCs. By varying the fraction and density of agonist pMHC on APCs, we demonstrate that stimulatory pMHC molecules play a central role in the formation of TCR clusters, and that TCR-pMHC clustering drives longer surface molecules away from regions of close apposition. Lastly, we find that a small number of catch bonds can initially immobilize T-cell microvilli, after which additional bonds accumulate and

increase the cumulative receptor-engagement time. Thus, catch bonds can selectively slow and stabilize scanning microvilli, suggesting a physical mechanism that may contribute to antigen discrimination by T cells. Taken together, our results highlight the importance of force-dependent binding kinetics and cell mechanics for antigen discrimination at the T-cell-APC interface.

Table of Contents

1 Introduction **1**

1.1 Overview of T-cell biology . . . 1

1.1.1 Classes of T cells . . . 1

1.1.2 T-cell development . . . 2

1.1.3 Major histocompatibility complex (MHC) and the T-cell receptor (TCR) . . . 3

1.2 Important experiments in T-cell mechanobiology . . . 4

1.2.1 Catch bonds, forces, and mechanisms at the receptor-ligand level . . . 5

1.2.2 Forces and spatial organization at the immunological synapse . . . 12

1.2.3 T-cell microvilli . . . 16

1.3 Instrumentation pertinent to T-cell mechanobiology . . . 18

1.3.1 Biomembrane Force Probe (BFP) . . . 19

1.3.2 Optical Trap / Tweezers (OT) . . . 19

1.3.3 Lattice Light-Sheet Microscopy (LLS) . . . 20

1.3.4 Supported Lipid Bilayers (SLBs) and Giant Unilamellar Vesicles (GUVs) . . . 20

1.3.5 Molecular tension-based fluorescence microscopy . . . 20

1.3.6 Single-Molecule Localization Microscopy (SMLM) . . . 21

1.3.7 Atomic Force Microscopy (AFM) . . . 22

1.3.8 Traction Force Microscopy (TFM) . . . 22

1.4 Model Formulation . . . 23

1.4.1 Gillespie Algorithm . . . 23

1.4.2 Membrane Energetics . . . 24

1.4.3 Metropolis Monte Carlo Scheme . . . 25

1.4.4 Time-dependent Ginzburg-Landau Model . . . 26
1.4.5 Advection-diffusion Equations . . . 27
1.5 Thesis Outline . . . 28
1.5.1 Catch bonds at T-cell interfaces: Impact of spatial reorganization and membrane fluctuations (Ch. 2) . . . 28
1.5.2 Dynamics of T-cell receptor cluster formation (Ch. 3) . . . 29
1.5.3 Mechanical feedback enables catch bonds to selectively stabilize scanning microvilli at T-cell surfaces (Ch. 4) . . . 29
1.5.4 Eph-A2 receptor clustering (Ch. 5) . . . 30

2 Catch bonds at T-cell interfaces: Impact of spatial reorganization and membrane fluctuations 31
2.1 Introduction . . . 31
2.2 Methods . . . 34
2.2.1 Membrane dynamics . . . 34
2.2.2 Monte Carlo simulations . . . 35
2.2.3 Bond tension and survival probability . . . 36
2.3 Results . . . 37
2.3.1 Bond formation drives membrane reorganization . . . 37
2.3.2 Bonds experience a time-dependent tension with fluctuations driven by membrane shape fluctuations . . . 38
2.3.3 Catch bonds enhance binding times . . . 39
2.3.4 The distance between bonds impacts bond tensions and survival probabilities 40
2.4 Discussion . . . 42
2.5 Conclusion . . . 44

3 Dynamics of T-cell receptor cluster formation 46
3.1 Introduction . . . 46
3.2 Model formulation . . . 47
3.2.1 Membrane dynamics . . . 47
3.2.2 Receptor-ligand dissociation kinetics . . . 48

3.2.3 Coupling of the TDGL model with reaction-diffusion equations 48
3.3 TCR cluster formation is highly dependent on the fraction of agonist pMHC molecules 50

4 Mechanical feedback enables catch bonds to selectively stabilize scanning microvilli at T-cell surfaces 52
4.1 Introduction 52
4.2 Methods 54
4.2.1 Computational framework 54
4.2.2 TCR-pMHC binding kinetics 56
4.3 Results 57
4.3.1 Scanning microvilli are slowed in a ligand-dependent manner 57
4.3.2 Heterogeneity of microvillus trajectories 57
4.3.3 Catch bonds stabilize microvilli 58
4.3.4 Catch bonds impact cumulative TCR-pMHC binding times 59
4.4 Discussion 60
4.4.1 Choice of the velocity profile, V_{MV} 61
4.4.2 A physical mechanism for microvillar stabilization and enhanced antigen discrimination 62

5 Dynamics of EphA2 receptor clustering 64
5.1 Receptor clustering 64
5.2 EphA2 receptor introduction 65
5.3 Model formulation 66
5.4 Parameterization of the model and sensitivity analysis 67
5.5 Time-dependence of EphA2 species fractions 68
5.6 TYPE7 titration characterization 68
5.7 Discussion 69

6 Future Directions 70
6.1 Evaluating the timescale necessary to distinguish an infected cell 70

6.2 Two-dimensional EphA2 receptor clustering model 71
6.3 Imposing shear flows on the T-cell / antigen-presenting cell interface 71

Bibliography **73**

Appendices **91**

A Introduction: Tables and Figures 92
B Catch bonds at T-cell interfaces: Tables and Figures 93
B.1 Supporting Material 106
C Dynamics of T-cell receptor cluster formation: Tables and Figures 110
D Scanning microvilli at T-cell surfaces: Tables and Figures 115
D.1 Supporting Material 124
E Dynamics of EphA2 receptor clustering: Tables and Figures 132

Vita **141**

List of Tables

B1 Model variables and parameters. 93

B2 Average force ($\langle f \rangle$) and standard deviation (σ) on a bond given that a second bond is located a fixed distance away. The averages and standard deviations are calculated for $t > 0.5$ s. Forces reported without a standard deviation are the average force at the final time point (1 s) of simulations without thermal fluctuations. 94

B3 Average force ($\langle f \rangle$) and standard deviation (σ) on edge bonds and the center bond in a configuration with three colinear bonds. The separation distance is the distance between each edge bond and the center bond. The averages and standard deviations are calculated for $t > 0.5$ s. 95

B4 Receptor-ligand binding kinetics for TCR-pMHC complexes given Bell and two-pathway models. 106

C1 Parameters used in the TDGL hybrid model. 110

D1 Parameters used in the model. 115

D2 Parameterization of TCR lifetime data 125

D3 Average $\pm$ SD for the microvillus velocity, bond lifetimes, and number of bonds for systems with VSV8 (A), OVA (B), and strong slip (C). All values are calculated from 25 independent trajectories. 131

E1 EphA2 model variables and parameters. PS denotes parameter sweep. 132

List of Figures

A.1 TCR-CD3 complex. The TCR has an α and β chain, each of which contain a variable domain, constant domain, and short transmembrane tail. The α and β chains are linked by a disulfide-bridge. The CD3$\delta\varepsilon$, CD3$\gamma\varepsilon$, and CD3$\zeta\zeta$ chains comprise the CD3 complex and associate with the TCR. ITAMs are located on each CD3 chain and are phosphorylated by kinases, e.g. Lck and ZAP70, upon TCR engagement with a ligand. Negative charges in the CD3 chains interact with the positve charges of the TCR. This figure is adapted from Wikimedia Commons. 92

B.1 Force-dependent lifetime data (points) for the OT1 TCR bound to three different ligands. Data points are from Liu et al. (76). OVA and A2 exhibit catch-bond behavior. Solid lines are nonlinear least squares fits to the data using Eqn. 2.1 for E1 and Eqn. 2.2 for OVA and A2. 96

B.2 Characteristic response to the formation of a bond (with thermal fluctuations). (A) Snapshots of the surface molecule concentration (top row) and the intermembrane distance (bottom row) with $\kappa = 12.15\ k_{\mathrm{B}}T$. Each column corresponds to a different time point. The bond is located at the center of the domain. (B) Kymographs of C_{SM} and z from a one-dimensional slice containing the bond. 97

B.3 Time evolution of the effective diameter (d) of the depletion zone. Data is averaged over ten independent trajectories for each condition. Simulations with thermal fluctuations (solid lines) lead to a more rapid expansion of the depletion zone than simulations without thermal fluctuations (dashed lines). Increasing the membrane stiffness, κ, promotes the formation of a larger depletion zone. 98

B.4 Average bond tension as a function of time. The average tension at each time point is calculated by averaging the tension from ten independent simulation trajectories with $\kappa = 12.15\ k_B T$ (blue) and $\kappa = 40\ k_B T$ (green). The cases without fluctuations are shown in darker shades. 99

B.5 Gaussian fits of the probability densities for the mean-centered forces obtained from simulations with and without surface molecules present. Results are shown for $\kappa = 12.15\ k_B T$ (blue) and $\kappa = 40\ k_B T$ (green). Histograms of mean-centered force data are included as insets for cases with (solid) and without (dashed) surface molecules. Each condition uses data from ten trajectories, with forces for $t > 0.5$ s used when surface molecules are present. 100

B.6 Survival probabilities for different ligands. Each survival probability curve is calculated by averaging ten independent survival curves. Different ligands (OVA, A2, and E1) are considered with (solid) and without (dashed) thermal fluctuations. (A) Survival probabilities with zero applied force. In this case, the slip bond (E1) exhibits the longest average lifetime. (B) Survival probabilities with $\kappa = 12.15\ k_B T$. (C) Survival probabilities with $\kappa = 40\ k_B T$. 101

B.7 Characteristic response to the formation of two bonds separated by 160 nm (with thermal fluctuations). (A) Snapshots of C_{SM} (top row) and z (bottom row) with $\kappa = 12.15\ k_B T$. Each column corresponds to a different time point. (B) Kymographs of C_{SM} and z from a one-dimensional slice containing both bonds. 102

B.8 Time evolution of the effective diameter (d) of the depletion zone for two bonds separated by different distances. Data is averaged over ten independent trajectories for each condition. (A) $\kappa = 12.15\ k_B T$. (B) $\kappa = 40\ k_B T$. 103

B.9 Average force on a bond when a second bond is a fixed distance away. Results with (solid) and without (dashed) thermal fluctuations are shown for $\kappa = 40\ k_B T$. For each case, data is averaged over ten independent trajectories. The average bond tension increases with increased separation. 104

B.10 Fraction of bonds that remain at $t = 1$ s as a function of bond separation distance. Rows correspond to different ligands (OVA, A2, and E1) and columns correspond to different values of κ. Results with (diamonds) and without (squares) fluctuations are shown. The values of ϕ reported with a separation distance of zero correspond to a single bond. All other cases have two bonds. For every condition tested, the catch bonds have a larger binding fraction that the slip bond. 105

B.11 Maximum time step as a function of the compressional stiffness (k_p) given a lattice spacing of 10 nm. 107

B.12 Characteristic response to the formation of a bond without thermal fluctuations. (A) Snapshots of C_{SM} (top row) and z (bottom row) with $\kappa = 12.15\ k_B T$. Each column corresponds to a different time point. The bond is located at the center of the domain. (B) Kymographs of C_{SM} and z from a one-dimensional slice containing the bond. 108

B.13 Ratio of the effective off rate to $k_{\mathrm{off}}(f_A)$ for different ligands. Solid lines are obtained by numerically integrating (Equation Number). Dashed lines are analytical results obtained in the limit $f \gg f_c$. (A) $\kappa = 12.15\ k_{\mathrm{B}}T$. (B) $\kappa = 40\ k_{\mathrm{B}}T$. 109

C.1 Initial intermembrane distance profile. The system size is 500 nm $\times$ 500 nm with a spatial discretization of 10 nm, which is commensurate with the footprint of a single TCR complex within the T-cell membrane (14). 111

C.2 Time evolution of the intermembrane distance profile given ρ_{pMHC} = 1000 molecules / $\mu\mathrm{m}^2$, ϕ_{VSV8} = 1.00. Clusters rapidly form due to the close proximity of the two apposed membranes and the high on-rate for stimulatory TCR-pMHC interactions. As time progresses, smaller clusters coalesce to form larger aggregates. By the final time point, only four clusters remain. 112

C.3 Average total number of bonds as a function of time and fraction of agonist pMHC given a constant pMHC molecule density of 1000 molecules / μm^2. Due to the close proximity and energetically favorable initial configuration of the two membranes, TCR-pMHC complexes rapidly accumulate at early times. The average number of TCR-pMHC complexes fluctuates about a constant value at longer-lived times. A total of five independent trajectories were sampled for each case. 113

C.4 The spatiotemporal evolution of TCR-pMHC complexes and CD45 phosphatases. TCR-pMHC complexes (white) coalesce over time and form separate protein domains from the longer CD45 surface molecules (red) within the intercellular junction. 114

D.1 Schematic of a T-cell microvillus scanning across the surface of an antigen-presenting cell. TCR-pMHC bonds stochastically form and dissociate as the microvillus moves across the APC surface. The velocity, V_{MV}, depends on the force exerted on the microvillus tip by TCR-pMHC complexes. (A) Side view of the system with the T-cell microvillus tip residing above the APC surface. (B) Top-down view. The microvillus moves in the x-direction. A mixed population of pMHC is shown; some form catch bonds upon binding TCRs while others form slip bonds. 116

D.2 Average TCR-pMHC lifetimes as a function of tensile force. Curves for VSV8, OVA, and slip were fit using nonlinear least square fits of experimental data from Refs. (76) and (37). The "strong slip" bond is a hypothetical control with the same maximum average lifetime as VSV8 and the same reference force as the slip bond. 117

D.3 The average microvillus displacement for different fractions of stimulatory pMHC: (A) VSV8, (B) OVA, and (C) strong slip. Each line shows the average displacement from 25 independent trajectories. 118

D.4 Displacements of microvilli for (A) nonstimulatory pMHC, (B) 10% VSV8 pMHC, and (C) 30% VSV8 pMHC. Black lines show the average microvillus displacement calculated from 25 independent trajectories. Colored lines show the displacement of individual microvilli (10 shown). 119

D.5 (A) Probability density and cumulative distribution functions (inset) of the microvillus velocity at various fractions of VSV8 pMHC. (B) Probability density of the microvillus velocity at various fractions of strong-slip pMHC. Each distribution is constructed from the velocities obtained over the course of 25 independent trajectories. The green curve (0%) is the same on both figures. 120
D.6 The probability that a microvillus is immobilized ("stops") within 1 minute of scanning. A "stopping event" occurs when the average velocity is ≤ 0.25 μm/min for a continuous period of at least 10 s. Each point is obtained from 25 independent trajectories. 121
D.7 The number of catch and slip bonds (colored lines, right axes) and the microvillus displacement (black lines, left axes) for sample trajectories at three fractions of VSV8 pMHC (A-C). 122
D.8 The average cumulative time of receptor engagement for various systems: (A) VSV8 with stopped microvilli, (B) VSV8 with mobile microvilli, and (C) strong-slip pMHC. No stopping events were observed for the strong-slip case. 123
D.9 Displacements of microvilli for different fractions of strong-slip (A - C) and OVA (D - F) pMHC. Black lines show the average microvillus displacement calculated from 25 independent trajectories. Colored lines show the displacement of individual microvilli (10 shown). 127
D.10 (A) Probability density of the microvillus velocity at various fractions of OVA pMHC. (B, C) The average number of slip and catch bonds as a function of the microvillus velocity for the OVA system. 128
D.11 (A, B) The average number of nonstimulatory slip bonds as a function of the microvillus velocity for varying fractions of strong-slip and VSV8 pMHC. (C, D) The average number of strong-slip and catch bonds for the same systems. 129
D.12 Characterization of the velocity distribution for different forms of V_{MV} with 100% slip (A), 100% OVA (B), and 100% VSV8 (C). The linear response is considered with $f_{\mathrm{MV}} = 25$ pN and 100 pN (compared with $f_{\mathrm{MV}} = 50$ pN in the main text). The Hill-like response is considered with $F_{\mathrm{MV}} = 25$ pN and $n_{\mathrm{H}} = 4$. 130

E.1 Chemical species and binding interactions in the computational model. The EphA2 particle (monomer) has two binding surfaces that allow it to participate in dimer formation. Dimers that reversibly bind via the inactive interface (black) of the monomer cannot form larger aggregates. Dimers that reversibly bind via active monomer interface can participate in cluster formation. Cluster formation starts when two active dimers occupy adjacent lattice sites (red linker). TYPE7 binds to monomers via the inactive interface while leaving the active interface available for dimerization. Particles diffuse by hopping to neighboring lattice sites at a rate proportional to the diffusion coefficient. 133

E.2 EphA2 receptor clustering reaction coordinate diagram. This diagram relates the free energies of dimerization at the inacative and active interfaces as well as the free energy associated with the cluster reaction. Ephrin-A1 abrogrates the reaction via the inactive interface and thus forces the monomer to transition to the active dimer state. 134

E.3 Kinetic parameter sweep. This subset of the parameter sweep shows the average cluster fraction at a given parameter set after running one hundred independent trajectories. A desirable kinetic parameter set has a large difference in the cluster fraction between the TYPE7 = 0 and Ephrin cases (system limits). Cases that show significant differentiation between the two limits are highlighted in light green. . . 135

E.4 Sensitivity analysis. Analysis was performed observing changes of cluster fraction that occur when parameters are varied. Triangle symbols correspond to the sensitivity analysis and correspond to results when increasing (upward triangle) or decreasing (downward triangle) a kinetic parameter by ten percent of its original value. The dashed lines represent the cluster fraction obtained using the parameters in the table. The black line gives the cluster fraction when ephrin-A1 is present, and the orange line gives the final cluster fraction without ephrin-A1 or TYPE7. Each result corresponds to the average of one hundred independent trajectories. . . 136

E.5 Characterization of the effect of system size. We show the average cluster fraction of one hundred independent trajectories for the conditions considered in our study (solid lines) and for a system twice the size (dashed lines). The black vertical line at 3 minutes indicates the time at which TYPE7 peptides or ephrin-A1 ligands are introduced into the system. Doubling the system size does not significantly change the average cluster fraction for a given TYPE7 peptide density. 137

E.6 Time-dependent chemical species fractions given the presence of ephrin-A1. The average chemical species fraction $\pm$ S.D. of each chemical species are shown. The black vertical line at 3 minutes indicates the time at which ephrin-A1 ligands are introduced into the system. Each result corresponds to the average of one hundred independent trajectories. 138

E.7 Time-dependent chemical species fractions given the a TYPE7 peptide density of 41 molecules/μm^2. The average chemical species fraction $\pm$ S.D. of each chemical species are shown. The lack vertical line at 3 minutes indicates the time at which ephrin-A1 ligands are introduced into the system. Each result corresponds to the average of one hundred independent trajectories. 139

E.8 EphA2 receptor clustering is dependent on the number of TYPE7 peptides present in the system. (A) Average cluster fractions as a function of time and TYPE7 peptide number. Averages were obtained from one hundred independent trajectories. (B) Time-dependence of cluster fractions for individual trajectories. The black vertical line at 3 minutes indicates the time at which TYPE7 peptides or ephrin ligands are introduced into the system. There is significant variation between individual trajectories at lower TYPE7 peptide densities due to the stochastic nature of the model. 140

Chapter 1

Introduction

1.1 Overview of T-cell biology

T cells are a type of immune cell that orchestrate an adaptive immune response after exposure to a stimulatory antigen (antibody generator). The adaptive immune response is vital to the elimination of foreign pathogens that have evaded the innate immune response. T cells directly interact with target cell surfaces and must reliably recognize antigenic ligands in a sea of non-stimulatory ligands. How T cells are able to efficiently scan and issue an appropriate response to rare encounters of antigen remains an important, open question in the field of immunology.

1.1.1 Classes of T cells

T cells are able to differentiate into four main subsets: cytotoxic, helper, memory, and regulatory cells, each of which has a separate function in mediating the adaptive immune response (41). Cytotoxic T cells are most easily identified through the expression of a surface molecule, the CD8 co-receptor and directly interact with a target cell (28). When they identify an infected cell, they induce its death usually by (i) release of lytic granules into the target cell's cytosol after the formation of an immunological synapse (IS) (124) or (ii) initiating an apoptotic signaling cascade within the target cell (26). Helper T cells are identified through the expression of the CD4 co-receptor. They help activate B cells, macrophages, and cytotoxic T cells to destroy pathogens. An essential aspect of the adaptive immune system is its ability to efficiently coordinate a response to

previously encountered antigens. Memory cells are a small subset of T cells originating from T cells that have encountered antigen. They remain present within the body after the initial immune response, typically for the rest of the organism's life. Memory cells have an increased affinity for the same antigen such that if it is ever encountered again, the memory cells can quickly orchestrate an adaptive immune response. Lastly, regulatory T cells function to suppress other T cells as a means to prevent autoimmune diseases by over-reactivity.

1.1.2 T-cell development

Lymphocytes are a subset of white blood cells that are responsible for immune responses. An important task for the immune system is to distinguish the difference between 'self' and 'foreign'. The major histocompability complex is a molecule that displays peptides derived from their own proteins (self-pMHC) and foreign pathogens. T cells are derived from a common lymphoid progenitor, which can differentiate into a B, T, or natural killer cell. T cells are developed in the thymus, a central lymphoid organ. Within the thymus, T cells are exposed to self-pMHC complexes and must interact appropriately in order to avoid apoptosis and eventually circulate within the body (65). In the cortex of the thymus, the T-cell receptor on a T cell first must weakly bind to self-pMHC complexes, which is indicative that the T-cell receptor is capable of binding to a foreign pathogen displayed on the surface of a target cell (positive selection) (49, 91). Next, surviving thymocytes move to the medulla of the thymus, where they interact with dendritic cells or macrophages. Negative selection eliminates developing T cells whose T-cell receptors bind too strongly with presented self-pMHC complexes (15). Strong interactions are indicative of autoreactive T cells, which could cause autoimmunity diseases if left unchecked (6, 117). It is thought that the MHC molecule that induced positive selection causes the thymocyte to differentiate and express a particular co-receptor on its cell surface, i.e. CD4 or CD8. The combination of these two selection processes permits only 2% of developing thymocytes to leave the thymus, while the others are ingested by macrophages (92).

1.1.3 Major histocompatibility complex (MHC) and the T-cell receptor (TCR)

Major histocompatibility complexes (MHC) are highly polymorphic and sorted into two groups, MHC classes I and II. MHC class I molecules are recognized by cytotoxic T cells (CD8+) while MHC class II molecules are recognized by helper T cells (CD4+). The main differentiator between the two classes of molecules is the cleft within the MHC molecule that binds to peptide fragments (61). MHC class I molecules bind smaller peptides ($\sim 8-10$ amino acids), and aligns them along the MHC-$\alpha 1\alpha 2$ domains. MHC class II molecules have a larger peptide-binding cleft, and bind to peptides that are at least 13 amino acids in length.

T-cell receptors (TCRs) recognize antigen in the form of a processed peptide fragment (peptide-MHC) that is presented on the surface of a professional antigen-presenting cell, such as a mature dendritic cell. The T-cell receptor is composed of an α and β chain that are interconnected by a disulfide bridge. Each chain contains a variable domain, a constant domain that anchors the molecule in the membrane, and a transmembrane region that associates with chains of the cluster of differentiation 3 (CD3) complex (Fig. A.1) (142). *All tables and figures are placed in the Appendix*. The two variable domains, V_α and V_β, contain six hypervariable loops, which form three complementarity-determining region (CDR) loops that provide the center of the antigen-binding site and contact the peptide fragment (110). The structural combination of these CDR loops shapes the receptor-ligand binding interface and determines antigen specificity.

T-cell signaling plays a crucial role in the translation of receptor-mediated interactions at the cell-cell interface to a cellular response. T-cell activation occurs after the phosphorylation of immunoreceptor tyrosine-based activated motifs (ITAMs) on the cytoplasmic domains of the TCR-CD3 complex. The CD3 complex is comprised of two heterodimers (CD3$\delta\varepsilon$ and CD3$\gamma\varepsilon$) and one homodimer (CD3$\zeta\zeta$) that interacts with the TCR to form the TCR-CD3 complex (73). The cytoplasmic CD3ζ chains each contain three ITAMs while the two heterodimers, CD3$\delta\varepsilon$ and CD3$\gamma\varepsilon$ each contain one ITAM. Phosphatases are molecules that dephosphorylate proteins, thereby returning them to their inactive state. The balance between kinases and phosphatases in the local environment surrounding TCR-CD3 complexes modulates the phosphorylation state of a TCR-pMHC complex. Upon TCR-pMHC engagement, Lck, a protein kinase, is recruited to

the TCR-CD3 complex and phosphorylates CD3ζ chains of the TCR complex (5). This in turn, recruits an additional kinase, ZAP70, which phosphorylates LAT, a scaffold protein, and SLP-76, an adaptor protein (103). This leads to further downstream signaling results in an increase in the flux of intracellular calcium and the activation of the transcription factors (NFκB, NFAT, and AP-1). Together, this induces T-cell proliferation and differentiation.

1.2 Important experiments in T-cell mechanobiology

Mechanobiology is a rising field that focuses on how the interplay of forces and physical properties of the environment influence a biological system. With the advancement of instrumental techniques, research groups have been able to investigate how mechanical properties couple to immune cell biology. In particular, T-cell mechanobiology has progressed considerably over the past decade from the initial discovery that the T-cell receptor actuates as an anisotropic mechanosensor to the emerging understanding that forces at the cell-cell interface play a role in directing the overall response from the adaptive immune system (69). Novel experimental techniques and computational frameworks have illuminated the forces, spatial organization, and dynamics of key proteins at the interface between a T cell and antigen-presenting cell. Here, we discuss the findings of recent publications that have advanced the field and understanding of T-cell mechanobiology.

Taken together, these experiments show TCR-pMHC complexes exhibit different binding kinetics given the presence of a stimulatory or non-agonist pMHC. Ensuing mechanisms after the initial cell-cell contact, including TCR-pMHC conformational changes, TCR microcluster aggregation, downstream signaling cascades, and the coupling of the underlying actin cytoskeleton, work in tandem to discriminate antigen and orchestrate an appropriate immune response.

1.2.1 Catch bonds, forces, and mechanisms at the receptor-ligand level

"Accumulation of dynamic catch bonds between TCR and agonist peptide-MHC triggers T-cell signaling"

The Zhu group used a biomembrane force probe (BFP) to investigate force-dependence of TCR-pMHC bond lifetimes (76). By testing a panel of ligands of varying stimulatory strength for several constant forces, they found that the bond lifetimes of non-agonist TCR-pMHC complexes reached a maximum when no force was applied. The strictly monotonic decrease of non-stimulatory bond lifetimes as a function of applied tensile force is commonly referred to as slip-bond behavior. However, when applying tensile forces to stimulatory TCR-pMHC systems, they observed catch-bond behavior in that the bond lifetime initially increases with an applied force until it is maximized at some nonzero force before subsequently decaying. This experiment was the first, direct observation that agonist pMHC molecules resulted in catch-bond behavior.

To test how downstream signaling is influenced by the stimulatory strength of a ligand, the researchers measured intracellular Ca^{2+} release using fura-2 ratiometric imaging under a range of constant forces. Interestingly, the Ca^{2+} release as a function of applied force closely matched the catch- or slip-bond lifetime behavior. Shorter-lived binding events, with intermediate tensions ($F \leq 15$ pN), were sufficient to induce Ca^{2+} signaling. This and the observation that the cumulative bond lifetime of TCR-pMHC complexes best correlated with Ca^{2+} release suggests that long bond lifetimes may not be needed to generate Ca^{2+} signaling.

"A TCR mechanotransduction-signaling loop induces negative selection in the thymus"

Hong et al. explored whether catch- and slip-bond behavior played a role in the development of T cells, particularly with regards to positive or negative selection (50). In the thymus, T cells are positively selected if they are able to appropriately interact with self-antigens to produce a "survival" signal. Negative selection leads to apoptosis of T cells that interact too strongly with self-antigen to ensure removal of potential autoimmune cells.

The experimentalists used a biomembrane force probe to measure the force-dependent receptor-ligand kinetics of CD4+CD8+ double-positive (DP) thymocytes. The bead was coated with wild-type H2-K^b MHC or a mutant H2-$K^b\alpha$3A2 MHC, which completely abrogated CD8

co-receptor binding. The interaction between strong agonist peptides presented by wild-type MHC and OT1 TCRs resulted in catch bonds. TCR interactions with all H2-K$^b\alpha$3A2-presented ligands resulted in slip-bond behavior. To test the role of co-receptor kinase signaling and its impact on TCR-pMHC bond lifetimes, the group treated cells with an Lck inhibitor. Upon treating OT1.CD8.4 thymocytes with an Lck inhibitor, catch bonds converted to slip bonds implying that Lck signaling likely modulates the CD8-dependent conversion of the TCR-pMHC slip bond to a catch bond.

DP thymocytes were then placed on glass coverslips bearing pMHC tagged with 13-pN molecular tension probes. By testing a panel of negative- and positive selection peptides, they found increased and longer-sustained fluorescence in negative selection ligands for the molecular tension probe experiments. This supports the notion that thymocytes exert a higher-sustained force given the presentation of a negative selection ligand. Interestingly, all negative selection peptides were observed to contain catch-bond behavior whereas positive selection peptides exhibited slip-bond behavior. If the T cell imparts endogenous forces onto a TCR-pMHC complex, catch bonds are more likely to withstand the forces. This translates into a longer-preserved signal that could directly influence the differentiation of the DP thymocyte.

"Mechano-regulation of peptide-MHC class I conformations determines TCR antigen recognition"

To investigate the structural mechanism of 2C TCR-H-2K^b catch bonds, Wu et al. used a combined approach of computational methods (molecular dynamics) and single-molecule experiments with a biomembrane force probe (BFP) (144). Using steered molecular dynamics, they found that applying a normal force to the bond interface increased the frequency of hydrogen bonding between pMHC residues and CDR loops for agonist peptides, but not for antagonist peptides. This gave rise to the hypothesis that a small subset of key residues on the pMHC are required for forming catch bonds. To test this idea, they mutated an agonist peptide, R4, to an antagonist peptide, L4, via a single amino-acid substitution *in silico*, and found no hydrogen bonding formation or catch-bond characteristics. Performing the same experiment using BFP, they observed catch bonds and robustly stimulated IL-2 and IFN-γ release with R4-MHC unlike L4-MHC, which exhibited only slip bonds and no IL-2 release.

Steered molecular dynamics simulations also showed that an applied normal load to the TCR-pMHC complex resulted in a gradually extension and rotation of the MHC towards the CDR loops via intracellular breakup of the MHC $\alpha 1\alpha 2 - \beta 2$m domains. This applied force and subsequent extension of the MHC ($\sim 7 - 12$ nm) induced the formation of new H-bonds at the TCR-pMHC binding interface. BFP confirmed that a conformational change was indeed induced these agonist pMHC-TCR interactions with a MHC and TCR extensions of ~ 12 nm and ~ 2 nm, respectively. To test if the conformational change was indeed necessary for catch bond formation, the researchers tested a disulfide bond-locked R4 MHC mutant, which prevents extension of the MHC α chain. In agreement with previous simulations, they found that the resulting TCR-pMHC complex exhibited slip-bond behavior.

Taken together, these results indicate that a conformational change in the TCR-pMHC complex and subsequent formation of hydrogen bonds is necessary for catch-bond behavior. Given a sufficient applied tensile force, the length of the conformational extension in the TCR-pMHC complex (~ 15 nm) is in agreement with previous experiments (31). However, the underlying source for the conformational change is currently in contention whether it be extension of the TCR-β subunit or the MHC-α chain.

"Mechanosensing drives acuity of $\alpha\beta$ T-cell recognition"

The Lang laboratory uses optical tweezers (OT) to control the direction and magnitude of forces with high precision to T cells. Using OT, they can explore how T-cell activation is dependent upon the magnitude of the force, direction of the force, and the pMHC density on the probe bead. Feng et al. utilized OT to determine that in the absence of force, the chemical threshold to trigger T-cell activation requires an unphysiological number of pMHC molecules (37). However, the application of ~ 10 pN forces on TCR-pMHC complexes did result in TCR triggering for reasonable numbers of pMHC molecules. The optical trap was held in several configurations leading to forces on the TCR-pMHC complex in both normal and shear directions. The force-dependent conformational change of the TCR-pMHC complex was facilitated with an applied shear force as opposed to a normal-directed force. Accordingly, calcium signaling was maximized with an applied shear force, strongly suggesting that T-cell triggering is anisotropic under applied forces.

This anisotropic preference can possibly be explained by the underlying geometry of the TCR-pMHC complex in relation to the applied force. Under a normal-directional force, multiple receptor-ligand complexes would experience the same pulling force at the interface. However, an applied shear force unevenly distributes the force to TCR-pMHC complexes. This geometric argument supports the experimental data produced where (i) at low copy numbers of pMHC (2 agonist pMHC at the interface), both a shear and normal force cause TCR triggering, but (ii) at slightly higher pMHC numbers (29 agonist pMHC at the interface), only a shear force results in TCR triggering.

"Force-dependent transition in the T-cell receptor β-subunit allosterically regulates peptide discrimination and pMHC bond lifetime"

The TCR$\alpha\beta$ heterodimer contains a 12-residue-long insertion called the CβFG loop that is thought to play a role in T-cell activation, as deletion of the loop results in mitigated T-cell function (119, 135). Das et al. used an optical trap in single-molecule experiments on isolated single cells to investigate the CβFG loop and conformations of the TCR-pMHC complex under applied tensile force (31). Because the CβFG loop is structured solely by hydrogen bonds and lacks disulfide bonds, it was proposed that a sufficient tensile force might lead to an allosteric alteration within the TCR β-subunit.

After allowing bond formation between a T cell and pMHC-loaded bead, the optical trap held the bead at a fixed position leading to a constant tensile force on the TCR-pMHC bond. By using a variety of ligands, the researchers observed conformational transitions that were pMHC-dependent. Before bond rupture, non-agonist pMHC molecules showed a smaller conformational transition ($\sim$ 8 nm) in comparison to agonist pMHC molecules ($\sim$ 15 nm).

To assess if this conformational change could be attributed to the CβFG loop, Das et al. compared the wild-type TCR data with TCRs that had either a stabilized or deleted CβFG loop. Deletion of the CβFG loop caused a dramatic reduction in bond lifetime and a smaller conformational change, while stabilizing the CβFG loop resulted in a significantly increased bond lifetime, but abolished the conformational transition. Hence, the CβFG loop plays a critical role in relation to the conformational transition of the TCR-pMHC complex under an applied tensile

force. The proposed model suggests that the CβFG loop modulates the pMHC-dependent catch-bond behavior of the T-cell receptor by force-driven allosteric transitions.

"DNA-based nanoparticle tension sensors reveal that T-cell receptors transmit defined pN forces to their antigens for enhanced fidelity"

Liu et al. explored the range of forces that are commonly transmitted by individual TCR-pMHC complexes before T-cell activation using DNA-hairpin tension sensors (77). If the tensile force experienced by the receptor-ligand pair exceeded the force threshold of the DNA-hairpin sensor, the hairpin loop would break followed by a drastic increase in fluorescence. Using a combination of the tension probes and ratiometric fura-2 Ca^{2+} indicators, the researchers found that high tensions on TCR-pMHC complexes preceded Ca^{2+} release. These forces were highly co-localized with F-actin, myosin light chain kinase, and Lck indicating that actin dynamics and kinases / signaling likely play a role in actuating tensile forces.

Importantly, the force threshold of the DNA-hairpin sensors can be modified by the GC content within the hairpin loop. In particular, Liu et al. conducted experiments with 12-, 19-, and 56-pN sensors to gauge the tensile forces experienced by TCR-pMHC bonds as the T cell spread over a glass coverslip with pMHC-loaded gold nanoparticles (77). After engaging the surface for 15 minutes, naïve OT-1 T cells showed robust fluorescence only with the 12-pN probe surface. This signifies that T cells apply tensile forces on the TCR-pMHC complexes somewhere in the range of 12-19 pN. Using a mutant pMHC to block CD8 co-receptor binding or pretreating T cells with an Lck inhibitor eliminated measurable tension and cell spreading. Hence, both co-receptor binding and Lck are required to observe forces greater than 12 pN.

By testing a panel of ligands of varying stimulatory strength, the researchers observed the more potent ligands exhibited forces regularly exceeding 12 pN and enhanced T-cell triggering. It is interesting to note that given the multitude of cell-generated forces (cell motion, TCR-CD3 coupling to the actin cytoskeleton, thermal fluctuations, etc.) on TCR-pMHC complexes, the observed tensions lied within the same range where catch bond lifetimes are maximized.

"Monomeric TCRs drive T cell antigen recognition"

Previous observations have led some to the conclude that TCR oligomerization plays a role in antigen discrimination. Brameshuber et al. used several experimental techniques, each pertinent to a different timescale, to investigate the stoichiometry of the TCR-CD3 complex (18). Thinning out clusters while conserving stoichiometry of labeling (TOCCSL) measurements tracked the fluorescence of labeled TCRβ subunits and CD3ε-reactive KT3 antibodies. Their results show that naïve T cells chiefly consist of one TCRβ subunit and two CD3ε units, which follow the stoichiometry of monovalent TCR-CD3 complexes. However, it is important to note that TOCCSL is unable to account for the presence of short-lived protein complexes.

Thus, to ensure multimerized TCR-CD3 complexes were not transiently present, the group conducted photon-antibunching / fluorescence correlation spectroscopy (PA/FCS) experiments for increased temporal resolution. This experiment relates the characteristic timescales of a fluorescent excitation event to that of the light pulse. If the light pulse is shorter than the fluorescent lifetime, a single fluorophore can only emit one photon. Then, using FCS, the researchers are able to track the locations of the protein complexes. Fluorophores coming from the same complex, as would be the case for higher-order TCR oligomerization, would show correlated movements. In agreement with results from TOCCSL, PA/FCS did not indicate the presence of TCR-CD3 oligomers.

Despite these conclusions, both these experiments assume that the protein complex of interest is able to diffuse about the system. To account for the possibility that higher-order TCR-CD3 complexes are immobile, Brameshuber et al. conducted FRET between labeled TCR-engaged pMHCs on supported lipid bilayers with and without agonist pMHC (18). The authors measured FRET values at or below the threshold of random molecular encounters indicating the vast majority of immobile or TCR-engaged TCRs were monomeric. Taken together, these three independent experimental studies suggest that higher-order TCR-CD3 complexes have no role in antigen discrimination.

"Isolation of a structural mechanism for uncoupling T-cell receptor signaling from peptide-MHC binding"

Sibener et al. investigated differences in TCR-pMHC complexes that did or did not lead to T-cell triggering (125). The docking geometries of TCR-pMHC complexes that resulted in T-cell triggering were indistinguishable from TCR-pMHC complexes that did not lead to T-cell signaling. Thus, the crystal structure of a TCR-pMHC complex cannot be used to predict whether a given TCR-pMHC complex would cause TCR triggering. Agonist TCR-pMHC interactions, which exhibited catch-bond behavior, displayed a rapid rise in the intracellular Ca^{2+} flux followed by a decay, and strong ZAP70 recruitment at the center of the conjugate. Meanwhile, non-stimulatory TCR-pMHC interactions showed no significant increase in Ca^{2+} flux or aggregation of ZAP70. Using a GUV/SLB system, the authors found that the weak TCR signaling in non-agonist interactions led to limited CD45 phosphatase segregation. Therefore, ITAMs on the CD3ζ tails of the TCR-CD3 complex were unlikely to remain phosphorylated due to the proximity of phosphatases. Using this rationale, the authors proposed that catch bond formation may be able to sustain interactions between apposing cells leading to CD45 exclusion, and an intracellular shift in the kinase-phosphatase balance inducing T-cell activation.

"Early T-cell receptor signals globally modulate ligand:receptor affinities during antigen discrimination"

The Groves group examined how (i) single-molecule binding events influence the average of subsequent TCR-pMHC complex lifetimes and (ii) if the density of pMHC molecules impacted the observed bond lifetimes. After investigating a panel of TCRs and pMHCs, Pielak et al. found the maximum affinity for the interaction between a TCR and pMHC was reached at low pMHC densities, $\rho_{\text{pMHC}} \leq 10$ molecules/μm^2, regardless of the tested peptide or TCR (106). Interestingly, because the average mean dwell time of TCR-pMHC complexes was invariant across the tested pMHC densities, the researchers concluded that the kinetic binding rate is modulated in the TCR-pMHC interaction.

Drug inhibitory studies were used to find possible candidates that enhanced the on-rate of the TCR-pMHC interaction. In particular, they measured how titrating inhibitory drugs altered

the dissociation constant at the pMHC density corresponding to the highest TCR-pMHC binding affinity. Titration of LatA, which targets the actin cytoskeleton, and GGTI-298, which disrupts inside-out signaling of LFA-1, resulted in monotonic decreases of binding affinity. Thus, the actin cytoskeleton and / or LFA-1 may play a role in the enhancement of the binding rate. The authors propose the enhanced on-rate resulted from coupling of the first few binding events and TCR signaling, which induces a morphological change at the cell-cell interface. This positive feedback mechanism at low densities of pMHC enhances the ability of antigen discrimination by allowing multiple binding events to check for more antigens. Thereby, T cells can effectively slow down the antigen recognition process and allow for multiple measurements of a TCR-pMHC dwell time before ultimately initiating an immune response.

1.2.2 Forces and spatial organization at the immunological synapse

"Cytotoxic T cells use mechanical force to potentiate target cell killing"

Although previous studies have focused on the formation of the immunological synapse, the forces present at cytotoxic T cell (CTL)-target cell interfaces remain largely unknown. Basu et al. investigated how CTLs might employ forces at the immunological synapse to potentially enhance target cell killing. Perforin, PTEN, and Dock2 are a few proteins present at the IS which are central for the cytotoxic efficiency of a CTL (9). Perforin is a protein secreted by CTLs to disrupt and consequently induce the growth of membrane pores within the target cell membrane. These membrane pores are sufficiently large such that granzymes from lytic granules within the CTL can diffuse into the target cell cytoplasm and cause apoptosis. PTEN is a phosphatase that inhibits the kinase PI3K, which itself promotes F-actin polymerization within the IS by recruiting the Rho GTPase exchange factor Dock2.

To investigate the interplay between these molecules, Basu et al. transduced OT1 TCRs with short-hairpin RNA to silence gene expression of PTEN (shPTEN) and Dock2 (shDock2). Cells were then placed in a solution of propidium iodide (PI), which fluoresces after reaching the target cell cytoplasm, to quantify the delay between IS formation and perforin-induced membrane pore formation. The time difference between IS formation and PI fluorescence was approximately two-fold smaller for shPTEN CTLs in comparison to the control case. Next they considered whether

the substrate stiffness, which is analogous to the cell tension, impacted the probability of cell lysis. By comparing two hydrogels of stiffnesses 12 kPa and 50 kPa, the authors showed that CTL killing was significantly enhanced on the stiffer substrate. Basu et al. employed microvillar arrays to measure deflections of the pillars, and thus the force present at the cell-cell interaces.

Given that cell tension can cause cell membrane deformations, do CTLs spatiotemporally correlate the forces at the IS with perforin release? To test this theory, the authors used a pH-sensitive fluorescent probe that attaches to Lamp1, a protein inside lytic granules. Given an acidic environment, such as that of a lytic granule, the probe cannot fluoresce. However upon reaching and fusing to the target cell plasma membrane, the pH of the local environment is approximately neutral, which causes the probe to fluoresce. Remarkably, the increases in fluorescence of the degranulation probe spatiotemporally correlated with "hotspots", or regions of high tension at the cell-cell interface. This is highly suggestive that CTLs coordinate perforin release with applied local forces to potentiate target cell killing.

"Functional role of T-cell receptor nanoclusters in signal initiation and antigen discrimination"

A question within immunology that still lacks a clear understanding is how binding at the cell-cell interface is mechanistically related to signal transduction. Pageon et al. used single-molecule localization microscopy (SMLM) methods together with degree-of-co-localization (DoC) analysis to determine if the spatial pattern of TCR nanoclusters translated information about the antigen-presenting cell (100). Two-color SMLM was used to track the position of TCR-CD3 complexes by fusing a fluorescent protein to the CD3ζ chain. Phosphorylated TCR-CD3 complexes (pCD3) fluoresced red while unphosphorylated TCR-CD3 complexes were tracked using a green marker. Thus, this experimental technique gave positioning information about the phosphorylation state of all TCR-CD3 complexes in the system. The degree-of-co-localization then correlated the density gradients of the tracked proteins, i.e. CD3ζ and pCD3ζ.

The authors defined a "triggered CD3ζ cluster" as having $\geq$ 10 pCD3ζ molecules and a high degree of co-localization (DoC $\geq$ 0.40). DoC calculates the local density for every molecule at increasing distances, which thus provides density gradients for both the phosphorylated and unphosphorylated TCR-CD3 complexes. Intriguingly, the molecular density within triggered

clusters was approximately two-fold greater than non-triggered clusters for three different T-cell receptor systems. This gave rise to the question of whether pCD3ζ complexes aggregate into dense clusters or whether a high density of TCR-CD3 complexes leads to phosphorylation. To answer the "chicken or the egg" question, the researchers created a mutant where all tyrosine residues on the CD3ζ chain were replaced with leucine to abrogate phosphorylation (CD3ζ-6YL). Using the same system, they found that CD3ζ-6YL nanoclusters had a similar density to the wild type. This strongly suggests that the formation of TCR-CD3 nanoclusters precedes phosphorylation events.

Next, they examined the interplay between binding affinity, phosphorylation, and density of nanoclusters. Using a library of peptide ligands with varying degrees of binding affinity, Gauss et al. found the molecular density within the nanoclusters was dependent upon the TCR-pMHC binding affinity and pMHC concentration on the antigen-presenting cell surface (100). The relative density of the nanoclusters increased with both an increasing TCR-pMHC affinity and increasing pMHC concentration. The density of CD3ζ clusters was then highly correlated to the ensuing phosphorylation signal. Therefore, they proposed a mechanism for TCR signaling in which the TCR-pMHC binding event is converted into a spatial pattern reflective of the binding affinity and pMHC dose, which then gives rise to a chemical signature, i.e. phosphorylation.

"*In vitro* reconstitution of T-cell receptor-mediated segregation of the CD45 phosphatase"

To investigate the kinetic segregation model, the Vale group completed *in vitro* studies of giant unilamellar vesicle / supported lipid bilayer (GUV/SLB) systems (23). For the GUV, they co-expressed 2B4 TCR, which binds to class II IE^k MHC, and fluorescently tagged the β-chain of the receptor. Additionally, two CD45 phosphatase isoforms (CD45R$_0$ and CD45R$_{ABC}$, which have equilibrium lengths of 25 and 40 nm, respectively) were linked to the GUV to explore the effects of steric exclusion on pattern and cluster formation. His-tagged ligands were added to the SLB so that the interaction between the GUV and SLB mimicked the T-cell / antigen-presenting cell interface.

GUV/SLB contact led to spatial segregation of TCR-pMHC complexes and the two surface phosphatases in the intercellular junction at similar levels despite their differences in length. By loading several peptides on the SLB with varying TCR-pMHC affinities, Carbone et al. showed that TCR-pMHC binding affinity ≤ 15 μM resulted in approximately the same level of CD45R$_{ABC}$

exclusion (51%) (23). TCR-pMHC interactions with binding affinities weaker than ≤ 15 μM resulted in no $CD45R_{ABC}$ exclusion. This suggests that a threshold value of TCR-pMHC binding affinity will cause a step-like function in the exclusion of long surface phosphatases.

Proposed coupling of the actin cytoskeleton to T-cell activation

The actin cytoskeleton is likely an important candidate in modulating T-cell responses given its coupling to the TCR-CD3 complex and its function in organizing the immunological synapse. Several models have been proposed to explain the role of the actin cytoskeleton at the cell-cell interface including the conformational change model, kinetic segregation model, and frictional coupling model (32, 70, 147). The conformational change model focuses on the molecular level and posits that tension is transmitted to the TCR as the T cell crawls across the antigen-presenting cell via actin-dependent motion. The tension produced by the cell motion induces a conformational change within the CD3ζ chains that leave the cytoplasmic ITAMs exposed to kinases. Increasing structural evidence has supported the underlying notion of the coupling between a tensile force and a resulting TCR-CD3 conformational change (31, 37, 144).

The kinetic segregation model states that the spatial organization of proteins within the intercellular junction is influenced by steric exclusion (32). The TCR-pMHC complex, which is substantially shorter than many other surface proteins and complexes, holds the two membranes in close apposition. It is energetically unfavorable for longer surface molecules to reside in regions where the two membranes are in close apposition. Thus, larger surface molecules are driven towards intermembrane heights similar to their natural length. The actin cytoskeleton may support maintenance of these close-contact regions by regulating membrane tension through actin-based motors and promoting the formation of segregated protein domains, otherwise known as lipid rafts. It should be stated that the topic of lipid rafts remains controversial due to the complexity of experimentally observing these proposed nanometer-based domains (45, 80, 140).

The frictional coupling model proposes a transient binding mechanism between the actin cytoskeleton and clusters of TCRs and LFA-1 molecules that is responsible for spatial segregation seen in the immunological synapse. At long times, the immunological synapse forms a bull's eye pattern where different regions correspond to different protein complexes in the intercellular junction (138). The very center of the immuological synapse is termed the central

supramolecular activation cluster (cSMAC) and contains the majority of TCR-pMHC complexes (139). Essentially, receptor microclusters are actively translocated towards the cSMAC from the periphery in a manner that is dependent upon the number of linkages to actin. If a receptor microcluster has multiple linkages to the actin cytoskeleton, then there is a larger force that directs the microcluster towards the center of the immunological synapse. This model is able to explain the observation how larger LFA-1 microclusters are transported to the cSMAC despite their large steric hindrance, unlike the kinetic-segregation model.

1.2.3 T-cell microvilli

"Three-dimensional localization of T-cell receptors in relation to microvilli using a combination of super-resolution microscopies"

Microvilli are thin, actin-based filaments that extend outward from the main body of the T-cell. The spatial distributions of molecules on microvillar protrusions have been difficult to characterize due to the small size of the system and the high degree of spatial resolution that is required. Jung et al. recently characterized spatial distributions of several surface molecules on T-cell microvilli at nanometer resolution through the combination of two super-resolution techniques. Variable-angle total internal reflection fluorescence microscopy (VA-TIRFM) and stochastic localization nanoscopy (SLN) construct 3D images of the surface and report positions of the fluorescently labeled proteins, respectively. In particular, they observed that the spatial distributions for L-selectin and $\alpha\beta$TCRs co-localized with the microvillar tips. The molecular density of $\alpha\beta$TCRs at the microvillar tips was approximately four- to six-fold times higher than the TCR density on the rest of the cell body, implying that TCR complexes might be pre-clustered on microvilli. The high density of TCRs on microvillar tips could dramatically impact the avidity of TCR-pMHC interactions as the T cell scans across an antigen-presenting surface. Treating T cells with LatA, which blocks actin polymerization, resulted in the deterioration of the majority of microvilli. Thus, actin polymerization likely plays a role in the stabilization and movement of T-cell microvilli.

"Visualizing dynamic microvillar search and stabilization during ligand detection by T cells"

Cai et al. used lattice light-sheet (LLS) microscopy to image T cells and characterize their microvilli dynamics (22). After labeling the surface molecule CD45, the researchers measured the microvillar displacements across three individual cells to find an average microvillus velocity of 5.20 ± 0.40 μm/min. To estimate how efficiently microvilli scan target cell surfaces, Cai et al. considered a region above the isolated T cell that represented a putative surface. By tracking microvillar protrusions in relation to the two-dimensional plane, they generated plots for the instantaneous and cumulative coverage of the target cell surface. Microvilli randomly moved about the T-cell membrane and covered only $\sim$40% of the target cell surface at any given time. However, the cumulative target cell coverage rose to 98% within one minute. Thus, random microvilli movements are able to effectively scan a target cell surface within an immunologically relevant timescale.

Next, given an agonist-loaded antigen-presenting cell, Cai et al. measured the protrusion density of microvilli in response to the recognition of an antigenic ligand (22). Interestingly, the microvillar protrusion density did not change appreciably between regions of the T-cell surface that did or did not encounter the antigen-presenting cell. This indicates that the recognition of an antigenic ligand on the target cell surface does not impact the local densities of microvilli. To test how downstream signaling events coupled to microvillar searching, the researchers conducted drug inhibitory studies that blocked TCR-induced Ca^{2+} signaling, Src family kinases, and actin polymerization. Treatment of cells had no bearing on the microvillar scanning in regions of stabilized T-cell-APC contact. Therefore, once TCR microclusters have estabilished a strong contact with the antigen-presenting cell, they are no longer dependent on the actin cytoskeleton or downstream signaling.

"T-cell microvilli constitute immunological synaptosomes that carry messages to antigen-presenting cells"

Lymphocytes have been observed *in vivo* and *in vitro* to participate in a process known as trogocytosis, where a fragment of the lymphocyte plasma membrane containing surface proteins is extracted and then expressed on the antigen-presenting cell surface (44, 60). Kim et al. have

recently shown that T cells may use trogocytosis to sustain communication with cognate antigen-presenting cells over long distances (68). During the formation of the immunological synapse, the majority of T-cell microvilli are directed towards the center of the T-cell-antigen-presenting cell conjugate via cell polarization. However, as the T cell crawls across the target cell surface, a minority of T-cell microvilli remains anchored at the edge of the antigen-presenting cell. These form particles called T-cell microvilli-derived particles (TMPs), which contain a number of molecules relevant to T-cell activation including the TCR complex and co-stimulatory molecules.

Kim et al. explored differences in the number of observed TMPs given a stable, immunological synapse or motile, immunological kinapse. On average, kinapses produced more than two-fold as many TMPs as synapses, which may be due to the increased likelihood of breaking a microvillus contact from constant cell motion. By knocking out LFA-1, the researchers found the number of TMPs decreased considerably signifying that cellular adhesion is a central component in deriving TMPs. Interestingly, CD4+ TMPs deposited on dendritic cell (DC) surfaces were able to induce a robust Ca^{2+} flux and DC activation regardless of TCR engagement. Thus, TCR-pMHC signaling is not required to induce DC activation, and TMPs may act as "message-containing" vectors between T cells and DCs. Physically speaking, after a CD4+ T cell encounters a cognate DC and continues to propagate about the system in the search for antigens, a TMP can be left behind on the DC surface to sustain Ca^{2+} signaling and DC activation.

1.3 Instrumentation pertinent to T-cell mechanobiology

Recent advances in experimental instrumentation have helped capture previously unexplored features of the T-cell / antigen-presenting cell interface. Super-resolution visualization techniques allow better appreciation of the spatiotemporal dynamics of key players within T-cell activation. Single-molecule experiments have shown that forces, on the order of pico- to nanonewtons, play a pivotal role in cell adhesion, immunological synapse formation, and TCR microcluster aggregation. Below are a few important experimental techniques that have helped catapult the understanding of mechanobiology over the past five years.

1.3.1 Biomembrane Force Probe (BFP)

The biomembrane force probe (BFP) utilizes two micropipettes to measure the forces and binding kinetics of a receptor-ligand pair (54, 87). The first micropipette holds a red blood cell, with a known spring constant, that has a glass bead coated with pMHC molecules attached to its apex via streptavidin binding. Typically, the MHC on the probe bead is mutated so that no co-receptor binding will occur, thus ensuring direct measurements of TCR-pMHC binding. The micropipette with the red blood cell is held at a fixed location during the experiment.

The second micropipette holds a live T cell, which is brought into contact with the probe bead in repetitive cycles. The amount of time the T cell and the probe bead are within close apposition is called the contact time, and can be controlled. TCR-pMHC binding is observed by red blood cell elongation as the T cell approaches the probe bead, or detected bead displacement upon T-cell retraction. Because the spring constant is known, the deformation of the red blood cell can be translated into the force imparted on the receptor-ligand pair (76). Adhesion frequencies are then reported as a function of pMHC density, TCR density, and range of contact times. By analyzing the adhesion frequency curves, one can calculate the effective 2D affinity, dissociation rate, and effective 2D on-rate as a function of an applied force for a given TCR-pMHC.

1.3.2 Optical Trap / Tweezers (OT)

Optical traps use a highly focused Gaussian laser beam of infrared light to exert piconewton forces that can physically hold and manipulate small particles (31). Optical traps are able to measure and detect sub-nanometer displacements for sub-micron particles. In the limit of small displacements, the force applied to the particle is proportional to the particle displacement out of the trap, as given by Hooke's spring law (37). In the context of T-cell experiments, optical traps are used to apply force to a pMHC-coated polystyrene bead. Meanwhile, a T cell is immobilized on a glass coverslip operated by a piezoelectric stage. The T cell is brought into contact with the pMHC-loaded bead to induce binding. Afterwards, the stage is moved systematically to apply vectoral piconewton forces to the TCR-pMHC complex as the restoring force from the optical trap linearly increases with the piezoelectric stage displacement (38).

1.3.3 Lattice Light-Sheet Microscopy (LLS)

Lattice-light sheet microscopy (LLS) is a remarkably powerful super-resolution microscopy technique that has allowed experiments previously limited to minutes on other imaging platforms to be extended to the timescale of hours (27). LLS uses optical techniques to create a thin sheet of light that illuminates the entire sample with high spatial and temporal resolution. By using thin sheets of light, LLS reduces the overall exposure at the sample plane thus dramatically decreasing photoxicity and photobleaching effects. Recently, LLS was employed to study the dynamics of T-cell microvilli in naïve and antigen-experienced T cells, a field which has relatively limited understanding (22).

1.3.4 Supported Lipid Bilayers (SLBs) and Giant Unilamellar Vesicles (GUVs)

T cells mounted on planar, pMHC-loaded supported lipid bilayers (SLBs) have commonly been used for *in vitro* reconstitutions of interactions between a T cell and antigen-presenting cell. This system can be modulated to vary a wide variety of factors including protein density and variety. Recently, Jenkins et al. avoided the use of an SLB and instead used giant unilamellar vesicles (GUVs) to investigate cell-cell interactions (59). SLBs restrict diffusion of larger surface molecules and impose a higher rigidity on the lipid membrane, which is known to impact synapse formation and T-cell signaling. Thus, the GUVs represent a system closer to what T cells likely encounter in vivo. GUVs are functionalized by directly binding His-tagged immune cell surface proteins to nickel-nitrilotriacetic acid lipids on the vesicle surface (23). Results from recent studies using GUVs are consistent with the kinetic segregation model, in which larger surface molecules are excluded from regions where the two membranes are in close apposition.

1.3.5 Molecular tension-based fluorescence microscopy

DNA-hairpin nanoparticle tension sensors were recently engineered to detect if a threshold force is exceeded between an individual receptor-ligand pair (77). Each DNA hairpin is labeled with a fluorophore-quencher pair and is bound to a gold nanoparticle, which is immobilized on

a glass coverslip. Streptavidin interconnects the end of the DNA hairpin with the desired pMHC molecule (148). The T cell is then placed on top of the coverslip and allowed to interact with the tension sensors (78).

Initially, all tension sensors are in the "closed" loop phase, where the fluorphore is in close proximity to the quencher, preventing any detectable fluorescence. However, if the force resulting from a bound TCR-pMHC pair is sufficiently strong, the DNA-hairpin loop will break and drastically increase the distance between the fluorphore-quencher pair. Switching to this "open" state increases the fluorescence by a factor ~ 100. Thus, the DNA-hairpin acts as a digital sensor to indicate that a force threshold has been met between a receptor-ligand pair. Importantly, the hairpin sensors are force tunable, and are dependent upon the structure and length of the DNA stem loop. While determining an exact force on a receptor-ligand pair is not possible using this system, the combination of multiple tension sensors can be used to probe a range of forces.

1.3.6 Single-Molecule Localization Microscopy (SMLM)

Single-molecule localization microscopy (SMLM) is a group of experimental techniques that attain resolution below the diffraction limit by exploiting photoswitchable fluorescent probes. These fluorescent probes are commonly induced via irradiation with light or by the chemical environment. The key to SMLM is that there must be a small subset within the overall population of the activated, or fluorescent, proteins at any given time. By inducing activation events at sufficiently distinct times, different subsets of fluorophores are imaged without substantial overlap to previous images. Upon repeated activation, the positions of the protein of interest can be evaluated with high precision.

Reconstructed super-resolution images are obtained by the superimposition of fluorophores at all collected time points. A common practice is to use a statistical fit of the ideal Gaussian to approximate a fluorescence signature. The two main methodologies of SMLM are photoactivated localization microscopy (PALM) and stochastic optical reconstruction microscopy (STORM) (3, 12, 115). SMLM imaging has been critical to elucidating the spatial distribution of T-cell receptors in resting, antigen-experienced cells and how T-cell receptors aggregate together into nanoclusters upon TCR triggering (100, 114).

1.3.7 Atomic Force Microscopy (AFM)

Atomic force microscopy (AFM) uses deflections from the sharp tip of a cantilever to measure forces and image the cell with high resolution. The T cell is mounted on a piezoelectric scanner that controls its three-dimensional positioning. The tip of the AFM cantilever is commonly cross-linked with streptavidin to either pMHC or anti-CD3, and comes into direct contact with the T cell. Given the known stiffness of the cantilever, deflections of the lever directly relay the binding forces between the T-cell receptor and ligand / antibody. A laser beam deflection system images the cell simultaneously by tracking differences between photo-detector signals given a cantilever deflection.

The piezoelectric stage allows AFM to measure how T cells respond to a variety of intercellular contacts. For instance, the pMHC-loaded cantilever tip can stay in continuous contact with the T cell or oscillate, causing multiple binding and dissociation events. Researchers have used these techniques to compare how cyclical and continuous contact influences the calcium flux of the T cell (52).

1.3.8 Traction Force Microscopy (TFM)

Traction force microscopy (TFM) determines the forces at the interface between a cell and its substrate by measuring the surrounding displacement field. Fluorescent beads are immobilized within the hydrogel substrate and serve as markers for the displacement field. Given the mechanical properties of the hydrogel and the time-dependent displacement field, one can track the traction forces at the interface between the cell and the substrate. TFM often uses polydimethylsiloxane (PDMS) hydrogels, which can be engineered to have an elasticity range on the order of hundreds of kPa. TFM is useful for exploring how cell substrate stiffness impacts T-cell activation. Interestingly, TFM has shown that substrate rigidity impacts the differentiation of CD4+ T cells (98).

1.4 Model Formulation

The continuous feedback between the vast number of experimental and computational studies promotes an increased level of understanding within the scientific community for underlying biophysical mechanisms. Here, we detail the methodology used for the biophysically motivated computational models presented in the thesis.

1.4.1 Gillespie Algorithm

Deterministic modeling is typically reserved for large systems where the chemical species can be approximated as continuous variables. In the context of many biological problems, particularly at or smaller than the cellular level, small numbers of molecules can drive large fluctuations resulting in varied responses for the same conditions. To account for the inherent randomness within the system, stochastic simulations are commonly implemented to span the ensemble of responses and attain a better grasp of the underlying dynamics.

Monte Carlo simulations use repeated random sampling to generate trajectories that simulate the time evolution of a process. For a biochemical system, the transition rates of the Monte Carlo method relate the probability of undergoing a reaction or "move". Unlike a deterministic system, the probability of these moves do not explicitly determine the time evolution of the system. Instead, repeated random sampling generates an ensemble of trajectories given an initial condition. The average, variability, and distribution of the ensemble relays information about the likelihood of observing a given state / reaction.

One particular stochastic simulation method widely used to study biochemical networks is called the Gillespie algorithm. The algorithm takes into account discrete chemical species and the stochastic nature of a system by producing trajectories that describe the time evolution of all chemical species in the system. The algorithm depends on all possible reactions that can take place within the system. For instance, in the interaction of a T cell with an antigen-presenting cell (further detail: Ch. 3, 4), a T-cell receptor can participate in a binding reaction with a proximal pMHC molecule, diffuse about the system when unbound, or if already bound to a pMHC molecule, dissociate from it.

At any given time, the system has a particular configuration and a propensity asociated with each reaction. Each propensity, $a_j(\mathbf{x})$, is the probability per unit time that a reaction j occurs. At each time step, a single reaction occurs, and the chemical species populations are updated by the state-change vector

$$\nu_j = (\nu_{1j}, \ldots, \nu_{Nj}), \tag{1.1}$$

where ν_{ij} is the change in the chemical species and N is the total number of chemical species. When an event occurs, the state of the system $\mathbf{x}$ is updated to state $\mathbf{x} + \nu_j$. The total propensity, a_0, is the sum of all $a_j(\mathbf{x})$. The following two equations determine the time interval between events τ and the next reaction j:

$$\tau = \frac{1}{a_0(\mathbf{x})} \ln\left(\frac{1}{r_1}\right) \tag{1.2}$$

$$j = \min_j \{ \sum_{j'=1}^{j} a'_j(\mathbf{x}) > r_2 a_0(\mathbf{x}) \}. \tag{1.3}$$

Here, r_1 and r_2 are uniformly distributed random numbers in the interval [0,1]. Hence, until the final simulation time point is reached, the Gillespie algorithm can be written as:

1. Distribute initial chemical species
2. Calculate all reaction propensities $a_j(\mathbf{x})$ and the total propensity a_0
3. Draw two random numbers to determine the time interval τ and the next reaction j
4. Update the chemical species populations based on the chosen reaction
5. Record $(\mathbf{x}, t)$ and return to Step 2

1.4.2 Membrane Energetics

To consider the interactions of the intercellular junction between an apposed T cell and antigen-presenting cell, we modeled the two membranes as continuum surfaces characterized by a bending rigidity, κ. We then denote the position- and time-dependent distance of the between the two membranes as $z(x,y,t)$. The energy of a membrane patch within our system can be expressed as a

modified Helfrich Hamiltonian:

$$E[z, C_{\text{CD45}}, C_{\text{bond}}] = \iint dx\, dy \left(\left(\frac{\kappa}{2} \left(\nabla^2 z - 2c_0 \right)^2 + \overline{\kappa} K_{\text{G}} \right) + k_{\text{CD45}} C_{\text{CD45}} \left(z_{\text{CD45}} - z \right)^2 + \right.$$
$$\left. \ldots + k_{\text{bond}} C_{\text{bond}} \left(z_{\text{bond}} - z \right)^2 \right).$$

where c_0 is the spontaneous curvature, $\overline{\kappa}$ is the Gaussian curvature, k_i are the compressional stiffness constants, and C_i are the concentrations of the chemical species.

The spontaneous curvature is set to zero in the case of a symmetric lipid bilayer, which is the assumed condition in our simulations. A nonzero spontaneous curvature would indicate that the membrane would prefer to be spontaneously curved into one direction. The Gaussian curvature is equivalent to the product of the two principal curvatures of the biological membrane. The principal curvatures are the inversely proportional to the principal radii of curvature, which approach infinity given a planar geometry. In addition, by the Gauss-Bonnet theorem, the total Gaussian bending energy integrated over a closed surface is constant (71). Hence, the Gaussian curvature term in our simulations can be eliminated from the governing energy equation leaving the expression:

$$E[z, C_{\text{CD45}}, C_{\text{bond}}] = \iint dx\, dy \left(\frac{\kappa}{2} \left(\nabla^2 z \right)^2 + k_{\text{CD45}} C_{\text{CD45}} \left(z_{\text{CD45}} - z \right)^2 + k_{\text{bond}} C_{\text{bond}} \left(z_{\text{bond}} - z \right)^2 \right). \tag{1.4}$$

1.4.3 Metropolis Monte Carlo Scheme

The Metropolis Monte Carlo scheme is a Markov chain Monte Carlo method that computes values of a function, $f(\mathbf{x})$, using a probability distribution, $P(\mathbf{x})$, and independent proposal distributions. Given an initial distribution for the function $f(\mathbf{x})$, candidate distributions are generated from random sampling of values. Candidate distributions are accepted in proportion to the density of $P(\mathbf{x})$. After many repeated iterations, the values of $f(\mathbf{x})$ more closely approximate the desired distribution.

For our system of interest, the Metropolis Monte Carlo scheme generates a trial configuration by perturbing the intermembrane distance profile at a given location. Given the resulting energy difference in the membrane configurations, ΔE, the trial configuration is either accepted or rejected

by the Metropolis criterion: Energetically favorable trial configurations are accepted ($\Delta E \leq 0$); otherwise, the trial configuration is accepted with probability $\exp(-\beta\Delta E)$, where $\beta = 1/k_{\mathrm{B}}T$. After performing sufficient perturbations (Monte Carlo sweeps), the system reaches thermal equilibrium and the energy of the system fluctuates about a plateau for the given chemical species configuration. After equilibration, the intermembrane distance profile is updated and the simulation progresses to the next time step. It is important to note this algorithm assumes that the membrane configuration relaxes at a faster timescale than the reorganization of surface molecules within the intercellular junction.

1.4.4 Time-dependent Ginzburg-Landau Model

The time-dependent Ginzburg-Landau (TDGL) model is a phenomenological, non-equilibrium dynamical approach that relates an order parameter to the Helmholtz free energy of the system. For the T-cell / antigen-presenting cell model, our order parameter is the intermembrane distance profile, $z(\vec{x},t)$. In contrast to the Metropolis Monte Carlo scheme, the time-dependent Ginzburg Landau model does not presume that the intermembrane distance profile is able to reach mechanical equilibrium before the next diffusive or reaction within the intercellular junction.

The time-dependent Ginzburg Landau model takes the functional derivative of the energy equation (Eqn. 1.4) with respect to the intermembrane distance profile.

$$\frac{\partial z}{\partial t} = -M\frac{\delta E}{\delta z} + \zeta, \tag{1.5}$$

where M is the phenemonological constant that sets the timescale for membrane relaxation and ζ is thermal noise. Expanding the functional derivative,

$$\frac{\delta E}{\delta z} = \frac{\partial E}{\partial z} - \frac{\partial}{\partial x}\frac{\partial E}{\left(\frac{\partial z}{\partial x}\right)} - \frac{\partial}{\partial y}\frac{\partial E}{\left(\frac{\partial z}{\partial y}\right)} + \frac{\partial^2}{\partial x^2}\frac{\partial E}{\left(\frac{\partial^2 z}{\partial x^2}\right)} + \frac{\partial^2}{\partial y^2}\frac{\partial E}{\left(\frac{\partial^2 z}{\partial y^2}\right)} + \frac{\partial^2}{\partial x \partial y}\frac{\partial E}{\left(\frac{\partial^2 z}{\partial x \partial y}\right)}.$$

After differentiating the energy equation for all terms, we find

$$\frac{\partial z}{\partial t} = -M\left[\kappa\left(\frac{\partial^4 z}{\partial x^4} + \frac{\partial^4 z}{\partial y^4} + 2\frac{\partial^4 z}{\partial x^4 \partial y^4}\right) - k_{\mathrm{bond}}C_{\mathrm{bond}}(z_{\mathrm{bond}} - z) - k_{\mathrm{CD45}}C_{\mathrm{CD45}}(z_{\mathrm{CD45}} - z)\right] + \zeta$$

$$\therefore \frac{\partial z}{\partial t} = -M\left[\kappa\nabla^4 z - k_{\text{bond}}C_{\text{bond}}(z_{\text{bond}} - z) - k_{\text{CD45}}C_{\text{CD45}}(z_{\text{CD45}} - z)\right] + \zeta \tag{1.6}$$

Implementing a forward time-marching method with a central finite difference scheme, we can solve for the updated intermembrane distance profile. Each membrane height on the domain is updated once according to Eqn. 1.6 before progressing to the next time step.

1.4.5 Advection-diffusion Equations

If the energetics of the local intermembrane shape influence the concentration of a chemical species, an advection term must be added to describe its spatiotemporal dynamics. The advection term imposes an energetic penalty for molecules residing within the intercellular junction that are within a region different than their natural length. For our systems of interest, this applies to the CD45 phosphatase, slip bonds, and catch bonds. The transmembrane domain of the CD45 phosphatase spans $\approx 40-50$ nm, which is much larger than the natural length of TCR-pMHC complex bonds, $z_{\text{bond}} \approx 13-15$ nm. Generally, the spatiotemporal dynamics of a chemical species can be written as

$$\frac{\partial C_i}{\partial t} = D_i\nabla^2 C_i + \frac{D_i}{k_{\text{B}}T}\nabla\cdot\left[C_i\nabla\frac{1}{2}k_i(z - z_i^{\text{eq}})^2\right] + R_i \tag{1.7}$$

where D_i is the diffusion coefficient, $k_{\text{B}}T$ is the thermal energy, z_i^{eq} is the natural length of the chemical species, and R_i includes all reaction terms for the chemical species.

We first used a continuum model to describe the concentration of long surface molecules (i.e. CD45 phosphatases) for systems with static, intermembrane bonds (Ch. 2). A natural extension of the system is to characterize how the presence of laterally diffusive bonds, T-cell receptors, pMHC molecules and TCR-pMHC complexes impact the results at the T-cell-antigen-presenting cell interface. Considering a 2D square lattice defined in the plane, with lattice size Δx, the diffusion coefficient of proteins, D, on the surface is related to a stochastic hopping rate by $\gamma = D/(\Delta x)^2$ in the absence of an energetic gradient. The Grima-Newton master discretization method accounts for diffusion of discrete chemical species that are dependent upon the local intermembrane distance

profile. The modified rate of hopping from position i to adjacent lattice site j can be written as

$$\gamma_{i\to j} = D/(\Delta x)^2 \exp[-\beta(E_j - E_i)/2]. \tag{1.8}$$

1.5 Thesis Outline

In this thesis, we use computational methods to primarily characterize the interactions of T cells with antigen-presenting cells at the conjugate interface. A Gillespie algorithm is then applied to model the interactions for the receptor clustering of Ephrin-A2 molecules.

1. Catch bonds at T-cell interfaces: Impact of spatial reorganization and membrane fluctuations (Ch. 2).

2. Dynamics of T-cell receptor cluster formation (Ch. 3)

3. Mechanical feedback enables catch bonds to selectively stabilize scanning microvilli at T-cell surfaces (Ch. 4)

4. Dyamics of Eph-A2 receptor clustering (Ch. 5)

For each project, we employ appropriate kinetic parameters to simulate the spatiotemporal dynamics of a living system. Systematic variation of select parameters and conditions reveal nontrivial coupling with emergent system behavior.

1.5.1 Catch bonds at T-cell interfaces: Impact of spatial reorganization and membrane fluctuations (Ch. 2)

Catch bonds are characterized by average lifetimes that initially increase with increasing tensile force. Recently, they have been implicated in T-cell activation, where small numbers of antigenic receptor-ligand bonds at a cell-cell interface can stimulate a T cell. Here, we use computational methods to investigate small numbers of bonds at the interface between two membranes. We characterize the time-dependent forces on the bonds in response to changes in the membrane shape and the organization of other surface molecules. We then determine the distributions of bond

lifetimes using recent force-dependent lifetime data for T-cell receptors bound to various ligands. Strong agonists, which exhibit catch bond behavior, are markedly more likely to remain intact than an antagonist whose average lifetime decreases with increasing force. Thermal fluctuations of the membrane shape enhance the decay of the average force on a bond, but also lead to fluctuations of the force. These fluctuations promote bond rupture, but the effect is buffered by catch bonds. When more than one bond is present, the bonds experience reduced average forces that depend on their relative positions, leading to changes in bond lifetimes. Our results highlight the importance of force-dependent binding kinetics when bonds experience time-dependent and fluctuating forces, as well as potential consequences of collective bond behavior relevant to T-cell activation.

1.5.2 Dynamics of T-cell receptor cluster formation (Ch. 3)

T-cell receptor microclusters are thought to play a role in both the detection of foreign antigens, and the chemo-mechanical translation of physical properties at the cell-cell interface to downstream signaling processes. Here, we employ a hybrid computational model to investigate the role of catch bond behavior at the cell-cell interface with regards to TCR cluster formation. By varying both the fraction of agonist pMHC and density of pMHC molecules on the antigen-presenting cell, we find that stimulatory pMHC molecules play a central role in the formation of TCR clusters. We observe TCR cluster formation and aggregation within a 5 second period given the T-cell membrane and antigen-presenting cell are initially in close proximity. Our results demonstrate that the formation of TCR clusters drives longer surface molecules from regions of close apposition, supporting the proposed kinetic segregation model.

1.5.3 Mechanical feedback enables catch bonds to selectively stabilize scanning microvilli at T-cell surfaces (Ch. 4)

T cells use microvilli to search the surfaces of antigen-presenting cells for antigenic ligands. The active motion of scanning microvilli provides a force-generating mechanism that is intriguing in light of single-molecule experiments showing that applied forces on stimulatory receptor-ligand bonds increase their lifetimes (catch-bond behavior). In this work, we introduce a theoretical framework to explore the motion of a microvillus tip above an antigen-presenting surface when

receptors on the tip stochastically bind to ligands on the surface and dissociate from them in a force-dependent manner. Forces on receptor-ligand bonds impact the motion of the microvillus, leading to feedback between binding and microvillar motion. We use computer simulations to show that the average microvillus velocity varies in a ligand-dependent manner, that catch bonds generate responses in which some microvilli almost completely stop while others move with a broad distribution of velocities, and that the frequency of stopping depends on the concentration of stimulatory ligands. Typically, a small number of catch bonds initially immobilize the microvillus, after which additional bonds accumulate and increase the cumulative receptor-engagement time. Our results demonstrate that catch bonds can selectively slow and stabilize scanning microvilli, suggesting a physical mechanism that may contribute to antigen discrimination by T cells.

1.5.4 Eph-A2 receptor clustering (Ch. 5)

Eph receptors are the largest subfamily of receptor tyrosine kinases. Overexpression and high activity of EphA2 receptors without its ligand, ephrin-A1, has been found to be a marker of numerous cancers. Interestingly, the full activation of EphA2 receptors and corresponding Eph-ephrin signaling has been observed to mitigate the invasive potential of tumor cells. Thus, the promotion of EphA2 receptor activation could likely impede the progress of an existing cancer. The Barrera laboratory group has developed a novel peptide that relies on the inherent acidity of the tumor microenvironment to locate and then bind to the overexpressed EphA2 receptor. EphA2 receptors are not fully activated until they are present in an oligomer form, which first requires the dimerization of EphA2 receptors. Here, we supplement experiments of our collaborator by providing a computational model to gain mechanistic insight of the underlying dynamics of EphA2 receptor cluster formation. Using a one-dimensional Gillespie algorithm, we account for and track the time evolution of diffusive motion and binding reactions of all chemical species in the EphA2 receptor system. Our results showcase that the titration of a targeted peptide into the system promotes the formation of EphA2 receptor clustering and sequestration of monomeric EphA2 receptors.

Chapter 2

Catch bonds at T-cell interfaces: Impact of spatial reorganization and membrane fluctuations

Summary: A version of this chapter was originally published by Robert H. Pullen, III and Steven M. Abel (107): Pullen III, Robert H., and Steven M. Abel. *Catch bonds at T cell interfaces: Impact of surface reorganization and membrane fluctuations*. Biophysical Journal. 113.1 (2017): 120-131.

2.1 Introduction

Membrane-associated proteins experience a variety of forces at the interface between interacting cells. The forces can arise from sources including membrane undulations, cell motion, and active cytoskeletal processes (48). In the context of cell adhesion, there has been significant interest in protein-protein bonds known as catch bonds, which have average lifetimes that initially increase with an increasing tensile force (134). This is in contrast to the more prevalent slip bond, which has an average lifetime that decreases with increasing force (11). Well-studied examples of catch bonds include adhesion proteins that mediate shear-enhanced adhesion, such as selectins in leukocytes (84) and FimH in *E. coli* (96, 120, 133). Catch bonds are also involved in maintaining the integrity of multicellular tissues in cadherin-based adhesions (19, 83), and emerging evidence

suggests that T cells use catch bonds in their search for antigens on the surfaces of other cells (31, 76).

T cells orchestrate the adaptive immune response and use the T-cell receptor (TCR) complex to engage membrane-presented ligands on the surfaces of other cells as they scan for antigen. An outstanding question in immunology is how the T cell reliably distinguishes between self and foreign ligands while being sensitive to even a single antigenic ligand (53, 100, 130). A number of recent studies have shown that TCRs can exhibit catch-bond behavior when engaged with stimulatory ligands, which raises the intriguing question of whether the catch-bond behavior contributes to the T cell's specific and sensitive response (31, 34, 76).

The TCR binds to peptide fragments presented by major histocompatability complex proteins (pMHC) on the surfaces of other cells. The binding kinetics between the TCR and pMHC are thought to largely control T-cell activation (75, 149), yet kinetics are difficult to measure *in situ* (54, 56, 112). Recent work has begun to elucidate the importance of forces on the TCR at the T-cell interface (62). For example, insight has been gained from experimental methods including optical tweezers (31, 69), biomembrane force probes (51, 76), atomic force microscopy (52), nanoparticle tension sensors (77), and traction force microscopy (8, 55). Some of these studies have directly measured TCR-pMHC binding times as a function of force, showing binding kinetics consistent with catch-bond behavior (31, 51, 76).

In this paper, we focus on TCR lifetime data from Liu et al. (76), who measured the force-dependent average lifetime of OT1 TCRs bound to ligands of varying stimulatory strength. As shown in Fig. B.1, they observed that stimulatory ligands (OVA and A2) exhibited catch-bond behavior while other ligands (E1 is shown here) exhibited slip-bond behavior. The off rate of a slip bond is commonly described by the Bell model (11),

$$k_{\text{off}}^{\text{slip}}(f) = k_0\, e^{f/f_0}, \tag{2.1}$$

where k_0 is the off rate at zero applied force, f is the applied force on the receptor-ligand complex, and f_0 is the reference force. There are a number of simple mathematical models for catch-bond

kinetics, with a common description being the two-pathway model (104),

$$k_{\text{off}}^{\text{catch}}(f) = k_c\, e^{-f/f_c} + k_s\, e^{f/f_s}\,, \tag{2.2}$$

where c denotes catch-phase parameters and s denotes slip-phase parameters. The average lifetime of a bond is given by k_{off}^{-1}. Fig. B.1 also includes fits of the data that were obtained using a nonlinear least squares fitting procedure (parameters are tabulated in the Appendix).

It is interesting to consider the implications of catch-bond behavior in the context of antigen discrimination by T cells, as many factors influence the formation and dissociation of TCR-pMHC complexes at the T-cell interface. For example, differences between the lengths of the TCR-pMHC complex and other key surface proteins have led to the kinetic-segregation model for TCR triggering, in which large proteins are excluded from regions near TCR-pMHC complexes (32). This is due to the relatively short distance between membranes imposed by the TCR-pMHC complex ($\approx$ 13 nm) that restricts access of longer molecules ($\sim$ 50 nm) (2). In particular, exclusion of the transmembrane phosphatase CD45 is proposed to locally alter the balance of kinase and phosphatase activity near the intracellular domain of the TCR complex (32). It is energetically unfavorable to bend membranes over short length scales, and the coupling of protein size exclusion to membrane bending mechanics can lead to deformations of the membrane, a large-scale reorganization of the membrane, and a time-dependent force on a single TCR-pMHC bond (2, 25, 108).

It is unclear how small numbers of catch bonds at a cell-cell interface are influenced by membrane shape changes, reorganization of surface molecules, and thermal fluctuations. In this work, we consider a computational framework that represents small numbers of bonds at the interface of a T cell and an antigen-presenting cell. We begin by introducing the framework and computational methods. We then explore the dynamic response to the formation of one or more fixed bonds, characterizing the resulting membrane reorganization, the time-dependent forces experienced by the bonds, and the resulting distribution of bond lifetimes. By using the data discussed above, we assess the influence of catch- versus slip-bond binding kinetics in the context of TCR binding.

2.2 Methods

2.2.1 Membrane dynamics

We consider a framework in which two apposed membranes are connected by one or more static intermembrane bonds. The membranes are modeled as continuum surfaces characterized by a bending rigidity that penalizes membrane deformations. The intermembrane bonds constrain the membranes to reside at a fixed distance apart at the location of the bonds. The membrane shape and distribution of surface molecules evolve in time in response to the presence of bonds.

We consider a square domain and denote the position- and time-dependent distance between the membranes by $z(x,y,t)$. The concentration of surface molecules is denoted by $C_{\mathrm{SM}}(x,y,t)$ and the total energy of the system is

$$E[z,C_{\mathrm{SM}}] = \iint dx\,dy \left(\frac{\kappa}{2}\left(\nabla^2 z\right)^2 + C_{\mathrm{SM}} E_p \right), \tag{2.3}$$

where κ is the membrane bending rigidity and E_p is the energy associated with compression of the surface molecules (2, 35, 108). The total energy is comprised of two parts: The first is the bending term of the Helfrich Hamiltonian in the limit of small deformations (95), which penalizes bending of the membrane. The second part penalizes the presence of surface molecules if the local membrane separation differs from their natural length, z_p. The compressional energy takes the form $E_p(x,y,t) = k_p(z_p - z)^2/2$. Position and time arguments are omitted for clarity.

We adopt a hybrid computational scheme to characterize the dynamics of the intermembrane distance profile (z) and the concentration profile of surface molecules (C_{SM}): C_{SM} is governed by an advection-diffusion equation and the membrane adapts by mechanically equilibrating in response to the changing concentration profile. Given a membrane shape, the concentration of surface molecules changes according to

$$\frac{\partial C_{\mathrm{SM}}}{\partial t} = D\nabla^2 C_{\mathrm{SM}} + \frac{D}{k_{\mathrm{B}}T}\nabla\cdot\left(C_{\mathrm{SM}}\nabla E_p\right), \tag{2.4}$$

where D is the diffusion coefficient and $k_{\mathrm{B}}T$ is the thermal energy. Thus, the concentration of surface molecules evolves in time in response to the shape of the membrane, which affects

E_p. To solve the advection-diffusion equation, we employ an explicit forward-time difference method and spatially discretize the system, using central finite difference approximations with periodic boundary conditions. After each time step, we use Metropolis Monte Carlo computer simulations to generate a membrane configuration that is sampled from thermal equilibrium. Allard et al. adopted a similar framework in which the equilibrated membrane separation profile was solved using a generalized Euler-Lagrange equation to minimize the energy (2). Using Monte Carlo methods allows one to account for thermal fluctuations in the membrane shape and provides flexibility in solving systems with various distributions of intermembrane bonds.

We initialize the system by assuming that one or more intermembrane bonds have formed and that surface molecules are homogeneously distributed with concentration $C_{\mathrm{SM},0}$. Locations with bonds are pinned to their natural length (13 nm). We first equilibrate the intermembrane height profile given the presence of bonds and the uniform distribution of surface molecules. The concentration profile of surface molecules is propagated forward in time using the advection-diffusion equation, after which the membrane height profile is equilibrated. This process is then repeated to determine the time evolution of the system.

Parameters used in the model are summarized in Table B1. The system size is 510 nm $\times$ 510 nm, which is sufficiently large such that finite-size effects do not influence the results. The spatial discretization size is $\Delta x = 10$ nm, which is commensurate with the footprint of a single TCR complex within the T cell membrane (14). The time step is chosen to ensure stability of the numerical solutions of the advection-diffusion equation (Fig. B.11) (47). To assess the effects of bending rigidity, we consider two values ($\kappa = 12.15$ and 40 $k_{\mathrm{B}}T$) that span biologically relevant values (2, 16, 72, 86). The compressional stiffness, $k_p = 0.1$ pN/nm, is consistent with previous estimates (2) and is sufficiently large to drive segregation of surface molecules away from TCR-pMHC bonds.

2.2.2 Monte Carlo simulations

Monte Carlo simulations are used to update the spatially discretized distance profile $z(x,y,t)$. Trial configurations are generated by randomly choosing a lattice site and perturbing the distance by a uniformly sampled random variable between -0.05 and 0.05 nm. After calculating the

resulting energy change (ΔE) using Eqn. 2.3, the trial configuration is either accepted or rejected according to the Metropolis criterion: Energetically favorable ($\Delta E < 0$) trial configurations are accepted; otherwise, the trial configuration is accepted with probability $\exp(-\beta\Delta E)$, where $\beta = 1/k_{\mathrm{B}}T$. Each Monte Carlo step consists of 51^2 attempted updates, so that each site has one attempted update on average per step. After bonds are placed between the two membranes, we run the initial equilibration for 10^5 Monte Carlo steps. After each update to C_{SM}, the membrane height profile is equilibrated for 5×10^3 Monte Carlo steps. The number of steps required for equilibration is significantly smaller since the changes are more subtle after the initial binding event. For each set of conditions considered below, we run 10 independent trajectories.

In the results, we are interested in the effects of thermal fluctuations. As such, we also conduct simulations in which we let $\beta \to \infty$ in the Metropolis criterion. For these simulations, any trial configuration with $\Delta E \leq 0$ is accepted and any energetically unfavorable trial configuration is rejected. Thus, the energy decreases monotonically. In results below, we refer to simulations "without thermal fluctuations" when $\beta \to \infty$.

2.2.3 Bond tension and survival probability

The force experienced by a bond at time t is given by $f(t) = \partial E/\partial z|_{\mathbf{x}=\mathbf{x}_0}$, where $\mathbf{x}_0$ denotes the position of the bond (2). We compute the derivative numerically by perturbing the intermembrane distance upward and downward from its constrained value of z_0 (74). Given the time-dependent tension on the bond, we calculate the distribution of rupture times. For every time step Δt, the probability that a bond ruptures is

$$p_{\mathrm{rup}}(f) = 1 - e^{-k_{\mathrm{off}}(f)\Delta t}\ , \tag{2.5}$$

where $k_{\mathrm{off}}(f)$ is the force-dependent dissociation rate. We report the calculated distributions in terms of the survival probability, $S(t)$, which gives the probability that a bond has not ruptured by time t:

$$S(t) = \prod_{i=0}^{N_t} \exp\Big(-k_{\mathrm{off}}\big(f(t_i)\big)\Delta t\Big)\ . \tag{2.6}$$

Here $N_t = (t/\Delta t) - 1$ denotes the number of times intervals and $f(t_i)$ is the force at time t_i.

2.3 Results

We begin by examining a system with a single bond. We characterize the membrane response to bond formation, the time-dependent bond tension and associated fluctuations, and the probability that the bond remains intact as a function of time. We then explore the impact of an additional bond as the distance between bonds is varied.

2.3.1 Bond formation drives membrane reorganization

The formation of an intermembrane bond causes a response in the membrane shape (z) and in the distribution of surface molecules (C_{SM}). Fig. B.2A shows snapshots of z and C_{SM} from a sample trajectory with a single bond at the center of the domain. Because the TCR-pMHC bond is shorter than the surrounding surface molecules, there is an energetic penalty for surface molecules near the bond. This leads to a rapid expulsion of surface molecules from the region near the bond, leading to a ring of high concentration that can be observed at $t = 0.05$ s. The size of the region in close apposition increases slightly between the two time points, and fluctuations in the distance profile are reflected in the non-uniform shape of this region and in the heterogeneity of z far from the bond.

To more completely characterize the time-dependence of z and C_{SM}, we consider a one-dimensional strip containing the bond and plot the time-dependence of z and C_{SM} along the strip as a kymograph (Fig. B.2B). For C_{SM}, there is a broadening of the region depleted in surface molecules (i.e., the "depletion zone") and an eventual dissipation of the high-concentration ring due to the diffusion of molecules from the ring into the region far from the bond. For z, one can see a slight broadening of the deformed region and the presence of fluctuations, although the shape of the deformation remains largely stable. Results for $\kappa = 40\ k_{\mathrm{B}}T$ are qualitatively similar with a broader depletion zone, and analogous results from simulations in which thermal fluctuations are neglected are included in Fig. B.12. In this case, the membrane shape evolves to minimize energy at each time point. The results are qualitatively similar to Fig. B.2, but the lack of thermal fluctuations in the membrane shape leads to smoother features.

The influence of bending rigidity and thermal fluctuations on membrane relaxation are more clearly observed in Fig. B.3. Here, we plot the characteristic diameter of the depletion zone, $d(t) = (4A_{\text{dep}}(t)/\pi)^{1/2}$, where A_{dep} is the area of the membrane with $C_{\text{SM}} \leq 0.01\, C_{\text{SM},0}$. For the two bending rigidities considered, the size of the depletion zone increases more rapidly for the case with thermal fluctuations, although the difference is more pronounced at the larger value of κ. Fig. B.3 also demonstrates the effect of membrane bending rigidity on the size of the domain surrounding the bond. Since larger values of κ impose higher energetic penalties for bending, the intermembrane shape with $\kappa = 40\ k_{\text{B}}T$ adopts a locally flatter shape near the bond, and a larger footprint overall. This in turn leads to a larger region in which it is energetically unfavorable for surface molecules to reside. Thus, increasing the membrane stiffness, κ, promotes the formation of a larger depletion zone.

2.3.2 Bonds experience a time-dependent tension with fluctuations driven by membrane shape fluctuations

When a bond forms, changes in membrane shape and surface organization alter the energy profile near the bond, which leads to a time-dependent force on the bond. As the system evolves toward more energetically favorable configurations, the average tension on the bond decreases. In Fig. B.4, we compare the average tension experienced by a bond both with and without thermal fluctuations. Increasing the membrane bending rigidity (κ) leads to a larger average tension on the bond. The presence of thermal fluctuations leads to a smaller initial average force and a faster decay of the tension, which is consistent with the faster relaxation of the membrane discussed above. The difference is more pronounced at larger κ.

Comparing cases with and without thermal fluctuations, it is evident that membrane fluctuations lead to significant fluctuations in the force on the bond. To characterize the force fluctuations, we determine the distribution of forces for $t > 0.5$ s, as the depletion zone is almost completely formed during this time. For $\kappa = 12.15\ k_{\text{B}}T$, the bond experiences a force of 7.07 ± 6.32 pN (average $\pm$ standard deviation); for $\kappa = 40\ k_{\text{B}}T$, the bond experiences 13.5 ± 11.6 pN. The distribution of mean-centered forces is shown in Fig. B.5, which demonstrates the broader range of fluctuations at the larger bending rigidity.

The concentration of surface molecules near the bond is small, suggesting that the fluctuations are a consequence of fluctuations in z near the bond. For comparison, we also consider a system with a single bond and no surface molecules. For such a system, there is no driving force for the membrane to deform. Thus, the average membrane separation should be 13 nm throughout the domain and the average force on the bond should be negligible since the membrane is locally flat on average. In our simulations, the mean force on the bond is approximately 0 pN, as expected. We plot the distribution of forces in Fig. B.5 along with the mean-centered forces from the cases with surface molecules. The distributions are strikingly similar, which suggests that inherent shape fluctuations, independent of the surface molecules, drive the fluctuations in the force. It also underscores how a bond, even with zero average tension, can experience large forces due to shape fluctuations alone.

The physical picture that emerges from these results is that the evolving average shape of the membrane near the bond leads to a changing average tension on the bond. Fluctuations in z in the region surrounding the bond give rise to fluctuations in the bond tension, with the characteristic size of the force fluctuations similar to the characteristic size at an undeformed interface.

2.3.3 Catch bonds enhance binding times

Given the forces characterized above, we now investigate their impact on the binding times of different ligands relevant to OT1 T-cell activation. Fig. B.6 shows the average survival probability as a function of time for the three ligands shown in Fig. B.1. At zero applied force, the slip bond (E1) has the longest average lifetime, which is consistent with its survival probability being higher than the two stimulatory catch bonds (Fig. B.6A). When the slip bond experiences time-dependent forces, the bond ruptures more quickly (Figs. B.6B and B.6C), with bonds breaking almost immediately at the higher bending rigidity. At the lower bending rigidity, the survival probability decays more rapidly with fluctuations. Since the time-dependence of the average force is similar both with and without fluctuations, fluctuations involving larger forces increase the likelihood of bond rupture and enhance the decay of $S(t)$.

When forces are taken into account (Figs. B.6B and B.6C), both catch bonds (OVA and A2) are far more likely to remain intact than E1. Furthermore, OVA, which is the more potent agonist,

is more likely to remain intact than A2. At $\kappa = 12.15\ k_BT$, the survival probabilities for catch bonds decay more quickly when thermal fluctuations are taken into account. At $\kappa = 40\ k_BT$, the survival curves with fluctuations initially decay more slowly, but eventually fall below the curves without fluctuations. The initial decay is consistent with the average force plots (Fig. **??**), where the difference in the average force is most pronounced at short times for $\kappa = 40\ k_BT$. At longer times, when fluctuations are neglected, the average force decays to values close to the peak of the lifetime curve (Fig. B.1). However, for the case with fluctuations, even though the average force leads to relatively long lifetimes, the fluctuations enhance the likelihood of bond rupture.

Thus, the physical picture that emerges is that thermal fluctuations lead to faster relaxation of the membrane and a more rapid decrease in the average force on a bond. This can have the effect of enhancing the survival probability of a bond at short times, as for the catch bonds with $\kappa = 40\ k_BT$. However, if the average force on the bond is close to the force that maximizes the lifetime, the fluctuations lead to a smaller average lifetime.

2.3.4 The distance between bonds impacts bond tensions and survival probabilities

When a T cell interacts with another cell, multiple TCRs are likely to engage pMHC and mutually influence each other's behavior. In this section, we investigate cooperative effects by introducing a second bond that is separated by a fixed distance (20, 40, 80, and 160 nm). As before, we characterize how the separation distance influences membrane organization, forces on the bonds, and survival times of the bonds. Fig. B.7 shows snapshots and kymographs of the surface molecule concentration and distance profile for two bonds separated by 160 nm. At this distance, a separate depletion zone forms around each bond at short times, but by 1 s, the depletion zones merge with each other. A single domain develops at shorter times for all cases in which the bonds are closer.

Fig. B.8 shows the characteristic size of the depletion zone (d) at various distances between the bonds. As for a single bond, stiffer membranes lead to larger depletion zones. Additionally, thermal fluctuations expedite the formation of depletion zones at $\kappa = 40\ k_BT$. With separations of 20, 40, and 80 nm, a single depletion zone forms at short times. It takes longer to form a single

domain for the largest separation (160 nm), which is reflected by the delayed increase in the size of the depletion zone. The drive to form a single domain is a consequence of the larger bending energy associated with having two minima in z rather than a single domain. If the separation between the two bonds is small, the intermembrane distance profile quickly adopts a single minimum and surface molecules rapidly vacate the region between the bonds. As the distance between bonds increases, there is a smaller driving force to form a single depletion zone because the energetically unfavorable perimeter of the region grows. At sufficiently large bond separations, the domains would remain approximately independent. At small κ, the driving force to form a single domain is also smaller, and hence the surface molecules persist for longer in the region between the bonds.

The distance between the bonds affects the time-dependent tension experienced by each bond in the system. Fig. B.9 compares the average force on a bond given that a second bond is 20 nm or 160 nm away. The force is reduced when the bonds are close to one another, and the tension is similar to that of a single bond when the bonds are well separated. Table B2 shows the average force at long times on a bond for various separation distances. The average force increases as the separation distance increases. When two bonds are sufficiently close, they share the load associated with deforming the membrane, and each experiences a smaller force than a single, isolated bond.

For each distance separating the two bonds, we characterize the average survival probability over time for a bond given that the other bond remains intact. Fig. B.10 shows the fraction of bonds that remain after 1 s (denoted by ϕ) for each survival probability curve. Thermal fluctuations reduce ϕ for all cases considered. At $\kappa = 12.15\ k_{\mathrm{B}}T$, load sharing between two catch bonds (at separation distances of 20, 40, and 80 nm) decreases the fraction bound in the absence of fluctuations but has minimal influence when fluctuations are present. This is because the average force when two bonds are close gives an effective lifetime that is similar to the zero-force case (shorter lifetime). However, fluctuations sample a broader distribution of lifetimes, weakening the dependence on the average force. At $\kappa = 40\ k_{\mathrm{B}}T$, load sharing between two catch bonds enhances the binding fraction both with and without fluctuations. This is because the average force at long times is close to the force that maximizes the lifetime of the bond. For all cases, the slip bond is significantly less likely to remain intact at 1 s.

2.4 Discussion

The results above describe the time-dependent force experienced by bonds tethering two membranes when bond formation drives changes in membrane shape and organization of surface molecules. Given recent experimental data that measured the average force-dependent lifetime of a TCR bound to various ligands (76), we characterized resulting bond rupture distributions using the dynamically changing tension on the bond. For all of the cases we considered, the forces on the bonds lead to a higher survival probability of catch bonds (OVA and A2) compared with the slip bond (E1). This is in contrast to their behavior at zero force, when the slip bond remained intact longer on average. In this section, we further discuss features of the force fluctuations, the role of catch bonds in buffering fluctuations, and collective effects when multiple bonds are present.

In Fig. B.5, we showed that the mean-centered distribution of forces on a single bond was strikingly similar to the force distribution with no surface molecules present. This similarity holds despite the different average force experienced by the bonds in the two cases. Thus, even though the average shape of the membrane leads to a nonzero force on the bond when surface molecules are present, the fluctuations in shape lead to the same distribution of fluctuations about the mean. The characteristic size of force fluctuations is also similar when multiple bonds are present (Table 2).

It is interesting to view the survival probability curves in the context of the force fluctuations. Due to large fluctuations, the bonds occasionally experience forces far exceeding the average force. For large forces, the off rate grows exponentially, $k_{\text{off}}(f) \approx k_s \exp(f/f_s)$. Thus, a concern might be that large forces might effectively sever the bond due to the large off rate. We have tested the effect of the sampling time by recalculating the survival probability curves using the force at every other time point (doubling the sampling time). This has the effect of making fluctuations longer-lived, yet we find marginal changes in the survival probability curves. Thus, there is no evidence that outliers in the rupture probability significantly alter the survival curves. Additionally, this provides support for the assumption of mechanical equilibrium of the membrane, as fluctuations that stay correlated over longer times do not significantly change the survival probability curves.

Our results suggest that catch bonds may buffer against thermal fluctuations when compared with slip bonds. For example, consider an average bond tension that is close to the force

maximizing the bond lifetime. The slope of the lifetime curve is small (Fig. **??**), and thus small fluctuations in the force do not significantly affect the off rate. To further explore this, consider the effective off rate given an average force (f_A) on a bond. Assuming a Gaussian distribution of fluctuations, we can write the ratio of the effective (average) off rate to the off rate evaluated at the average force as

$$\frac{\langle k_{\text{off}}(f_A)\rangle_f}{k_{\text{off}}(f_A)} = \frac{1}{k_{\text{off}}(f_A)\sqrt{2\pi\sigma^2}} \int_{-\infty}^{\infty} df\, k_{\text{off}}(f_A+f) \exp\left(-\frac{f^2}{2\sigma^2}\right). \tag{2.7}$$

Using Eqns. 2.1 and 2.2 for $k_{\text{off}}(f)$, we computed this quantity for the three different ligands using values of σ obtained from simulations. Fig. B.13 shows the value of this ratio for a range of f_A. For all values of f_A, the ratio is largest for the slip bond. Thus, fluctuations increase the effective off rate of the slip bond by the greatest factor, and the catch bonds suppress the effects of force fluctuations in comparison.

We can further evaluate the effective off rate at large values of the force. In particular, for catch bonds with $f_A \gg f_c$, averaging over the fluctuations gives

$$\frac{\langle k_{\text{off}}(f_A)\rangle_f}{k_{\text{off}}(f_A)} = \exp\left(\frac{\sigma^2}{2f_s^2}\right) \tag{2.8}$$

Thus, the effective off rate is larger than $k_{\text{off}}(f_A)$, with broader distributions (larger σ) leading to higher effective off rates. Note that the catch bonds have values of f_s approximately two times larger than the corresponding parameter (f_0) in the slip bond model. For a given value of σ, the larger value of f_s suppresses the ratio for the catch bonds in comparison with the slip bond. From Fig. S3, it can be seen that this approximation is good when $f \gtrsim 15$ pN.

When a T cell interacts with an antigen-presenting cell, multiple TCRs are likely to interact with a variety of pMHCs, including many with endogenous peptides that are not stimulatory. In the previous section, we showed that a second bond reduced the average force on each bond when they were sufficiently close. To further explore cooperative binding effects, we added a third bond to the system and focused on a configuration in which the three bonds are colinear. Table B3 contains the average forces on the middle bond and the two other bonds, which we call "edge bonds." It is interesting to note that when the receptors are close, the bond in the middle experiences a

negative average force. The two edge bonds lead to an average configuration that, in the absence of the middle bond, would adopt a minimum intermembrane distance (z) smaller than the bond length (z_0). Including the middle bond forces the membrane to deviate upward, which leads to a compressive average force on the bond.

The case of three bonds highlights the importance of characterizing the dissociation kinetics of a bond under a compressive force. To our knowledge, there has been no extended study or discussion of catch bonds under compressive forces. In this work, we assumed that the off rate was an even function of force, $k_{\text{off}}(-f) = k_{\text{off}}(f)$. For comparison, we also considered the case in which negative forces were treated as equivalent to the zero-force case. For a single bond, the assumption had little effect, as most forces sampled were positive. Because of the ambiguity regarding bonds under compressive force, we did not construct survival curves for the cases without surface molecules ($\langle f \rangle = 0$) or for the cases with three bonds ($\langle f \rangle < 0$ for the center bond). Experimental investigations of bonds under compressive force would be useful given the high likelihood that receptor-ligand bonds at intermembrane junctions experience both positive and negative forces. Such forces may arise due to membrane deformations, shape fluctuations, and active processes such as those mediated by the actin cytoskeleton.

2.5 Conclusion

A growing body of work has revealed the importance of forces in T-cell activation. Recent experiments measuring the force-dependent lifetimes of TCR-pMHC bonds have revealed the surprising finding that TCRs can behave as catch bonds when bound to stimulatory pMHCs. This is suggestive from a mechanistic standpoint, as force-dependent regulation of TCR-pMHC binding times provides a physical mechanism that could help T cells discriminate between self and foreign peptides.

Our approach provides a way to characterize the impact of surface molecule reorganization and membrane shape changes over times relevant to the earliest stage of T-cell activation. We focused on immobile bonds to carefully characterize the time-dependent forces over a 1 s time period. In reality, TCR-pMHC bonds can diffuse and are influenced by the actin cytoskeleton, although actin-mediated forces initiated by TCR engagement are likely most relevant at later times

(52). Both receptor mobility and actin-mediated forces will be interesting features to consider in the future theoretical settings.

Our results indicate that agonist catch bonds are more likely to remain intact than an antagonist slip bond when the bonds experience a time-dependent and fluctuating force. After initial cell-cell contact, the presence of a single TCR-pMHC bond that is sufficiently long-lived could promote the formation of other TCR-pMHC bonds nearby, as the local intermembrane distance accommodates the bond formation. This could lead to an effective feedback and clustering mechanism in which the new bonds would reinforce the contact between the cells by sharing the load of deforming the membrane. Furthermore, the encounter times remain short enough to enable serial engagement by the pMHC (1, 99, 137, 143). We anticipate that continued experimental progress and theoretical developments will lead to a better understanding of the mechanical modulation of TCR binding kinetics, which will enhance our understanding of how T cells act as specific and sensitive detectors of antigen.

Chapter 3

Dynamics of T-cell receptor cluster formation

3.1 Introduction

T cells use membrane-anchored receptors (TCRs) to distinguish foreign antigens with high sensitivity amongst a sea of non-stimulatory antigens. It has been proposed that TCRs may experience a tensile force after engaging a processed peptide fragment presented by the major histocompatibility complex (pMHC) to amplify differences between stimulatory and nonstimulatory ligands (37, 106, 144). There have been a number of recent experiments that characterized the binding kinetics of TCR-pMHC interactions as well as the formation of TCR microclusters. Stimulatory TCR-pMHC complexes exhibit force-dependent catch-bond behavior, where the TCR-pMHC complex lifetime is maximized at a nonzero tensile force, typically $\sim 10-15$ pN (54, 76). This is in direct contrast to the more common slip bond whose average bond lifetime decreases monotonically with an increasing tensile force (11).

The kinetic segregation model posits that the difference in the natural length of TCR-pMHC complexes in comparison to other key proteins, such as the CD45 phosphatase, energetically drives spatial reorganization within the intercellular junction to form distinct domains for proteins of similar length (21). In addition to the development of separate protein domains, Pageon et al. demonstrated that the formation of TCR microclusters most likely precedes phosphorylation events (100). Interestingly, density of pMHC on the antigen-presenting cell has been observed

to impact T-cell activation and proliferation (33, 129). How the spatial formation of TCR microclusters couples with receptor-ligand binding kinetics, protein reorganization, and membrane mechanics at the cell-cell interface remains an open question in immunology.

In this work, we use a computational framework to investigate the impact of catch bonds versus slip bonds as the formation of TCR microclusters at the cell-cell interface. When possible, we use experimentally-derived parameters to describe the underlying biophysics of TCR microcluster formation. We expand upon our previous model to allow for stochastic receptor-ligand binding events and TCR-pMHC diffusion (107). In the results, we characterize TCR microcluster spatial organization given a wide range of pMHC densities on the target cell surface.

3.2 Model formulation

3.2.1 Membrane dynamics

We consider a framework in which a T cell is in close proximity to a patch of an antigen-presenting cell surface Fig. C.1. The two membranes are modeled as continuum surfaces characterized by a bending rigidity, κ, that penalizes membrane deformations. We describe the separation of the two membranes by an intermembrane distance profile, $z(x,y,t)$. The energy of the system is dependent upon the curvature of the intermembrane distance profile, and the presence of TCR-pMHC complexes or long surface molecules (i.e. CD45) within regions of the intercellular junction different than their natural lengths,

$$E[z, C_{\text{CD45}}, C_{\text{bond}}] = \iint dx\, dy \left(\frac{\kappa}{2}\left(\nabla^2 z\right)^2 + k_{\text{bond}} C_{\text{bond}} \left(z_{\text{bond}} - z\right)^2 + k_{\text{CD45}} C_{\text{CD45}} \left(z_{\text{CD45}} - z\right)^2 \right).$$

C_{CD45} and C_{bond} are the concentrations of CD45 phosphatases and bonds, respectively. k_i and z_i are the compressional stiffnesses and equilibrium lengths of the chemical species, respectively. We use the time-dependent Ginzburg Landau (TDGL) model to describe the evolution of the intermembrane distance profile

$$\frac{\partial z}{\partial t} = -M \frac{\delta E}{\delta z} + \zeta$$

Here M is a phenomenological constant, which sets the timescale for membrane relaxation, and ζ is the thermal noise in the system. The TDGL model can account for dynamics in which the timescale for the reorganization of proteins within the intercellular junction is on the same order as membrane relaxation. Implementing a forward time-marching method with a central finite difference scheme, we solve for the updated intermembrane distance profile at each lattice site before progressing to the next time step.

3.2.2 Receptor-ligand dissociation kinetics

As previously mentioned, nonstimulatory ligands result in the formation of slip bonds whose lifetimes decrease exponentially with an applied tensile force and are characterized by the Bell model (11):

$$k_{\text{off}}^{\text{slip}}(f) = k_0\, e^{f/f_0}.$$

Here, k_0 is the intrinsic off rate at zero applied force, f is the applied tensile force on the TCR-pMHC complex, and f_0 is the reference force. The two-pathway model is commonly applied to account for the dissociation kinetics of TCR-pMHC complexes that exhibit catch bond behavior (104),

$$k_{\text{off}}^{\text{catch}}(f) = k_c\, e^{-f/f_c} + k_s\, e^{f/f_s}$$

where c and s denote catch- and slip-phase parameters, respectively.

3.2.3 Coupling of the TDGL model with reaction-diffusion equations

In the TDGL model, the intermembrane distance profile at a rate proportional to the functional derivative of the free energy with respect to the membrane shape. When expanded, the expression for the intermembrane distance profile is depends on the concentration of long surface molecules and catch/slip bonds:

$$\frac{\partial z}{\partial t} = -M\Big[\kappa\nabla^4 z - k_{\text{CD45}}C_{\text{CD45}}(z_{\text{CD45}} - z) - k_{\text{bond}}C_{\text{bond}}(z_{\text{bond}} - z)\Big] + \zeta$$

The time evolution of all chemical species are modeled as reaction-diffusion equations which are coupled to the intermembrane distance profile,

$$\begin{aligned}
\frac{\partial C_{\text{ag}}}{\partial t} &= D_{\text{ag}}\nabla^2 C_{\text{ag}} - k_{\text{on}}(z)C_{\text{ag}}C_{\text{TCR}} + k_{\text{off}}^{\text{catch}}(f)C_{\text{catch}} \\
\frac{\partial C_{\text{catch}}}{\partial t} &= D_{\text{bond}}\nabla^2 C_{\text{catch}} + \frac{D_{\text{bond}}}{k_{\text{B}}T}\nabla\cdot\Big[C_{\text{catch}}\nabla\frac{1}{2}k_{\text{bond}}(z-z_{\text{bond}})^2\Big] + k_{\text{on}}(z)C_{\text{ag}}C_{\text{TCR}} - k_{\text{off}}^{\text{catch}}(f)C_{\text{catch}} \\
\frac{\partial C_{\text{CD45}}}{\partial t} &= D_{\text{CD45}}\nabla^2 C_{\text{CD45}} + \frac{D_{\text{CD45}}}{k_{\text{B}}T}\nabla\cdot\Big[C_{\text{CD45}}\nabla\frac{1}{2}k_{\text{CD45}}(z-z_{\text{CD45}})^2\Big] \\
\frac{\partial C_{\text{ns}}}{\partial t} &= D_{\text{ns}}\nabla^2 C_{\text{ns}} - k_{\text{on}}(z)C_{\text{ns}}C_{\text{TCR}} + k_{\text{off}}^{\text{slip}}(f)C_{\text{slip}} \\
\frac{\partial C_{\text{slip}}}{\partial t} &= D_{\text{bond}}\nabla^2 C_{\text{slip}} + \frac{D_{\text{bond}}}{k_{\text{B}}T}\nabla\cdot\Big[C_{\text{slip}}\nabla\frac{1}{2}k_{\text{bond}}(z-z_{\text{bond}})^2\Big] + k_{\text{on}}(z)C_{\text{ns}}C_{\text{TCR}} - k_{\text{off}}^{\text{slip}}(f)C_{\text{slip}} \\
\frac{\partial C_{\text{TCR}}}{\partial t} &= D_{\text{TCR}}\nabla^2 C_{\text{TCR}} - k_{\text{on}}(z)C_{\text{ag}}C_{\text{TCR}} - k_{\text{on}}(z)C_{\text{ns}}C_{\text{TCR}} + k_{\text{off}}^{\text{catch}}(f)C_{\text{catch}} + k_{\text{off}}^{\text{slip}}(f)C_{\text{slip}}
\end{aligned}$$

Here, $k_{\text{on}}(z)$ is the binding rate of the various TCR-pMHC interactions, and C_{ag} & C_{ns} are the concentrations of the agonist and non-stimulatory pMHC molecules, respectively.

To account for diffusion of TCR-pMHC complexes and the low number of chemical species in the system, we model molecules as discrete objects that diffuse by stochastically hopping on a lattice overlaid on the surface. The diffusion coefficient of proteins, D, on the surface is related to a stochastic hopping rate by $\gamma = D/(\Delta x)^2$ in the absence of an energetic gradient. Given that bonds are less likely to diffuse to a region that leads to an increase in energy, the modified rate of hopping, based on the master equation discretization method of Grima and Newton, can be written as (43)

$$\gamma_{i\to j} = D/(\Delta x)^2 \exp[-\beta(E_j - E_i)/2].$$

We will allow TCR-pMHC bonds to form when a discrete TCR interacts with a discrete pMHC molecule on the same lattice site, given that the membrane separation at that site is less than $2z_{\text{bond}}$. We assume the binding rate of the TCR-pMHC bond decays with membrane-sepation distance as a Gaussian, centered about the natural length of the TCR-pMHC complex,

$$k_{\text{on}}(z) = k_{\text{on}}^0 \exp\Big[-\frac{(z-z_{\text{bond}})^2}{2\sigma^2}\Big]. \tag{3.1}$$

Here, k_{on}^{0} is the intrinsic on-rate that is associated with the TCR-pMHC interaction and σ is a characteristic decay length, which is set to 5 nm. Bonds dissociate stochastically, with the off rate determined by the time-dependent tension on the bond. As bonds break, there is reorganization of long surface molecules and membrane shape, thus affecting the tension on other bonds. Thus, this hybrid computational model combines the Gillespie algorithm to simulate diffusion and binding / unbinding of discrete TCR, pMHC, and TCR-pMHC complexes while the TDGL model accounts for updates to the intermembrane distance profile. Parameters used in the model are summarized in Table C1.

3.3 TCR cluster formation is highly dependent on the fraction of agonist pMHC molecules

Figure C.2 tracks the changes in the intermembrane distance profile (z) at several time points during the simulation. The formation of TCR-pMHC complexes rapidly induces changes in both the membrane shape and spatial organization of CD45 phosphatases in agreement with previous studies (2, 107). This case represents an extreme, where both the fraction of agonist pMHC and density of pMHC molecules on the antigen-presenting surface are high (i.e. $\phi_{VSV8} = 1.00$ and $\rho_{pMHC} = 1000$ molecules/μm^2). As time progresses, smaller TCR-pMHC clusters coalesce to form larger aggregates. The combination of the initial proximity of the two membranes and the high density of the pMHC molecules on the surface cause an immediate growth of TCR-pMHC complexes Fig. C.3. Interestingly, we observe that average number of TCR-pMHC complexes in the system fluctuate about a value dependent on the fraction of agonist peptide. By comparing Figs. C.2 and C.3, we come to the conclustion that as the number of individual clusters decreases with the progression of time, the average number of TCR-pMHC complexes in a given cluster correspondingly increases.

It is likely that TCR-pMHC complexes aggregate together to decrease both the energetic penalty of membrane curvature and form domains where the intercellular junction is close to their natural length. We next tracked the spatiotemporal organization of key proteins, namely the TCR-pMHC complexes and CD45 phosphatases. Fig. C.4 shows snapshots of the locations

of TCR-pMHC complexes (white) and CD45 phosphatases (red) within the system. As smaller clusters coalesce, CD45 phosphatases are energetically driven away from membrane patches of close apposition. By $t = 2\ s$, we observe significant segregation between the longer surface molecules and shorter TCR-pMHC complexes, thus supporting the kinetic segregation model.

Taken together, these results show the hybrid computational model is capable of observing spatial reorganization of proteins at the intercellular junction and the formation of TCR microclusters. The T cell encounters a large variety of target surfaces, and likely uses the spatial patterning of TCR-pMHC complexes to translate information to downstream signaling (100). It will be useful to investigate how the system dynamics are altered as a function of pMHC density, TCR-pMHC binding kinetics, and membrane stiffness to further the mechanistic understanding of TCR cluster formation.

Chapter 4

Mechanical feedback enables catch bonds to selectively stabilize scanning microvilli at T-cell surfaces

Summary: This chapter is based on the submitted paper by Robert H. Pullen, III and Steven M. Abel: Pullen III, Robert H., and Steven M. Abel. *Mechanical feedback enables catch bonds to selectively stabilize scanning microvilli at T-cell surfaces*. Manuscript currently under review.

4.1 Introduction

T cells directly engage antigen-presenting cells (APCs) to search for surface-displayed antigens. They use the T-cell receptor (TCR) complex to discriminate between self and foreign ligands in the form of peptides presented by major histocompatibility complex (pMHC) molecules on the APCs. T cells are able to recognize small numbers of antigens amongst a vast number of self-pMHCs (53, 100, 130) while being sensitive enough to distinguish between peptides with a single amino acid difference (49, 111). However, a comprehensive understanding of the mechanisms governing antigen recognition remains elusive, and growing evidence points to the importance of mechanical forces at the T cell-APC interface (34, 48, 136).

Recent experiments have revealed two intriguing physical mechanisms related to antigen recognition: (i) T cells use microvillar protrusions to actively search APCs, suggesting a

mechanism to scan large portions of the APC surface (22). (ii) The average lifetime of a bond between a TCR and an antigenic pMHC is maximized when there is an applied force on the TCR-pMHC complex (31, 76). Taken together, these results suggest feedback between microvillar motion and TCR-pMHC binding: Forces imparted by microvillar motion influence TCR-pMHC lifetimes, while tensions on individual TCR-pMHC complexes impact microvillar motion. To our knowledge, this feedback and its consequences have not been explored before.

Microvilli are fingerlike membrane protrusions that have been observed on T cells in a variety of studies (22, 48, 63, 68, 109, 116). They also contain large numbers of highly localized TCRs (63, 68), and a recent study using lattice light-sheet microscopy revealed that T cells use microvilli to actively scan the surfaces of APCs (22). Interestingly, this study showed that cognate pMHC on the APC resulted in some microvilli becoming "stabilized," with long-lived contact at localized regions on the APC surface. This stabilization occurred even when early intracellular signaling through the TCR was disrupted, suggesting that a physical mechanism might be responsible. Taken together, these studies suggest that microvilli play a role in antigen discrimination during early stages of T-cell activation.

Physical contact between the T cell and APC leads to mechanical forces at the cell-cell interface. TCR-pMHC complexes experience forces that arise from a variety of sources including cell motion, membrane undulations, active cytoskeletal processes, and the microvillar motion described above (48, 107). A number of recent experimental studies have characterized the force-dependence of individual TCR-pMHC dissociation kinetics (31, 34, 37, 50, 51, 54, 76, 125). When bound to stimulatory pMHC, the TCR exhibits catch-bond behavior, in which the average lifetime is maximized when a force $\sim$10 to 20 pN is applied to the protein complex. In contrast, a TCR bound to a nonstimulatory pMHC exhibits slip-bond behavior, in which the lifetime strictly decreases with increasing force. The ligand- and force-dependence of the dissociation kinetics has been proposed as a potential mechanism to enhance discrimination between self and foreign pMHC (38, 76).

In this paper, we investigate the mechanical coupling between microvillar motion and TCR-pMHC binding. We are interested in whether the interplay between the two provides a physical mechanism that could impact antigen recognition. To this end, we introduce a physically-motivated theoretical framework describing the motion of a microvillus near an antigen-presenting surface.

The framework captures key biophysical features while being simple enough to analyze in detail. When possible, we use experimentally-derived parameters, including those for force-dependent TCR-pMHC dissociation kinetics. In the results, we first characterize the motion of scanning microvilli in the presence of surfaces containing nonstimulatory (slip) pMHC, stimulatory (catch) pMHC, and mixtures of the two. We characterize the distribution of velocities for different cases and assess when an individual microvillus has stopped. We then characterize the total time of receptor engagement as a proxy for the degree of stimulation of TCRs at the microvillus tip. We conclude by discussing some assumptions of the model, the physical picture that emerges from our simulations, and potential implications for antigen recognition by T cells.

4.2 Methods

We consider a theoretical framework in which an isolated microvillus scans across an antigen-presenting surface. The velocity of the microvillus depends on the forces exerted on the microvillus by TCR-pMHC complexes ("bonds"). The number of bonds, bond lifetimes, and microvillus velocity are dependent upon the interplay between stochastic binding events, diffusive processes, and forces that result from the stretching and compression of bonds by the moving microvillus. We use a stochastic reaction-diffusion framework that accounts for the microvillus motion and the forces on TCR-pMHC bonds.

4.2.1 Computational framework

Figure D.1 provides a schematic depiction of the model. We represent a patch of the antigen-presenting surface as a rectangular domain in which pMHC molecules diffuse. The tip of the T-cell microvillus is represented by a circular surface with a diameter of 100 nm (39, 63, 82, 109). We assume that it resides at a fixed distance above the antigen-presenting surface, which we take to be the length of a TCR-pMHC complex (z_{bond}). TCRs diffuse about the microvillus tip and bind to pMHC molecules on the antigen-presenting surface. TCRs and pMHCs are represented by particles with a 5 nm radius (14), and particles on the same surface cannot overlap due to excluded volume. When TCR-pMHC bonds are stretched relative to their natural length, they impose a force on the microvillus. We describe the force with a linear spring model, $f = k_{\text{bond}}(L - z_{\text{bond}})$, where

k_{bond} is the spring constant, L is the distance between the two bound particles, and the force is directed along the bond.

The microvillus tip moves across the antigen-presenting surface in the x-direction. In the absence of an external force, the microvillus moves at velocity V_0. However, forces arising from TCR-pMHC bonds impact the microvillus velocity, which we assume depends linearly on the component of the net force in the x-direction, $f_x(t)$:

$$V_{\text{MV}}(t) = V_0 \left(\frac{f_{\text{MV}} + f_x(t)}{f_{\text{MV}}} \right) . \tag{4.1}$$

Here, f_{MV} is a characteristic force and the time-dependence of f_x is a consequence of the formation, stretching, and breaking of bonds. We assume that active processes driving the microvillus keep it in close apposition to the APC surface, and thus we neglect motion in the z-direction. Additionally, we ignore velocity fluctuations in the y-direction, as these would average to zero and can be thought of as changing the frame of motion of the microvillus. Physically, for an individual TCR-pMHC bond, when the pMHC is "in front of" the TCR ($x_{\text{pMHC}} > x_{\text{TCR}}$), it effectively pulls the microvillus forward and increases the velocity. When the pMHC is "behind" the TCR, it decreases the velocity. The linear dependence of the velocity on force is consistent with the terminal velocity of an object experiencing a viscous drag. We discuss this choice and the results of a different functional form for V_{MV} later in the paper.

We use a discrete-time, continuous-space stochastic algorithm to describe the dynamics of the system. During each time step, the algorithm accounts for diffusive hops of particles, binding events, and dissociation of bonds. At the end of each time step, the position of the microvillus is updated in accordance with its velocity, which impacts the state of the system by changing the lengths of TCR-pMHC bonds and the positions of TCRs relative to the antigen-presenting surface. Details of the algorithm are presented Appendix B.

Parameters used in the model are summarized in Table D1. The system size is $200\,\text{nm} \times 5\,\mu\text{m}$, which is sufficiently long for the microvillus tip to remain within the domain. The total pMHC concentration is fixed at 100 pMHC/μm^2 (24, 42, 99), and the microvillus tip contains 23 TCRs (63). The state of the system is recorded every 2.5×10^{-4} seconds.

4.2.2 TCR-pMHC binding kinetics

In the model, TCR-pMHC dissociation kinetics are described by the Bell model for slip bonds (nonstimulatory pMHCs) and by the two-pathway model for catch bonds (stimulatory pMHCs). The off-rate in the Bell model is characterized by (11)

$$k_{\text{off}}^{\text{slip}}(f) = k_0 e^{f/f_0} \,, \tag{4.2}$$

where k_0 is the off-rate at zero applied force, f is the force on the receptor-ligand complex, and f_0 is the reference force. The off-rate in the two-pathway model is characterized by (104)

$$k_{\text{off}}^{\text{catch}}(f) = k_c e^{-f/f_c} + k_s e^{f/f_s} \,, \tag{4.3}$$

where c and s denote catch- and slip-phase parameters, respectively.

We parameterized experimental bond-lifetime data from two previous studies that showcase catch- and slip-bond binding characteristics. Liu et al. used a biomembrane force probe to characterize the interactions of the OT1 TCR with a panel of pMHCs that ranged from a nonstimulatory peptide (E1) to a strongly stimulatory peptide (OVA) (76). Feng et al. utilized optical tweezers to investigate interactions of the N15 TCR with the stimulatory vesicular stomatitis virus octapeptide (VSV8) presented by the MHC class I molecule H-2K$^{\text{b}}$ (37). Figure D.2 shows the average bond lifetime as a function of tensile force for the cases we consider in this paper. We also consider a hypothetical slip bond ("strong slip") with the same maximum lifetime as a VSV8 catch bond and the same reference force as the E1 slip bond. The strong slip bond is used as a control to determine if a slip bond with a large zero-force lifetime behaves similarly to the catch-bond cases. For convenience, we refer to the two catch bonds and the strong-slip bond as "stimulatory." Parameters for the different cases are tabulated in the Appendix B.

To characterize binding rates, we use data from Huang et al. (54), which reports effective 2D on-rates for the OT1 TCR binding to OVA and to E1 pMHC (Table D1). We use the on-rate reported for OVA to describe the binding of all stimulatory pMHC in this study (OVA, VSV8, and "strong slip").

4.3 Results

In this section, we characterize the collective effects of catch and slip bonds on the motion of of microvilli. The total pMHC concentration is fixed at 100 μm^{-2} throughout. For reference, we consider an antigen-presenting surface containing only nonstimulatory ligands with slip-bond kinetics. We then mimic varying degrees of stimulation by replacing 10%, 20%, 30%, and 100% of the nonstimulatory pMHCs with stimulatory pMHCs (either VSV8, OVA, or strong slip). For each condition, we generate 25 independent trajectories to assess stochastic effects.

4.3.1 Scanning microvilli are slowed in a ligand-dependent manner

Figure D.3 shows the average microvillus displacement over time for the three different stimulatory pMHCs at various fractions of the total concentration. The green line (0% stimulatory pMHC) represents the average microvillus position when only nonstimulatory slip bonds are present. For this case, the average displacement grows linearly in time with a velocity of 3.5 μm/min, which is less than the zero-force velocity of the microvillus ($V_0 = 5.2$ μm/min). From Eqn. 4.1, the average velocity is consistent with the nonstimulatory TCR-pMHC bonds exerting an average net force of approximately 16 pN in the direction opposed to the microvillus motion.

The average displacement of the microvillus decreases as the fraction of stimulatory pMHCs increases. VSV8 leads to the most pronounced decrease in microvillus displacement, with increasing fractions of VSV8 leading to slower average microvillus movement. For 100% VSV8, the average displacement is nearly completely arrested after a short time. OVA generates similar behavior with smaller relative changes as the fraction of OVA is changed. The strong-slip case shows the weakest change in the average displacement as its fraction increases.

4.3.2 Heterogeneity of microvillus trajectories

Stochastic binding and dissociation events lead to differences in the motion of microvilli even at identical conditions. Figure D.4 shows the time-dependent positions of microvilli from multiple independent simulations. When only nonstimulatory pMHCs are present (Figure D.4A), there is relatively small variation between individual displacements and the average microvillus displacement. However, when the fraction of VSV8 pMHC is 10%, there is markedly more

variation between individual microvillus displacements. One particularly striking feature is that some trajectories plateau for sustained periods of time. During these periods, the microvillus is approximately stationary due to forces exerted by TCR-pMHC bonds. When the fraction of VSV8 pMHC is 30%, a greater fraction of microvilli become effectively immobile within the one-minute period, which further decreases the average microvillus displacement. Analogous figures with OVA and strong-slip pMHC are shown in Figure S1.

Movies S1 and S2 show sample trajectories at 10% and 30% VSV8 pMHC, respectively. In each, the microvillus experiences a period during which it is nearly stationary. For these cases, it can be seen that binding a small number of catch bonds significantly impacts the velocity of the microvillus. Once the catch bonds significantly slow the microvillus, additional slip bonds accumulate over time.

4.3.3 Catch bonds stabilize microvilli

Figure D.5 characterizes distributions of the microvillus velocity for different types and fractions of stimulatory pMHC. When only nonstimulatory pMHCs are present (green line), the velocity distribution is approximately normal with a velocity of 3.48 ± 1.08 μm/min (mean $\pm$ SD). Figure D.5A shows how the presence of VSV8 pMHC changes the velocity distributions. At 10% VSV8, a small peak in the probability density emerges near 0 μm/min, which is associated with stationary ("stabilized") microvilli. As the fraction of VSV8 increases, both the number and duration of immobile microvilli increase, leading to more prominent and narrower peaks. Results for OVA (Figure B.S2) are similar but less pronounced. Figure D.5B compares distributions of the velocity for systems containing varied fractions of strong-slip pMHC. Although larger fractions of strong-slip pMHC decrease the average velocity, in contrast with Figure D.5A, the velocities extend across a broad range with no peak near 0 μm/min. Thus, even large fractions of strong-slip pMHC do not result in the effective immobilization of microvilli.

To further characterize the stabilization of microvilli by stimulatory pMHC, we determine the probability that a microvillus effectively stops during the course of a simulation (Figure D.6). We define a "stopping event" to be when a microvillus has an average velocity ≤ 0.25 μm/min for a continuous period of at least 10 s. Varying the thresholds for the average velocity and the time

interval did not affect our conclusions. Figure D.6 shows that the microvillus did not stop for any fraction of strong-slip pMHC. However, stopping does occur when stimulatory pMHC with catch bond characteristics (OVA and VSV8) are present. For OVA, stopped microvilli are observed at 20% OVA, and there is a significant increase in the number of stopped microvilli at larger fractions of OVA. For VSV8, stopped microvilli are observed at all fractions of VSV8, with larger fractions increasing the likelihood of stopping.

4.3.4 Catch bonds impact cumulative TCR-pMHC binding times

In Figure D.7, we examine the time-dependent displacement of a microvillus concurrently with the number of slip and catch bonds. Figure D.7A shows a case with only nonstimulatory pMHC present. Although the number of slip bonds varies during the simulation, the slope of the microvillus displacement remains relatively constant. This is consistent with a rapid turnover of bonds, in which they frequently form and break. Figures D.7B and D.7C correspond to trajectories with 10% and 30% VSV8 pMHC, respectively. These two sample trajectories correspond to Movies S1 and S2. In both cases, when two or more catch bonds form, the microvillus slows dramatically. After the microvillus is initially stabilized, there is a gradual accumulation of additional slip bonds. In Figure D.7B, the sudden increase in velocity at late times is coincident with the breaking of catch bonds and a rapid decrease in the number of slip bonds. Figure B.S3 shows the average number of catch and slip bonds as a function of the microvillus velocity. These results are consistent with TCR-pMHC bonds accumulating at stabilized microvilli: In systems with catch bonds, slower velocities have larger average numbers of TCR-pMHC bonds.

Our results indicate that catch bonds selectively stabilize scanning microvilli in a stochastic manner and that TCR-pMHC bonds accumulate when the microvillus is stopped. This suggests a physical mechanism that could link the motion of the microvillus to intracellular processes through receptor engagement. As a proxy for the degree of stimulation through the TCR, we calculate the cumulative time of receptor engagement as a function of time for each trajectory:

$$\text{Time engaged}(t) = \sum_{i=1}^{n_{\text{bonds}}} \left(t - t_{i,0}\right) . \tag{4.4}$$

Here, n_{bonds} is the number of bound TCRs at time t, and $t_{i,0}$ is the time of bond formation for a given TCR-pMHC complex. Thus, at time t, this function gives the total time that all current TCR-pMHC complexes have been present. Given the results on microvillus stopping in Figure D.8, we analyze trajectories with and without stopping events separately to provide insight into the effects of microvillar stabilization by catch bonds.

When only nonstimulatory slip bonds are present, the average cumulative time engaged is 0.26 s. Figure D.8A shows the average time of engagement for trajectories with a microvillus-stopping event for various fractions of VSV8 pMHC. The average time engaged increases with increasing fraction of stimulatory pMHC, exceeding 10 s for 30% VSV8. Note that these curves underestimate the typical time engaged for a specific stabilized microvillus because the average occurs over periods in which some microvilli are stopped and others are not. In comparison, Figure D.8B shows a substantially smaller average time engaged for trajectories in which the microvillus does not stop. Figure D.8C shows the average time engaged for systems with various levels of strong-slip pMHC, which did not induce any stopping events. The time engaged increases with an increasing fraction of strong-slip pMHC, but in all cases, the time engaged is substantially lower than corresponding cases in which catch bonds resulted in a stopping event (Figure D.8A). Thus, systems with catch bonds are able to generate much longer sustained receptor engagement in comparison with even the strong-slip system.

4.4 Discussion

In this paper, we introduced a theoretical framework to explore the motion of a T-cell microvillus scanning across the surface of an antigen-presenting cell. TCRs at the tip of the microvillus interact with pMHCs on the antigen-presenting surface, and mechanical forces on the TCR-pMHC complexes resulting from motion of the microvillus impact both TCR-pMHC lifetimes and the microvillus velocity. Using parameters obtained from experimental studies of T cells, we showed that relatively small numbers of stimulatory pMHC with catch-bond characteristics immobilized microvilli in the model through mechanical coupling. In contrast, slip bonds alone did not immobilize microvilli. These results are exemplified by Figures D.5 and D.6, which show the distribution of velocities for scanning microvilli and the likelihood that a

microvillus becomes immobilized. The effects become more pronounced as the concentration of antigenic pMHC increases.

4.4.1 Choice of the velocity profile, V_{MV}

The mechanisms underlying microvillar motion on T cells have not been fully elucidated experimentally (20, 22, 82), so we chose to use a simple, physically motivated model relating the applied force to microvillar velocity. Our model uses a linear relationship between the velocity, V_{MV}, and the applied force in the direction of motion. This relationship is consistent with the terminal velocity (zero acceleration) of an object experiencing a viscous drag: $F_A + f_x - \mu V_{MV} = 0$. Here, F_A is a constant applied force driving the motion of the object (provided, for example, by cytoskeletal processes within the cell), f_x is the applied force due to bonds, and μ is the drag coefficient relating the velocity to the drag force μV_{MV}. Thus, $V_{MV} = (F_A + f_x)/\mu$, which is consistent with Eqn. 4.1.

The characteristic force in Eqn. 4.1, f_{MV}, is unknown. If f_{MV} is too small, then even single slip bonds would significantly slow the microvillus. If f_{MV} is too large, then even a large number of bonds would not be able to significantly slow the microvillus. Both of these limits are inconsistent with the results from Ref. (22). With these limits in mind, we chose the value to be a few times larger than both typical forces experienced by individual TCR-pMHC bonds (77) and the force associated with the peak lifetime for catch bonds (31, 76). Moderately changing the value of f_{MV} impacts quantitative aspects of our results, although it does not impact the observation that catch bonds selectively stabilize microvilli. Figure S4 shows this for 2-fold changes in the force threshold for purely stimulatory and nonstimulatory pMHC systems.

Other models for V_{MV} may also be appropriate. Another plausible mechanism includes a "stall force" such that applied forces below a threshold have little effect on the velocity, while forces above the threshold have a large effect. To this end, we also consider a velocity profile with a Hill-like (sigmoidal) form in the SI (text and Figure B.S4). This profile results in an even more pronounced impact of catch bonds due to the inability of nonstimulatory ligands to significantly slow the microvillus tip on their own.

4.4.2 A physical mechanism for microvillar stabilization and enhanced antigen discrimination

T cells exhibit remarkable specificity and sensitivity in their search for antigenic ligands, yet the underlying mechanisms are still not fully understood. A growing body of work has revealed that physical mechanisms involving mechanical forces may play an important role (48, 136). In this paper, we have explored feedback between microvillar motion and TCR-pMHC dissociation kinetics. We were intrigued by the results from Cai et al. (22), which revealed that T cells use microvilli to scan the surfaces of APCs and that the presence of cognate pMHC stabilized microvilli even in the absence of tyrosine kinase signaling, which is a key component of the early TCR signaling pathway. In light of recent single-molecule studies of TCR-pMHC binding kinetics (31, 76), we hypothesized that nontrivial force-dependent dissociation kinetics could potentially lead to the stabilization. To investigate this idea, we developed a model that captures key biophysical properties of the microvillus-APC interaction but that is simple enough for analysis.

Taken together, our simulation results reveal a purely physical mechanism—the mechanical coupling of microvillar motion and TCR-pMHC binding—that could enhance antigen recognition by T cells. The physical picture is that forces generated by scanning microvilli provide a means to mechanically "test" TCR-pMHC bonds connecting the microvillus tip to the antigen-presenting surface. The total force necessary to immobilize a scanning microvillus is too large for an individual TCR-pMHC complex to reach before rupture. Thus, if only a small number of nonstimulatory TCR-pMHC bonds are present, the microvillus will continue to move, constantly increasing the force on the bonds and promoting their rupture. Short engagement times would prevent intracellular signaling through the TCR pathway.

In contrast, when a TCR binds to a stimulatory pMHC, the resulting catch bond is able to withstand substantially larger forces, thus allowing it to slow the microvillus and prolong the time spent in the range of forces that enhance its lifetime. For the VSV8 system, forces in the range of $\sim$10 to 30 pN significantly increase the lifetime of the bond. Thus, two such bonds aligned so that the force is mostly opposed to the direction of microvillus motion can halt the motion of the microvillus for a sustained period of time. This allows other TCR-pMHC complexes to accumulate and further stabilize the microvillus. As a consequence, the total time that TCRs

stay engaged increases substantially when the microvillus is immobilized, which can promote intracellular signaling, starting with phosphorylation of ITAM domains on the cytoplasmic domain of the TCR complex (29, 126). Because the stimulatory pMHCs are randomly distributed, the time at which the microvillus stops occurs at random. Microvilli are immobilized more quickly on average at higher concentrations of stimulatory pMHC because of the increased likelihood to encounter multiple stimulatory pMHCs at once.

Our results reveal that the physical stabilization of microvilli could amplify differences in the response to self and foreign pMHCs, thus enhancing the ability of a T cell to identify antigens. Other potential advantages that microvilli confer to T cells are that they enable the scanning of large portions of the APC surface, facilitate contact between TCRs and pMHCs, and may provide protrusive and retractive forces (22, 105). Other molecules such as coreceptors, transmembrane phosphatases, and adhesion molecules are also important players in T-cell activation. This is a rich area for future study, and combining experiments and theory should help to untangle the complex mechano-chemical events leading to antigen discrimination by T cells. Additionally, it is interesting to speculate about active search and force generation as a tool in designing synthetic systems for detecting ligands of interest.

Chapter 5

Dynamics of EphA2 receptor clustering

Summary: Here, we develop a computational model to investigate the dynamics of EphA2 receptor clustering. This work stemmed from collaboration with the Barrera laboratory in the BCMB department at the University of Tennessee, Knoxville.

5.1 Receptor clustering

Receptor-mediated interactions at cell-cell interfaces are abundant and play a pivotal role in many downstream signaling processes, ultimately ushering a response from the cell. In this dissertation, we computationally model receptor-clustering processes in the contexts of T-cell antigen discrimination and EphA2 receptor oligomerization. As mentioned previously, T cells use their surface receptors to bind to presented ligands on target cell surfaces. Physical properties of the antigen-presenting cell including membrane stiffness, ligand densities, and agonist peptide fraction, are thought to translate into the spatial organization of TCR microclusters (100). TCR clustering shifts the local kinase-phosphatase balance to favor phosphorylation by the exclusion of CD45 phosphatases and increasing the likelihood of TCR-Lck interactions (23, 90). These TCR microclusters then initiate signal transduction eventually leading to T-cell activation. Thus, receptor clustering is expected to play a large role in antigen discrimination and T-cell activation.

We consider an additional biological system where receptor clustering plays a central role in regulating the ultimate cellular response. EphA2 is a transmembrane receptor tyrosine kinase whose interactions with its highest affinity ligand, ephrin-A1, are suspected to play a role in the

progression and formation of cancer malignancy (127, 132, 146). Receptor clustering and the local cluster density have been proposed to regulate signaling mechanisms that could be correlated with overexpression of EphA2 in tumor cells (132, 146). EphA2 receptors reach their fully activated form by first dimerizing and then binding to other existing EphA2 dimers or oligomers. A byproduct of the fully activated EphA2 receptor is strong Eph-ephrin signaling within the cell. This Eph-eprhin signaling impedes cell motility and decreases the expansion potential of EphA2 tumor cells. Therefore, elucidating the formation of receptor clusters could prove useful in strategizing how to target and modulate Eph-overexpressing tumors.

5.2 EphA2 receptor introduction

Eph receptors are the largest subfamily of receptor tyrosine kinases (RTKs) and bind to their ligands, ephrins (7). In general, phosphorylation of RTKs initiate downstream signaling cascades and are central to cell proliferation and tissue organization (10, 85, 113). Eph receptors are sorted into two subclasses, EphA and EphB, which are dependent upon the binding properties to their ligand (101). EphA2 receptor overexpression and activity, accompanied with a low level expression of its ligand ephrin-A1, has appeared in breast, colorectal, gastric, gliboblastoma, lung, and prostate cancer (13, 57, 66, 81, 93, 131, 141, 145). Several previous experimental studies have demonstrated that the tumorigenic activity is linked to high cell motility and elevated levels of Ser-897-phosphorylated EphA2 within the stem cell population (13, 88, 89). Taken together, these results establish that an unliganded EphA2 receptor elicits oncogenic properties.

Ephrin ligands are anchored to the membrane and only activate signaling pathways via direct cell-cell contact. One of the key differences between the two sets of ephrin is that ephrin-A ligands do not contain a cytoplasmic domain. Intriguingly, the Eph-ephrin system displays bi-directional signaling. That is, an intracellular signal can be generated in either the receptor-bearing cell or the ligand-bearing cell after the conformational change of the receptor-ligand pair (30, 102). Eph-ephrin signaling was observed to couple to GTPases, which in turn couple to changes within the actin cytoskeleton and directly impacted the cellular motility (64, 97). Importantly, strong Eph-ephrin signals led to the inhibition of cell motility. This then suggests that Eph-eprhin signaling obstructs the invasive potential / expansion of existing tumors (7, 88, 94). The strength of the

Eph-ephrin signal is dependent upon the full activation of the EphA2 receptor. In order to fully activate, EphA2 first dimerizes, and then subsequently binds to other EphA2 dimers or oligomers to assemble into receptor clusters (46, 58, 121). Therefore, EphA2 receptor clusters are thought to suppress the otherwise tumorigenic activity of the undimerized EphA2 receptor (4, 127).

Recently, groups have proposed the treatment of EphA2-induced tumors by (i) reducing the number of monomeric receptors via stabilized interactions with peptides (4, 127), or (ii) raising an adaptive immune response against EphA2-derived peptides (118). An important, exploitable indicator of aggressive tumors is a highly acidic, local environment. Combining the above therapeutic treatments with this detail, Alves et al. designed a pH-dependent peptide, TYPE7, by altering the sequence of the transmembrane domain of EphA2 (4). At neutral pH, the peptide interacts with cell membranes. However, upon encountering a locally acidic environment, TYPE7 inserts itself into the membrane due to a conformational-induced polarity switch, and subsequent rise in hydrophobicity. TYPE7 is highly soluble and interacts with the surface of lipid membranes at neutral pH, while acidity triggers membrane insertion. In this way, Alves et al. propose to utilize the local acidic environments of tumors to chemotactically locate, and then interact with overexpressed EphA2 receptors.

5.3 Model formulation

The clustering of EphA2 receptors through interactions with ephrin-A1 or by titration of TYPE7 are similar, but differ in levels of self-assembly. Understanding the molecular events responsible for these differences could potentially shed new light on the molecular basis of the EphA2 clustering mechanism. To explore this, we developed a mathematical model describing EphA2 assembly kinetics. This particle-based, stochastic model accounts for the assembly of EphA2 monomers into dimers, and dimers into clusters, as well as the effect of binding of ephrin and TYPE7.

The model parameters include measured diffusion coefficients (4), association rate constants (k_{on}), and dissociation rate constants (k_{off}) for several different binding reactions. The dimerization k_{on} and k_{off} values are constrained by the previously determined ΔG of EphA2 dimerization (67).

Alves et al. used fluorescence correlation spectroscopy (FCS) to determine the EphA2 density at the plasma membrane was 123 monomers per μm^2 (4).

We employed the Gillespie algorithm to generate computer simulation trajectories describing the evolution of the system in space and time (40). In the model, the EphA2 monomer can form two types of dimers: one corresponds to a dimer with low activity (referred to as "inactive dimer"), and the second to the dimer in an alternative active conformation that can oligomerize into clusters ("active dimer") (123) (Fig. E.1). The two dimers are conceptualized to use different dimerization interfaces that likely involve different protein-protein contacts in both soluble domains and the transmembrane helix. NMR data suggests that the inactive dimer would use the interface observed in the NMR structure of the dimeric EphA2 transmembrane helix (17). NMR data did not contain extra resonances that suggested the presence of an alternative dimer conformation (4). As a result, we assumed the inactive dimer was significantly more stable than an active dimer (Fig. E.2). Therefore, the inactive dimers would be found prior to ligand activation. The model assumes that binding of ephrin-A1 induces a conformational change that disfavors the inactive dimer interface, promoting the formation of active dimers through a different interface.

5.4 Parameterization of the model and sensitivity analysis

Given the limited data in literature for the binding and dissociation rates of the system, we conducted an extensive parameter sweep to find kinetic parameters that resulted in a significant variation in the cluster fraction between fully titrated and zero TYPE7 peptide systems (Fig. E.3). In the absence of TYPE7, EphA2 receptors can bind to other particles using either dimerization interface. This would promote low levels of EphA2 receptor clustering due to a considerable fraction of EphA2 receptors bound in the inactive dimer state. Similarly, a system that is concentrated with ephrin-A1 would promote the dimerization of receptors through the active binding interface, prompting the subsequent formation of EphA2 receptor clusters.

After evaluating many kinetic parameter sets, we employed a sensitivity analysis of our chosen parameters and ensured robust responses from the model (Fig. E.4). Lastly, to demonstrate that the system size had no effect on the results, we doubled the system size and compared the cluster

fraction as a function of TYPE7 peptide density, and found no significant deviation between any tested case (Fig. E.5).

Table E1 shows the parameters used for results presented in the chapter. The last column shows the source of the parameter, where PS indicates that the value was derived from a parameter sweep, and subsequently analyzed through sensitivity analysis. The free energies of dimerization at the inactive and active interfaces are $\Delta G_{\mathrm{I}} = -5.45$ and $\Delta G_{\mathrm{A}} = -2.32$ kcal/mol. The free energy associated with the cluster reaction is $\Delta G_{\mathrm{C}} = -9.54$ kcal/mol.

5.5 Time-dependence of EphA2 species fractions

Figure E.6 shows the progression of the system over time starting from EphA2 monomers (blue line). In the absence of ligand, monomers rapidly assembled into dimers, almost exclusively in the inactive conformation. The levels of monomers and dimers rapidly equilibrated, reaching similar levels (Fig. E.6). Cluster levels were low, in agreement with previous observations (127). The vertical dashed line in Fig. E.6 marks the introduction of ephrin-A1. The model proposes that binding of saturating levels of ephrin-A1 causes a conformational switch that disfavors the inactive dimers, completely blocking the inactive interface. We observed that introduction of ephrin-A1 caused a transient increase in the number of monomers and a fast decrease of inactive dimers. A slight increase in the population of active dimers also occurred, constituting a transiently populated intermediate state that nucleated cluster formation. Once a cluster was formed, newly formed active dimers were rapidly added to the cluster, consequently keeping the population of isolated active dimers barely detectable. In this scenario, cluster growth rapidly accelerated after ephrin-A1 addition and eventually started to saturate. Interestingly, saturation of cluster formation occurred 5 minutes after ephrin-A1 addition, similar to the kinetics of phosphorylation of a tyrosine (Y772) on the cytoplasmic tail of EphA2, which results from EphA2 self-assembly (79).

5.6 TYPE7 titration characterization

We considered next the effect of TYPE7 on EphA2 self-assembly. We assumed that TYPE7 could bind to the EphA2 monomer using the inactive interface (blocked upon ephrin-A1 binding),

competing with formation of inactive dimers. When we introduced TYPE7 as a new particle into the system (Fig. E.7), it bound to EphA2 monomers and slowly reduced the number of inactive dimers. The effect of TYPE7 was concentration-dependent (Fig. E.8). When the TYPE7 concentration was less than EphA2, we observed slower and less efficient cluster formation than in the presence of ephrin-A1. Therefore, the mathematical model provides a plausible theoretical framework to explain why TYPE7 induces lower clustering levels than ephrin-A1.

5.7 Discussion

We have developed a mathematical model that provides insights that might explain the observed differences in cluster size. The fundamental assumptions of the model are based on experimental observations. Specifically, crystallographic studies have shown the presence of different protein-protein interfaces in the EphA2 extracellular domain. This suggests that a switch between alternate extracellular domain protein-protein interfaces can trigger a conformational change that leads to cluster formation (46, 121, 122). Additionally, it has been proposed that the transmembrane helix of EphA2 can dimerize using several interfaces (123). The resulting alternative transmembrane dimers would correspond to different (inactive vs. active) functional states. The kinetic model builds on these concepts, and suggests that switching between two alternate dimer conformations can explain the experimental results. The model assumes that ephrin-A1 binding would abrogate the inactive dimer conformation and result in a conformational switch to the alternate active dimer form. This state would be unstable, and act as a transient intermediate that rapidly assembles into the more stable cluster (Figs.E.2 and E.6). It has been previously hypothesized that EphA2 clusters use a seeding mechanism (56). Our model supports that the active dimer might be the species that seeds EphA2 cluster formation.

The model also suggests that we can reconcile the observation that TYPE7 is less efficient than ephrin in inducing clustering, while using a similar activation mechanism (4). The differences might be kinetic in nature, as TYPE7 binding would cause slower oligomerization.

Chapter 6

Future Directions

In this dissertation, we employed computational modeling to a number of biophysical receptor-mediated systems. We have shown that computational modeling can provide mechanistic insight into the underlying biophysics that would otherwise be difficult to attain using *in vivo* and *in vitro* methodologies. It is interesting to consider future directions for both *de novo* projects and direct extensions of these computational models.

6.1 Evaluating the timescale necessary to distinguish an infected cell

One compelling question posed in immunology is how quickly a T cell can detect, interact, and distinguish an infected cell. Given a chemical species gradient, it would be interesting to model how quickly a T cell moves across a system before encountering an infected cell. Different types of motion, such as random or chemotactic, could be considered as viable options for T-cell diffusion. Upon reaching the target cell, the T cell would be able to interact with the antigen-presenting surface. The surface of the target cell could be loaded with varying degrees of stimulatory pMHC. Implementing receptor-ligand binding kinetics with coupled ODEs to describe the intracellular calcium flux of the T cell could provide as a proxy to measure T-cell activation. Although this is admittedly a very ambitious project, the results and natural comparisons to experimental work in the field would be remarkable.

6.2 Two-dimensional EphA2 receptor clustering model

A natural extension of the EphA2 receptor model is to consider a two-dimensional system. A hexagonal lattice approach would increase the number of possible binding angles and promote the formation of interesting cluster organization. Salaita et al. has observed micron-sized clusters that contain hundreds of EphA2 receptors (118). Thus, the system size would need to increase to accommodate comparisons to experimentally observed phenomena.

The mapping of kinetic parameters for chemical species in the EphA2 receptor system could provide a basis for future experimental studies and predictions. The diffusion of clusters can be readily implemented into the model, and would offer an interesting analysis of the effective diffusion coefficient of EphA2 receptor clusters as a function of cluster size. In addition, the inclusion of an EphA2 receptor degradation term may strengthen the model's representation of the biophysical system. Lastly, an estimate for the timescale needed to reach an average EphA2 receptor cluster size could prove useful to Eph-ephrin signaling applications.

6.3 Imposing shear flows on the T-cell / antigen-presenting cell interface

The direction and magnitude of forces has been shown to impact TCR triggering (31). A simple extension of the TCR clustering model would allow for shear forces at the cell-cell interface. To allow for shear forces, the T-cell receptors would be permitted to bind to pMHC molecules on the target cell surface if they are within a given binding radius. This in contrast to the model described in Ch. 3, which only permits binding if the TCR is overlaid on the lattice site of the pMHC molecule.

Using the same formalism, we could model the T cell crawling across a target cell surface. The number of binding events, average bond lifetimes, and TCR clusters could be analyzed as a function of T-cell velocity and pMHC density. The T-cell velocity can be modeled as either a constant or have a force-dependent description similar to the formulation in Ch. 4. This computational work could provide as a basis for future experimental micropillar assay studies,

or used in conjunction with experiments to elucidate the role of catch bonds in T-cell spreading / immunological synapse formation.

A longer-term focus of the shear flow project could be to model the formation of T-cell microvilli-derived particles (TMPs). TMPs have been proposed to maintain communication with a previously-visited antigen-presenting cell (68). What is the required magnitude of shear forces that cause TMPs to form on the surface of target cells as the T-cell continues to crawl across the conjugate surface? How do receptor-ligand binding kinetics couple to this cellular adhesion process? In addition to the framework described above, this model would need to consider membrane budding and fusion.

Bibliography

[1] Aleksic, M., Dushek, O., Zhang, H., Shenderov, E., Chen, J.-L., Cerundolo, V., Coombs, D., and van der Merwe, P. A. (2010). Dependence of T cell antigen recognition on T cell receptor-peptide MHC confinement time. *Immunity*, 32(2):163–174. 45

[2] Allard, J. F., Dushek, O., Coombs, D., and van der Merwe, P. A. (2012). Mechanical modulation of receptor-ligand interactions at cell-cell interfaces. *Biophys. J.*, 102(6):1265–1273. 33, 34, 35, 36, 50, 110

[3] Allen, J. R., Ross, S. T., and Davidson, M. W. (2013). Single molecule localization microscopy for superresolution. *J. Opt.*, 15(9):094001. 21

[4] Alves, D. S., Westerfield, J. M., Shi, X., Nguyen, V. P., Stefanski, K. M., Booth, K. R., Kim, S., Morrell-Falvey, J., Wang, B.-C., Abel, S. M., Smith, A. W., and Barrera, F. N. (2018). A novel pH-dependent membrane peptide that binds to EphA2 and inhibits cell migration. *eLife*, 7:e36645. 66, 67, 69, 132

[5] Artyomov, M. N., Lis, M., Devadas, S., Davis, M. M., and Chakraborty, A. K. (2010). CD4 and CD8 binding to MHC molecules primarily acts to enhance Lck delivery. *Proc. Natl. Acad. Sci.*, 107(39):16916–16921. 4

[6] Asano, M., Toda, M., Sakaguchi, N., and Sakaguchi, S. (1996). Autoimmune disease as a consequence of developmental abnormality of a T cell subpopulation. *J. Exp. Med.*, 184(2):387–396. 2

[7] Barquilla, A. and Pasquale, E. B. (2015). Eph receptors and ephrins: Therapeutic opportunities. *Annu. Rev. Pharmacol. Toxicol.*, 55:465–487. 65

[8] Bashour, K. T., Gondarenko, A., Chen, H., Shen, K., Liu, X., Huse, M., Hone, J. C., and Kam, L. C. (2014). CD28 and CD3 have complementary roles in T-cell traction forces. *Proc. Natl. Acad. Sci. U.S.A.*, 111(6):2241–2246. 32

[9] Basu, R., Whitlock, B. M., Husson, J., Floc'h, A. L., Jin, W., Oyler-Yaniv, A., Dotiwala, F., Giannone, G., Hivroz, C., Biais, N., Lieberman, J., Kam, L. C., and Huse, M. (2016). Cytotoxic T cells use mechanical force to potentiate target cell killing. *Cell*, 165(1):100–110. 12

[10] Batlle, E. and Wilkinson, D. G. (2012). Molecular mechanisms of cell segregation and boundary formation in development and tumorigenesis. *Cold Spring Harb. Perspect. Biol.*, 4(1):a008227. 65

[11] Bell, G. I. (1978). Models for the specific adhesion of cells to cells. *Science*, 200(4342):618–627. 31, 32, 46, 48, 56

[12] Betzig, E., Patterson, G. H., Sougrat, R., Lindwasser, O. W., Olenych, S., Bonifacino, J. S., Davidson, M. W., Lippincott-Schwartz, J., and Hess, H. F. (2006). Imaging intracellular fluorescent proteins at nanometer resolution. *Science*, 313(5793):1642–1645. 21

[13] Binda, E., Visioli, A., Giani, F., Lamorte, G., Copetti, M., Pitter, K. L., Huse, J. T., Cajola, L., Zanetti, N., DiMeco, F., De Filippis, L., Mangolia, A., Giulio, M., Anile, C., De Bonis, P., Reynold, B. A., Pasquale, E. B., and Vescovi, A. L. (2012). The EphA2 receptor drives self-renewal and tumorigenicity in stem-like tumor-propagating cells from human glioblastomas. *Cancer Cell*, 22(6):765–780. 65

[14] Birnbaum, M. E., Berry, R., Hsiao, Y.-S., Chen, Z., Shingu-Vazquez, M. A., Yu, X., Waghray, D., Fischer, S., McCluskey, J., Rossjohn, J., Thomas, W., and Garcia, K. C. (2014). Molecular architecture of the $\alpha\beta$ T cell receptor–CD3 complex. *Proc. Natl. Acad. Sci. U.S.A.*, 111(49):17576–17581. xvii, 35, 54, 110, 111

[15] Blackman, M., Kappler, J. W., and Marrack, P. (1990). The role of the T cell receptor in positive and negative selection of developing T cells. *Science*, 248(4961):1335–1341. 2

[16] Boal, D. (2012). *Mechanics of the Cell*. Cambridge University Press. 35

[17] Bocharov, E. V., Mayzel, M. L., Volynsky, P. E., Mineev, K. S., Tkach, E. N., Ermolyuk, Y. S., Schulga, A. A., Efremov, R. G., and Arseniev, A. S. (2010). Left-handed dimer of EphA2 transmembrane domain: Helix packing diversity among receptor tyrosine kinases. *Biophys. J.*, 98(5):881–889. 67

[18] Brameshuber, M., Kellner, F., Rossboth, B. K., Ta, H., Alge, K., Sevcsik, E., Göhring, J., Axmann, M., Baumgart, F., Gascoigne, N. R. J., Davis, S. J., Stockinger, H., Schütz, G. J.,

and Huppa, J. B. (2018). Monomeric TCRs drive T cell antigen recognition. *Nat. Immunol.*, 19(5):487–496. 10, 110

[19] Buckley, C. D., Tan, J., Anderson, K. L., Hanein, D., Volkmann, N., Weis, W. I., Nelson, W. J., and Dunn, A. R. (2014). The minimal cadherin-catenin complex binds to actin filaments under force. *Science*, 346(6209). 31

[20] Burkhardt, J. K., Carrizosa, E., and Shaffer, M. H. (2008). The actin cytoskeleton in T cell activation. *Annu. Rev. Immunol.*, 26:233–259. 61

[21] Burroughs, N. J., Lazic, Z., and Merwe, P. A. v. (2006). Ligand detection and discrimination by spatial relocalization: A kinase-phosphatase segregation model of TCR activation. *Biophys. J.*, 91(5):1619–1629. 46

[22] Cai, E., Marchuk, K., Beemiller, P., Beppler, C., Rubashkin, M. G., Weaver, V. M., Gerard, A., Liu, T.-L., Chen, B.-C., Betzig, E., Bartumeus, F., and Krummel, M. F. (2017). Visualizing dynamic microvillar search and stabilization during ligand detection by T cells. *Science*, 356(6338):eaal3118. 17, 20, 53, 61, 62, 63

[23] Carbone, C. B., Kern, N., Fernandes, R. A., Hui, E., Su, X., Garcia, K. C., and Vale, R. D. (2017). *In vitro* reconstitution of T cell receptor-mediated segregation of the CD45 phosphatase. *Proc. Natl. Acad. Sci.*, 114(44):E9338–E9345. 14, 15, 20, 64, 110

[24] Casal, A., Sumen, C., Reddy, T. E., Alber, M. S., and Lee, P. P. (2005). Agent-based modeling of the context dependency in T cell recognition. *J. Theor. Biol.*, 236(4):376–391. 55

[25] Chang, V. T., Fernandes, R. A., Ganzinger, K. A., Lee, S. F., Siebold, C., McColl, J., Jönsson, P., Palayret, M., Harlos, K., Coles, C. H., Jones, E. Y., Lui, Y., Huang, E., Gilbert, R. J. C., Klenerman, D., Aricescu, A. R., and Davis, S. J. (2016). Initiation of T cell signaling by CD45 segregation at 'close contacts'. *Nat. Immunol.*, 17:574–582. 33

[26] Chávez-Galán, L., Arenas-Del Angel, M., Zenteno, E., Chávez, R., and Lascurain, R. (2009). Cell death mechanisms induced by cytotoxic lymphocytes. *Cell. Mol. Immunol.*, 6(1):15. 1

[27] Chen, B.-C., Legant, W. R., Wang, K., Shao, L., Milkie, D. E., Davidson, M. W., Janetopoulos, C., Wu, X. S., Hammer, J. A., Liu, Z., English, B. P., Mimori-Kiyosue, Y., Romero, D. P., Ritter, A. T., Lippincott-Schwartz, J., Fritz-Laylin, L., Mullins, R. D., Mitchell, D. M., Bembenek, J. N., Reymann, A.-C., Böhme, R., Grill, S. W., Wang, J. T., Seydoux, G., Tulu, U. S., Kiehart, D. P., and Betzig, E. (2014). Lattice light-sheet microscopy: Imaging molecules to embryos at high spatiotemporal resolution. *Science*, 346(6208). 20

[28] Cole, D. K. and Gao, G. F. (2004). CD8: Adhesion molecule, co-receptor and immunomodulator. *Cell. Mol. Immunol.*, 1(2):81–88. 1

[29] Courtney, A. H., Lo, W.-L., and Weiss, A. (2018). TCR signaling: Mechanisms of initiation and propagation. *Trends Biochem. Sci.*, 43(2):108–123. 63

[30] Daar, I. O. (2012). Non-SH2/PDZ reverse signaling by ephrins. *Semin. Cell Dev. Biol.*, 23(1):65–74. 65

[31] Das, D. K., Feng, Y., Mallis, R. J., Li, X., Keskin, D. B., Hussey, R. E., Brady, S. K., Wang, J. H., Wagner, G., Reinherz, E. L., and Lang, M. J. (2015). Force-dependent transition in the T-cell receptor β-subunit allosterically regulates peptide discrimination and pMHC bond lifetime. *Proc. Natl. Acad. Sci. U.S.A.*, 112(5):1517–1522. 7, 8, 15, 19, 32, 53, 61, 62, 71

[32] Davis, S. J. and van der Merwe, P. A. (2006). The kinetic-segregation model: TCR triggering and beyond. *Nat. Immunol.*, 7(8):803–809. 15, 33

[33] Deeg, J., Axmann, M., Matic, J., Liapis, A., Depoil, D., Afrose, J., Curado, S., Dustin, M. L., and Spatz, J. P. (2013). T cell activation is determined by the number of presented antigens. *Nano Lett.*, 13(11). 47

[34] Depoil, D. and Dustin, M. L. (2014). Force and affinity in ligand discrimination by the TCR. *Trends Immunol.*, 35(12):597–603. 32, 52, 53

[35] Dobrowsky, T. M., Daniels, B. R., Siliciano, R. F., Sun, S. X., and Wirtz, D. (2010). Organization of cellular receptors into a nanoscale junction during HIV-1 adhesion. *PLoS Comput. Biol.*, 6(7):1–14. 34

[36] Favier, B., Burroughs, N. J., Wedderburn, L., and Valitutti, S. (2001). TCR dynamics on the surface of living T cells. *Int. Immunol.*, 13(12):1525–1532. 115

[37] Feng, Y., Brazin, K. N., Kobayashi, E., Mallis, R. J., Reinherz, E. L., and Lang, M. J. (2017). Mechanosensing drives acuity of $\alpha\beta$ T-cell recognition. *Proc. Natl. Acad. Sci. U.S.A.*, 114(39):E8204–E8213. xviii, 7, 15, 19, 46, 53, 56, 117

[38] Feng, Y., Reinherz, E. L., and Lang, M. J. (2018). $\alpha\beta$ T cell receptor mechanosensing forces out serial engagement. *Trends Immunol.*, 39(8):569–609. 19, 53

[39] Fisher, P. J., Bulur, P. A., Vuk-Pavlovic, S., Prendergast, F. G., and Dietz, A. B. (2008). Dendritic cell microvilli: A novel membrane structure associated with the multifocal synapse and T-cell clustering. *Blood*, 112(13):5037–5045. 54

[40] Gillespie, D. T., Hellander, A., and Petzold, L. R. (2013). Perspective: Stochastic algorithms for chemical kinetics. *J. Chem. Phys.*, 138(17):05B201_1. 67

[41] Golubovskaya, V. and Wu, L. (2016). Different subsets of T cells, memory, effector functions, and CAR-T immunotherapy. *Cancers*, 8(3):36. 1

[42] Grakoui, A., Bromley, S. K., Sumen, C., Davis, M. M., Shaw, A. S., Allen, P. M., and Dustin, M. L. (1999). The immunological synapse: A molecular machine controlling T cell activation. *Science*, 285(5425):221–227. 55

[43] Grima, R. and Newman, T. J. (2004). Accurate discretization of advection-diffusion equations. *Phys. Rev. E*, 70(3):036703. 49

[44] Gutiérrez-Vázquez, C., Villarroya-Beltri, C., Mittelbrunn, M., and Sánchez-Madrid, F. (2013). Transfer of extracellular vesicles during immune cell-cell interactions. *Immunol. Rev.*, 251(1):125–142. 17

[45] Harder, T. and Sangani, D. (2009). Plasma membrane rafts engaged in T cell signalling: New developments in an old concept. *Cell Comm. Signal.*, 7(1):21. 15

[46] Himanen, J. P., Yermekbayeva, L., Janes, P. W., Walker, J. R., Xu, K., Atapattu, L., Rajashankar, K. R., Mensinga, A., Lackmann, M., Nikolov, D. B., and Dhe-Paganon,

S. (2010). Architecture of Eph receptor clusters architecture of Eph receptor clusters. *Proc. Natl. Acad. Sci. U.S.A.*, 107(24):10860–10865. 66, 69

[47] Hindmarsh, A. C., Gresho, P. M., and Griffiths, D. F. (1984). The stability of explicit Euler time-integration for certain finite difference approximations of the multi-dimensional advection-diffusion equation. *Int. J. Numer. Meth. Fluids*, 4(9):853–897. 35, 106

[48] Hivroz, C. and Saitakis, M. (2016). Biophysical aspects of T lymphocyte activation at the immune synapse. *Front. Immunol.*, 7:46. 31, 52, 53, 62

[49] Hogquist, K. A., Jameson, S. C., Heath, W. R., Howard, J. L., Bevan, M. J., and Carbone, F. R. (1994). T cell receptor antagonist peptides induce positive selection. *Cell*, 76(1):17–27. 2, 52

[50] Hong, J., Ge, C., Jothikumar, P., Liu, B., Bai, K., Li, K., Rittase, W., Shinzawa, M., Zhang, Y., Palin, A., Love, P., Yu, X., Salaita, K., Evavold, B. D., Singer, A., and Zhu, C. (2018). A TCR mechanotransduction signaling loop induces negative selection in the thymus. *Nat. Immunol.*, 19(12):1379. 5, 53

[51] Hong, J., Persaud, S. P., Horvath, S., Allen, P. M., Evavold, B. D., and Zhu, C. (2015). Force-regulated *in situ* TCR-peptide-bound MHC class II kinetics determine functions of CD4+ T cells. *J. Immunol.*, 195(8):3557–3564. 32, 53

[52] Hu, K. H. and Butte, M. J. (2016). T cell activation requires force generation. *J. Cell Biol.*, 213(5):535–542. 22, 32, 45

[53] Huang, J., Brameshuber, M., Zeng, X., Xie, J., Li, Q., Chien, Y., Valitutti, S., and Davis, M. M. (2013). A single peptide-major histocompatibility complex ligand triggers digital cytokine secretion in CD4+ T cells. *Immunity*, 39(5):846–857. 32, 52

[54] Huang, J., Zarnitsyna, V. I., Liu, B., Edwards, L. J., Jiang, N., Evavold, B. D., and Zhu, C. (2010). The kinetics of two-dimensional TCR and pMHC interactions determine T-cell responsiveness. *Nature*, 464(7290):932–936. 19, 32, 46, 53, 56, 110, 115

[55] Hui, K. L., Balagopalan, L., Samelson, L. E., and Upadhyaya, A. (2015). Cytoskeletal forces during signaling activation in Jurkat T-cells. *Mol. Biol. Cell*, 26(4):685–695. 32

[56] Huppa, J. B., Axmann, M., Mörtelmaier, M. A., Lillemeier, B. F., Newell, E. W., Brameshuber, M., Klein, L. O., Schütz, G. J., and Davis, M. M. (2010). TCR–peptide–MHC interactions *in situ* show accelerated kinetics and increased affinity. *Nature*, 463(7283):963–967. 32

[57] Ishikawa, M., Miyahara, R., Sonobe, M., Horiuchi, M., Mennju, T., Nakayama, E., Kobayashi, M., Kikuchi, R., Kitamura, J., Imamura, N., Huang, C.-L., and Date, H. (2012). Higher expression of EphA2 and ephrin-A1 is related to favorable clinicopathological features in pathological stage I non-small cell lung carcinoma. *Lung Cancer*, 76(3):431–438. 65

[58] Janes, P. W., Nievergall, E., and Lackmann, M. (2012). Concepts and consequences of Eph receptor clustering. *Semin. Cell Dev. Biol.*, 23(1):43–50. 66

[59] Jenkins, E., Santos, A. M., O'Brien-Ball, C., Felce, J. H., Wilcock, M. J., Hatherley, D., Dustin, M. L., Davis, S. J., Eggeling, C., and Sezgin, E. (2019). Reconstitution of immune cell interactions in free-standing membranes. *J. Cell Sci.*, 132(4). 20

[60] Joly, E. and Hudrisier, D. (2003). What is trogocytosis and what is its purpose? *Nat. Immunol.*, 4:815 EP. 17

[61] Jones, E. (1997). MHC class I and class II structures. *Curr. Opin. Immunol.*, 9(1):75–79. 3

[62] Judokusumo, E., Tabdanov, E., Kumari, S., Dustin, M. L., and Kam, L. C. (2012). Mechanosensing in T lymphocyte activation. *Biophys. J.*, 102(2):L5–L7. 32

[63] Jung, Y., Riven, I., Feigelson, S. W., Kartvelishvily, E., Tohya, K., Miyasaka, M., Alon, R., and Haran, G. (2016). Three-dimensional localization of T-cell receptors in relation to microvilli using a combination of superresolution microscopies. *Proc. Natl. Acad. Sci. U.S.A.*, 113(40):E5916–E5924. 53, 54, 55, 115

[64] Kania, A. and Klein, R. (2016). Mechanisms of ephrin-Eph signalling in development, physiology and disease. *Nat. Rev. Mol. Cell Biol.*, 17(4):240. 65

[65] Kappler, J. W., Roehm, N., and Marrack, P. (1987). T cell tolerance by clonal elimination in the thymus. *Cell*, 49(2):273–280. 2

[66] Kataoka, H., Igarashi, H., Kanamori, M., Ihara, M., Wang, J.-D., Wang, Y.-J., Li, Z.-Y., Shimamura, T., Kobayashi, T., Maruyama, K., Nakamura, T., Arai, H., Kajimura, M., Hanai, H., Tanaka, M., and Sugimura, H. (2004). Correlation of EphA2 overexpression with high microvessel count in human primary colorectal cancer. *Cancer Sci.*, 95(2):136–141. 65

[67] Killian, J. A. and Nyholm, T. K. (2006). Peptides in lipid bilayers: The power of simple models. *Curr. Opin. Struct. Biol.*, 16(4):473–479. 66, 132

[68] Kim, H.-R., Mun, Y., Lee, K.-S., Park, Y.-J., Park, J.-S., Park, J.-H., Jeon, B.-N., Kim, C.-H., Jun, Y., Hyun, Y.-M., Kim, M., Lee, S.-M., Park, C.-S., Im, S.-H., and Jun, C.-D. (2018). T cell microvilli constitute immunological synaptosomes that carry messages to antigen-presenting cells. *Nat. Commun.*, 9(1):3630. 18, 53, 72

[69] Kim, S. T., Takeuchi, K., Sun, Z.-Y. J., Touma, M., Castro, C. E., Fahmy, A., Lang, M. J., Wagner, G., and Reinherz, E. L. (2009). The $\alpha\beta$ T cell receptor is an anisotropic mechanosensor. *J. Biol. Chem.*, 284:31028–31037. 4, 32

[70] Kim, S. T., Touma, M., Takeuchi, K., Sun, Z.-Y. J., Dave, V. P., Kappes, D. J., Wagner, G., and Reinherz, E. L. (2010). Distinctive CD3 heterodimeric ectodomain topologies maximize antigen-triggered activation of $\alpha\beta$ T cell receptors. *J. Immunol.*, 185(5):2951–2959. 15

[71] Kleman, M. and Laverntovich, O. D. (2007). *Soft matter physics: An introduction*. Spring Science & Business Media. 25

[72] Krobath, H., Schütz, G., Lipowsky, R., and Weikl, T. (2007). Lateral diffusion of receptor-ligand bonds in membrane adhesion zones: Effect of thermal membrane roughness. *EPL*, 78(3):38003. 35

[73] Kuhns, M. S., Davis, M. M., and Garcia, K. C. (2006). Deconstructing the form and function of the TCR/CD3 complex. *Immunity*, 24(2):133 – 139. 3

[74] Lee, H. J., Peterson, E. L., Phillips, R., Klug, W. S., and Wiggins, P. A. (2008). Membrane shape as a reporter for applied forces. *Proc. Natl. Acad. Sci. U.S.A.*, 105(49):19253–19257. 36

[75] Lever, M., Maini, P. K., van der Merwe, P. A., and Dushek, O. (2014). Phenotypic models of T cell activation. *Nat. Rev. Immunol.*, 14(9):619–629. 32

[76] Liu, B., Chen, W., Evavold, B. D., and Zhu, C. (2014). Accumulation of dynamic catch bonds between TCR and agonist peptide-MHC triggers T cell signaling. *Cell*, 157(2):357–368. xv, xviii, 5, 19, 32, 42, 46, 53, 56, 61, 62, 96, 106, 117

[77] Liu, Y., Blanchfield, L., Ma, V. P.-Y., Andargachew, R., Galior, K., Liu, Z., Evavold, B., and Salaita, K. (2016). DNA-based nanoparticle tension sensors reveal that T-cell receptors transmit defined pN forces to their antigens for enhanced fidelity. *Proc. Natl. Acad. Sci. U.S.A.*, 113(20):5610–5615. 9, 20, 32, 61

[78] Liu, Y., Yehl, K., Narui, Y., and Salaita, K. (2013). Tension sensing nanoparticles for mechano-imaging at the living/nonliving interface. *J. Am. Chem. Soc.*, 135(14):5320–5323. 21

[79] Locard-Paulet, M., Lim, L., Veluscek, G., McMahon, K., Sinclair, J., Van Weverwijk, A., Worboys, J. D., Yuan, Y., Isacke, C. M., and Jørgensen, C. (2016). Phosphoproteomic analysis of interacting tumor and endothelial cells identifies regulatory mechanisms of transendothelial migration. *Sci. Signal*, 9(414):ra15–ra15. 68

[80] Luo, C., Wang, K., Liu, D., Li, Y., and Zhao, Q. (2008). The functional roles of lipid rafts in T cell activation, immune diseases and HIV infection and prevention. *Cell. Mol. Immunol.*, 5:1–7. 15

[81] Macrae, M., Neve, R., Rodriguez-Viciana, P., Haqq, C., Yeh, J., Chen, C., Gray, J. W., and McCormick, F. (2005). A conditional feedback loop regulates Ras activity through EphA2. *Cancer Cell*, 8(2):111–118. 65

[82] Majstoravich, S., Zhang, J., Nicholson-Dykstra, S., Linder, S., Friedrich, W., Siminovitch, K. A., and Higgs, H. N. (2004). Lymphocyte microvilli are dynamic, actin-dependent structures

that do not require Wiskott-Aldrich syndrome protein (WASp) for their morphology. *Blood*, 104(5):1396–1403. 54, 61

[83] Manibog, K., Li, H., Rakshit, S., and Sivasankar, S. (2014). Resolving the molecular mechanism of cadherin catch bond formation. *Nat. Commun.*, 5:3941. 31

[84] Marshall, B. T., Long, M., Piper, J. W., Yago, T., McEver, R. P., and Zhu, C. (2003). Direct observation of catch bonds involving cell-adhesion molecules. *Nature*, 423(6936):190–193. 31

[85] McClelland, A. C., Hruska, M., Coenen, A. J., Henkemeyer, M., and Dalva, M. B. (2010). Trans-synaptic EphB2–ephrin–B3 interaction regulates excitatory synapse density by inhibition of postsynaptic MAPK signaling. *Proc. Natl. Acad. Sci.*, 107(19):8830–8835. 65

[86] Méléard, P., Gerbeaud, C., Pott, T., Fernandez-Puente, L., Bivas, I., Mitov, M., Dufourcq, J., and Bothorel, P. (1997). Bending elasticities of model membranes: Influences of temperature and sterol content. *Biophys. J.*, 72(6):2616–2629. 35

[87] Merkel, R., Nassoy, P., Leung, A., Ritchie, K., and Evans, E. (1999). Energy landscapes of receptor–ligand bonds explored with dynamic force spectroscopy. *Nature*, 397:50–53. 19

[88] Miao, H., Gale, N. W., Guo, H., Qian, J., Petty, A., Kaspar, J., Murphy, A. J., Valenzuela, D. M., Yancopoulos, G., Hambardzumyan, D., Lathia, J. D., Rich, J. N., Lee, J., and Wang, B. (2015). EphA2 promotes infiltrative invasion of glioma stem cells in vivo through cross-talk with Akt and regulates stem cell properties. *Oncogene*, 34(5):558. 65

[89] Miao, H., Li, D.-Q., Mukherjee, A., Guo, H., Petty, A., Cutter, J., Basilion, J. P., Sedor, J., Wu, J., Danielpour, D., Sloan, A. E., Cohen, M. L., and Wang, B. (2009). EphA2 mediates ligand-dependent inhibition and ligand-independent promotion of cell migration and invasion via a reciprocal regulatory loop with Akt. *Cancer Cell*, 16(1):9–20. 65

[90] Mugler, A., Bailey, A. G., Takahashi, K., and Rein ten Wolde, P. (2012). Membrane clustering and the role of rebinding in biochemical signaling. *Biophys. J.*, 102(5):1069–1078. 64

[91] Munir Alam, S., Travers, P. J., Wung, J. L., Nasholds, W., Redpath, S., Jameson, S. C., and Gascoigne, N. (1996). T-cell-receptor affinity and thymocyte positive selection. *Nature*, 381:616–620. 2

[92] Murphy, K., Travers, P., and Walport, M. (2008). *Janeway's Immunobiology*. Garland Science, 7 edition. 2

[93] Nakamura, R., Kataoka, H., Sato, N., Kanamori, M., Ihara, M., Igarashi, H., Ravshanov, S., Wang, Y.-J., Li, Z.-Y., Shimamura, T., Kobayashi, T., Konno, H., Shinmura, K., Tanaka, M., and Sugimura, H. (2005). EPHA2/EFNA1 expression in human gastric cancer. *Cancer Sci.*, 96(1):42–47. 65

[94] Nasreen, N., Mohammed, K. A., Lai, Y., and Antony, V. B. (2007). Receptor EphA2 activation with ephrin-A1 suppresses growth of malignant mesothelioma (MM). *Cancer Lett.*, 258(2):215–222. 65

[95] Nelson, D., Piran, T., and Weinberg, S. (2004). *Statistical mechanics of membranes and surfaces*. World Scientific. 34

[96] Nilsson, L. M., Thomas, W. E., Trintchina, E., Vogel, V., and Sokurenko, E. V. (2006). Catch bond-mediated adhesion without a shear threshold: Trimannose versus monomannose interactions with the FimH adhesion of Escherichia coli. *J. Biol. Chem.*, 281(24):16656–16663. 31

[97] Noren, N. K. and Pasquale, E. B. (2004). Eph receptor–ephrin bidirectional signals that target Ras and Rho proteins. *Cell. Signal.*, 16(6):655–666. 65

[98] O'Connor, R. S., Hao, X., Shen, K., Bashour, K., Akimova, T., Hancock, W. W., Kam, L. C., and Milone, M. C. (2012). Substrate rigidity regulates human T cell activation and proliferation. *J. Immunol.*, 189(3):1330. 22

[99] O'Donoghue, G. P., Pielak, R. M., Smoligovets, A. A., Lin, J. J., and Groves, J. T. (2013). Direct single molecule measurement of TCR triggering by agonist pMHC in living primary T cells. *eLife*, 2:e00778. 45, 55

[100] Pageon, S. V., Tabarin, T., Yamamoto, Y., Yuangqing, M., Nicovich, P. R., Bridgeman, J. S., Cohnen, A., Benzing, C., Gao, Y., Crowther, M. D., Tungatt, K., Dolton, G., Sewell, A. K., Price, D. A., Acuto, O., Parton, R. G., Gooding, J. J., Rossy, J., Rossjohn, J., and

Gaus, K. (2016). Functional role of T-cell receptor nanoclusters in signal initiation and antigen discrimination. *Proc. Natl. Acad. Sci. U.S.A.*, 113(37):E5454–E5463. 13, 14, 21, 32, 46, 51, 52, 64

[101] Pasquale, E. B. (1997). The Eph family of receptors. *Curr. Opin. Cell Biol.*, 9(5):608–615. 65

[102] Pasquale, E. B. (2010). Eph receptors and ephrins in cancer: Bidirectional signalling and beyond. *Nat. Rev. Cancer*, 10(3):165. 65

[103] Paz, P. E., Wang, S., Clarke, H., Lu, X., Stokoe, D., and Abo, A. (2001). Mapping the Zap-70 phosphorylation sites on LAT (linker for activation of T cells) required for recruitment and activation of signalling proteins in T cells. *Biochem. J.*, 356(2):461–471. 4

[104] Pereverzev, Y. V., Prezhdo, O. V., Forero, M., Sokurenko, E. V., and Thomas, W. E. (2005). The two-pathway model for the catch-slip transition in biological adhesion. *Biophys. J.*, 89(3):1446–1454. 33, 48, 56

[105] Pettmann, J., Santos, A. M., Dushek, O., and Davis, S. J. (2018). Membrane ultrastructure and T cell activation. *Front. Immunol.*, 9:2152. 63

[106] Pielak, R. M., O'Donoghue, G. P., Lin, J. J., Alfieri, K. N., Fay, N. C., Low-Nam, S. T., and Groves, J. T. (2017). Early T cell receptor signals globally modulate ligand:receptor affinities during antigen discrimination. *Proc. Natl. Acad. Sci.*, 114(46):12190–12195. 11, 46

[107] Pullen III, R. H. and Abel, S. M. (2017). Catch bonds at T cell interfaces: Impact of surface reorganization and membrane fluctuations. *Biophys. J.*, 113(1):120–131. 31, 47, 50, 53, 110, 115

[108] Qi, S., Groves, J. T., and Chakraborty, A. K. (2001). Synaptic pattern formation during cellular recognition. *Proc. Natl. Acad. Sci. U.S.A.*, 98(12):6548–6553. 33, 34

[109] Razvag, Y., Neve-Oz, Y., Sajman, J., Reches, M., and Sherman, E. (2018). Nanoscale kinetic segregation of TCR and CD45 in engaged microvilli facilitates early T cell activation. *Nat. Commun.*, 9(1):732. 53, 54

[110] Reiser, J.-B., Darnault, C., Grégoire, C., Mosser, T., Mazza, G., Kearney, A., van der Merwe, P. A., Fontecilla-Camps, J. C., Housset, D., and Malissen, B. (2003). CDR3 loop flexibility contributes to the degeneracy of TCR recognition. *Nat. Immunol.*, 4:241–247. 3

[111] Robbins, P. F., Li, Y. F., El-Gamil, M., Zhao, Y., Wargo, J. A., Zheng, Z., Xu, H., Morgan, R. A., Feldman, S. A., Johnson, L. A., Bennet, A. D., Dunn, S. M., Mahon, T. M., Jakobsen, B. K., and Rosenberg, S. A. (2008). Single and dual amino acid substitutions in TCR CDRs can enhance antigen-specific T cell functions. *J. Immunol.*, 180(9):6116–6131. 52

[112] Robert, P., Aleksic, M., Dushek, O., Cerundolo, V., Bongrand, P., and van der Merwe, P. A. (2012). Kinetics and mechanics of two-dimensional interactions between T cell receptors and different activating ligands. *Biophys. J.*, 102(2):248–257. 32

[113] Robinson, D. R., Wu, Y.-M., and Lin, S.-F. (2000). The protein tyrosine kinase family of the human genome. *Oncogene*, 19(49):5548. 65

[114] Rossboth, B., Arnold, A. M., Ta, H., Platzer, R., Kellner, F., Huppa, J. B., Brameshuber, M., Baumgart, F., and Schütz, G. J. (2018). TCRs are randomly distributed on the plasma membrane of resting antigen-experienced T cells. *Nat. Immunol.*, 19(8):821–827. 21

[115] Rust, M. J., Bates, M., and Zhuang, X. (2006). Sub-diffraction-limit imaging by stochastic optical reconstruction microscopy (STORM). *Nature Methods*, 3:793–796. 21

[116] Sage, P. T., Varghese, L. M., Martinelli, R., Sciuto, T. E., Kamei, M., Dvorak, A. M., Springer, T. A., Sharpe, A. H., and Carman, C. V. (2012). Antigen recognition is facilitated by invadosome-like protrusions formed by memory/effector T cells. *J. Immunol.*, page 1102594. 53

[117] Sakaguchi, S., Fukuma, K., Kuribayashi, K., and Masuda, T. (1985). Organ-specific autoimmune diseases induced in mice by elimination of T cell subset. I. Evidence for the active participation of T cells in natural self-tolerance; deficit of a T cell subset as a possible cause of autoimmune disease. *J. Exp. Med.*, 161(1):72–87. 2

[118] Salaita, K., Nair, P. M., Petit, R. S., Neve, R. M., Das, D., Gray, J. W., and Groves, J. T. (2010). Restriction of receptor movement alters cellular response: physical force sensing by EphA2. *Science*, 327(5971):1380–1385. 66, 71

[119] Sasada, T., Touma, M., Chang, H.-C., Clayton, L. K., Wang, J.-h., and Reinherz, E. L. (2002). Involvement of the tcr Cβ FG loop in thymic selection and T cell function. *J. Exp. Med.*, 195(11):1419–1431. 8

[120] Sauer, M. M., Jakob, R. P., Eras, J., Baday, S., Eriş, D., Navarra, G., Bernèche, S., Ernst, B., Maier, T., and Glockshuber, R. (2016). Catch-bond mechanism of the bacterial adhesin FimH. *Nat. Commun.*, 7:10738. 31

[121] Seiradake, E., Harlos, K., Sutton, G., Aricescu, A. R., and Jones, E. Y. (2010). An extracellular steric seeding mechanism for Eph-ephrin signaling platform assembly. *Nat. Struct. Mol. Biol.*, 17(4):398. 66, 69

[122] Seiradake, E., Schaupp, A., del Toro Ruiz, D., Kaufmann, R., Mitakidis, N., Harlos, K., Aricescu, A., Klein, R., and Jones, E. (2013). Structurally encoded intraclass differences in EphA clusters drive distinct cell responses. *Nat. Struct. Mol. Biol.*, 20(8):98. 69

[123] Sharonov, G. V., Bocharov, E. V., Kosolov, P. M., Astapova, M. V., Arseniev, A. S., and Feofanov, A. V. (2014). Point mutations in dimerization motifs of the transmembrane domain stabilize active or inactive state of the EphA2 receptor tyrosine kinase. *J. Biol. Chem.*, 289(21):14955–14964. 67, 69

[124] Shen, D., Ma, J., Mather, J., Vukmanovic, S., and Radoja, S. (2006). Activation of primary T lymphocytes results in lysosome development and polarized granule exocytosis in $CD4^+$ and $CD8^+$ subsets, whereas expression of lytic molecules confers cytotoxicity to $CD8^+$ cells. *J. Leukoc. Biol.*, 80(4):827–837. 1

[125] Sibener, L. V., Fernandes, R. A., Kolawole, E. M., Carbone, C. B., Liu, F., McAffee, D., Birnbaum, M. E., Yang, X., Su, L. F., Yu, W., Dong, S., Gee, M. H., Jude, K. M., Davis, M. M., Groves, J. T., Goddard III, W. A., Heath, J. R., Evavold, B. D., Vale, R. D., and Garcia,

K. C. (2018). Isolation of a structural mechanism for uncoupling T cell receptor signaling from peptide-MHC binding. *Cell*, 174(3):672–687. 11, 53

[126] Siller-Farfán, J. A. and Dushek, O. (2018). Molecular mechanisms of T cell sensitivity to antigen. *Immunol. Rev.*, 285(1):194–205. 63

[127] Singh, D. R., Ahmed, F., Christopher, K., Gupta, N., Salotto, M., Pasquale, E. B., and Hristova, K. (2015). EphA2 unliganded dimers suppress EphA2 pro-tumorigenic signaling. *J. Biol. Chem.*, 290(45):27271–27279. 65, 66, 68

[128] Springer, T. A. (1990). Adhesion receptors of the immune system. *Nature*, 346(6283):425. 110, 115

[129] Sumen, C., Dustin, M. L., and Davis, M. M. (2004). T cell receptor antagonism interferes with mhc clustering and integrin patterning during immunological synapse formation. *J. Cell Biol.*, 166(4):579–590. 47

[130] Sykulev, Y., Joo, M., Vturina, I., Tsomides, T. J., and Eisen, H. N. (1996). Evidence that a single peptide–MHC complex on a target cell can elicit a cytolytic T cell response. *Immunity*, 4(6):565–571. 32, 52

[131] Taddei, M. L., Parri, M., Angelucci, A., Onnis, B., Bianchini, F., Giannoni, E., Raugei, G., Calorini, L., Rucci, N., Teti, A., Bologna, M., and Chiarugi, P. (2009). Kinase-dependent and-independent roles of EphA2 in the regulation of prostate cancer invasion and metastasis. *Am. J. Pathol.*, 4(174):1492–1503. 65

[132] Tandon, M., Vemula, S. V., and Mittal, S. K. (2011). Emerging strategies for EphA2 receptor targeting for cancer therapeutics. *Expert Opin. Ther. Targets*, 15(1):31–51. 65

[133] Thomas, W. E., Nilsson, L. M., Forero, M., Sokurenko, E. V., and Vogel, V. (2004). Shear-dependent 'stick-and-roll' adhesion of type 1 fimbriated Escherichia coli. *Mol. Microbiol.*, 53(5):1545–1557. 31

[134] Thomas, W. E., Vogel, V., and Sokurenko, E. (2008). Biophysics of catch bonds. *Annu. Rev. Biophys.*, 37(1):399–416. PMID: 18573088. 31

[135] Touma, M., Chang, H.-C., Sasada, T., Handley, M., Clayton, L. K., and Reinherz, E. L. (2006). The TCR Cβ FG loop regulates $\alpha\beta$ T cell development. *J. Immunol.*, 176(11):6812–6823. 8

[136] Upadhyaya, A. (2017). Mechanosensing in the immune response. *Semin. Cell Dev. Biol.*, 71:137–145. 52, 62

[137] Valitutti, S. (2012). The serial engagement model 17 years after: From TCR triggering to immunotherapy. *Front. Immunol.*, 3:272. 45

[138] van der Merwe, P. A. (2002). Formation and function of the immunological synapse. *Curr. Opin. Immunol.*, 14(3):293–298. 15

[139] van der Merwe, P. A. and Davis, S. J. (2002). The immunological synapse–a multitasking system. *Science*, 295(5559):1479. 16

[140] van der Merwe, P. A. and Dushek, O. (2010). Mechanisms for T cell receptor triggering. *Nat. Rev. Immunol.*, 11:47–55. 15

[141] Vaught, D., Brantley-Sieders, D., and Chen, J. (2008). Eph receptors in breast cancer: Roles in tumor promotion and tumor suppression. *Breast Cancer Res.*, 10(6):217. 65

[142] Wang, J.-h., Lim, K., Smolyar, A., Teng, M.-k., Liu, J.-h., Tse, A. G., Liu, J., Hussey, R. E., Chishti, Y., Thomson, C. T., Sweet, R. M., Nathenson, S. G., Chang, H.-C., Sacchettini, J. C., and Reinherz, E. L. (1998). Atomic structure of an $\alpha\beta$ T cell receptor (TCR) heterodimer in complex with an anti-TCR Fab fragment derived from a mitogenic antibody. *EMBO J*, 17(1):10–26. 3

[143] Wofsy, C., Coombs, D., and Goldstein, B. (2001). Calculations show substantial serial engagement of T cell receptors. *Biophys. J.*, 80(2):606–612. 45, 110, 115

[144] Wu, P., Zhang, T., Liu, B., Fei, P., Cui, L., Qin, R., Zhu, H., Yao, D., Martinez, R. J., Hu, W., An, C., Zhang, Y., Liu, J., Shi, J., Fan, J., Yin, W., Sun, J., Zhou, C., Zeng, X., Xu, C., Wang, J., Evavold, B. D., Zhu, C., Chen, W., and Lou, J. (2019). Mechano-regulation of peptide-MHC

class I conformations determines TCR antigen recognition. *Mol. Cell*, 73(5):1015–1027.e7. 6, 15, 46, 110

[145] Wykosky, J., Gibo, D. M., Stanton, C., and Debinski, W. (2005). EphA2 as a novel molecular marker and target in glioblastoma multiforme. *Mol. Cancer Res.*, 10(3):541–551. 65

[146] Xu, Q., Lin, W.-C., Petit, R. S., and Groves, J. T. (2011). EphA2 receptor activation by monomeric ephrin-A1 on supported membranes. *Biophys. J.*, 101(11):2731 – 2739. 65

[147] Yu, Y., Smoligovets, A. A., and Groves, J. T. (2013). Modulation of T cell signaling by the actin cytoskeleton. *J. Cell Sci.*, 126(5):1049–1058. 15

[148] Zhang, Y., Ge, C., Zhu, C., and Salaita, K. (2014). DNA-based digital tension probes reveal integrin forces during early cell adhesion. *Nat. Commun.*, 5:5167. 21

[149] Zhu, C., Jiang, N., Huang, J., Zarnitsyna, V. I., and Evavold, B. D. (2013). Insights from *in situ* analysis of TCR–pMHC recognition. *Immunol. Rev.*, 251(1):49–64. 32

Appendices

A Introduction: Tables and Figures

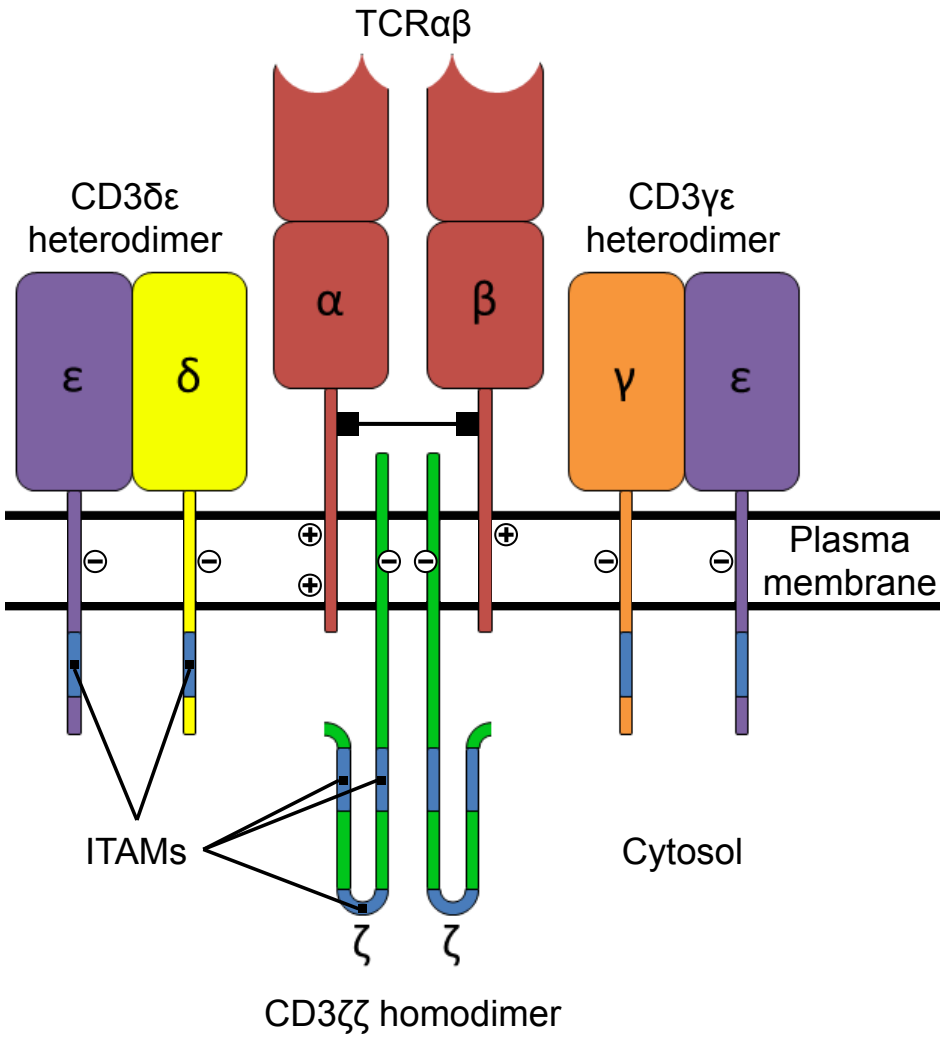

Figure A.1: TCR-CD3 complex. The TCR has an α and β chain, each of which contain a variable domain, constant domain, and short transmembrane tail. The α and β chains are linked by a disulfide-bridge. The CD3$\delta\varepsilon$, CD3$\gamma\varepsilon$, and CD3$\zeta\zeta$ chains comprise the CD3 complex and associate with the TCR. ITAMs are located on each CD3 chain and are phosphorylated by kinases, e.g. Lck and ZAP70, upon TCR engagement with a ligand. Negative charges in the CD3 chains interact with the positve charges of the TCR. This figure is adapted from Wikimedia Commons.

B Catch bonds at T-cell interfaces: Tables and Figures

Table B1: Model variables and parameters.

Variable	Definition	Value	Units
$C_{\mathrm{SM}}(x,y,t)$	Concentration of surface molecules (SMs)	—	$[\mu\mathrm{m}^{-2}]$
$z(x,y,t)$	Intermembrane distance	—	[nm]
$C_{\mathrm{SM},0}$	Initial concentration of SMs	1000	$[\mu\mathrm{m}^{-2}]$
D	Diffusion coefficient	0.01	$[\mu\mathrm{m}^2/s]$
κ	Membrane bending rigidity	12.15, 40	$[k_{\mathrm{B}}T]$
k_p	Compressional stiffness of SMs	0.1	[pN/nm]
z_p	Natural length of SMs	50	[nm]
z_o	TCR-pMHC complex height	13	[nm]
Δx	Lattice spacing	10	[nm]
Δt	Time step	7.5×10^{-4}	[s]

Table B2: Average force ($\langle f \rangle$) and standard deviation (σ) on a bond given that a second bond is located a fixed distance away. The averages and standard deviations are calculated for $t > 0.5$ s. Forces reported without a standard deviation are the average force at the final time point (1 s) of simulations without thermal fluctuations.

	$\kappa = 12.15\ k_{\mathrm{B}}T$	$\kappa = 40\ k_{\mathrm{B}}T$
Separation (nm)	$\langle f \rangle \pm \sigma$ (pN)	$\langle f \rangle \pm \sigma$ (pN)
20	3.43 ± 6.16	7.06 ± 11.38
	3.63	7.14
40	3.56 ± 6.24	7.23 ± 11.39
	3.79	7.38
80	3.78 ± 6.01	7.56 ± 11.74
	4.25	8.11
160	6.87 ± 6.34	9.67 ± 11.63
	7.16	11.42
single bond	7.07 ± 6.32	13.46 ± 11.60
	6.99	13.90

Table B3: Average force ($\langle f \rangle$) and standard deviation (σ) on edge bonds and the center bond in a configuration with three colinear bonds. The separation distance is the distance between each edge bond and the center bond. The averages and standard deviations are calculated for $t > 0.5$ s.

	Edge Bonds $\langle f \rangle \pm \sigma$ (pN)	Center Bond $\langle f \rangle \pm \sigma$ (pN)
20 nm separation	10.89 ± 11.31	-7.64 ± 10.81
40 nm separation	10.20 ± 11.68	-4.58 ± 11.34
80 nm separation	10.06 ± 11.51	-0.46 ± 11.40

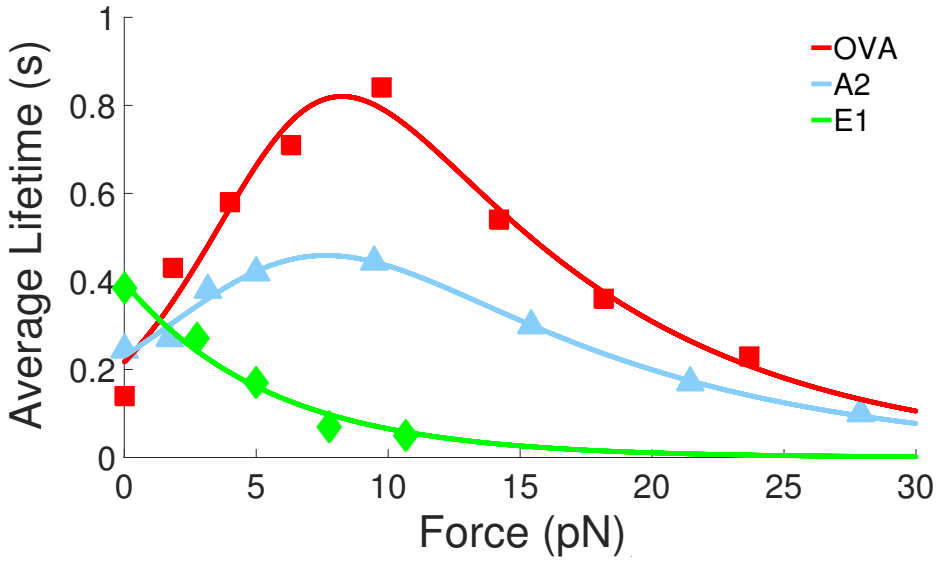

Figure B.1: Force-dependent lifetime data (points) for the OT1 TCR bound to three different ligands. Data points are from Liu et al. (76). OVA and A2 exhibit catch-bond behavior. Solid lines are nonlinear least squares fits to the data using Eqn. 2.1 for E1 and Eqn. 2.2 for OVA and A2.

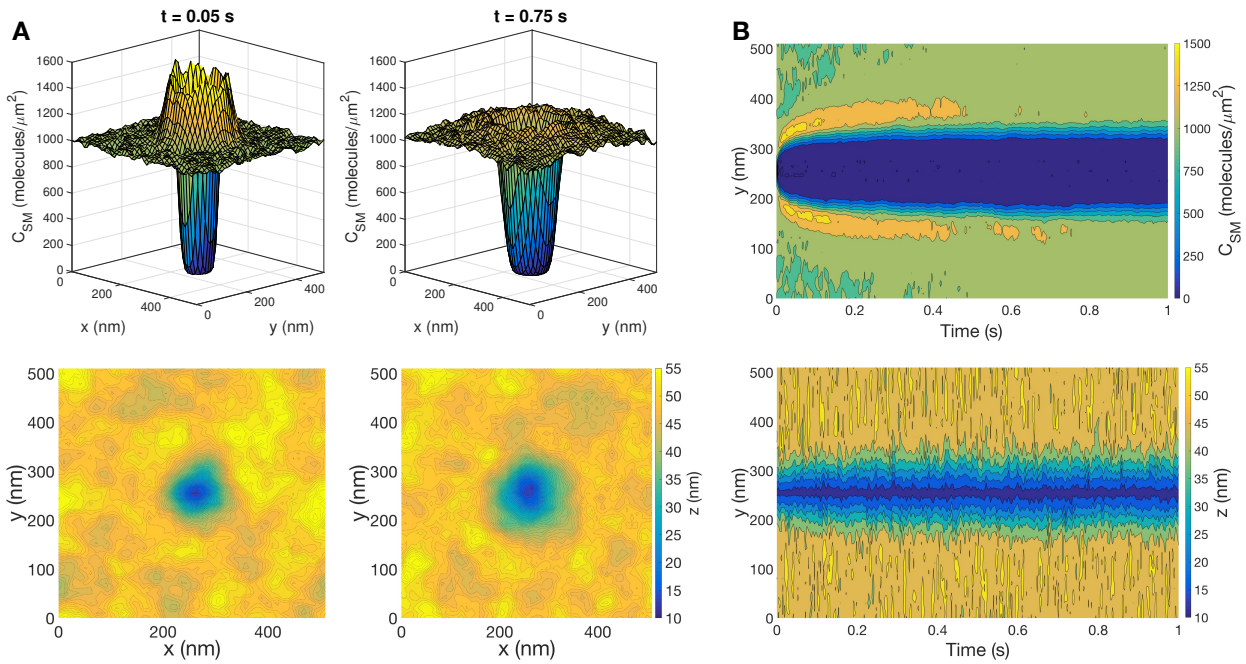

Figure B.2: Characteristic response to the formation of a bond (with thermal fluctuations). (A) Snapshots of the surface molecule concentration (top row) and the intermembrane distance (bottom row) with $\kappa = 12.15\ k_{\mathrm{B}}T$. Each column corresponds to a different time point. The bond is located at the center of the domain. (B) Kymographs of C_{SM} and z from a one-dimensional slice containing the bond.

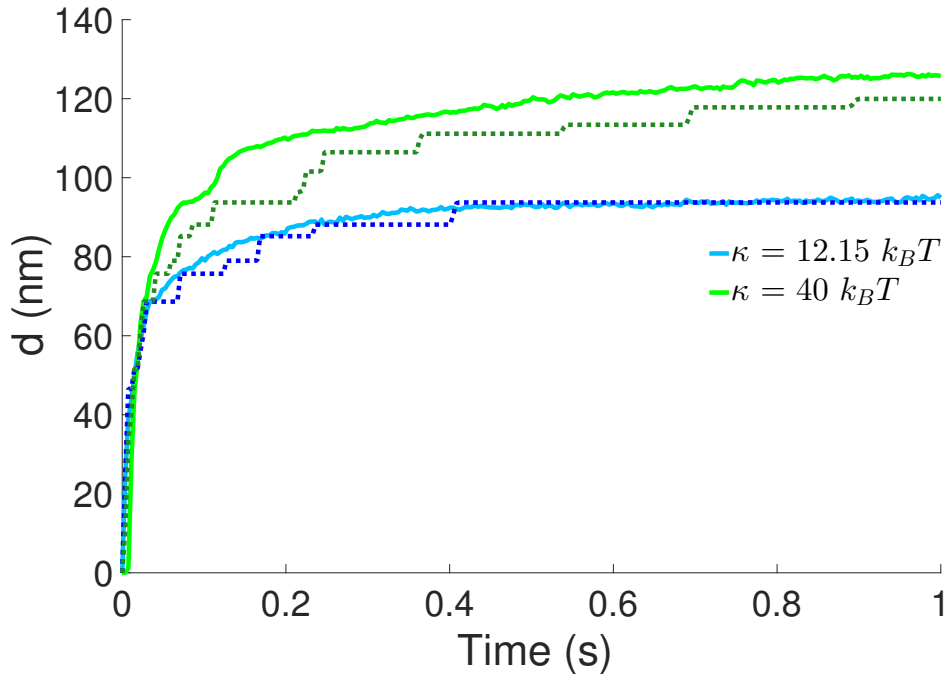

Figure B.3: Time evolution of the effective diameter (d) of the depletion zone. Data is averaged over ten independent trajectories for each condition. Simulations with thermal fluctuations (solid lines) lead to a more rapid expansion of the depletion zone than simulations without thermal fluctuations (dashed lines). Increasing the membrane stiffness, κ, promotes the formation of a larger depletion zone.

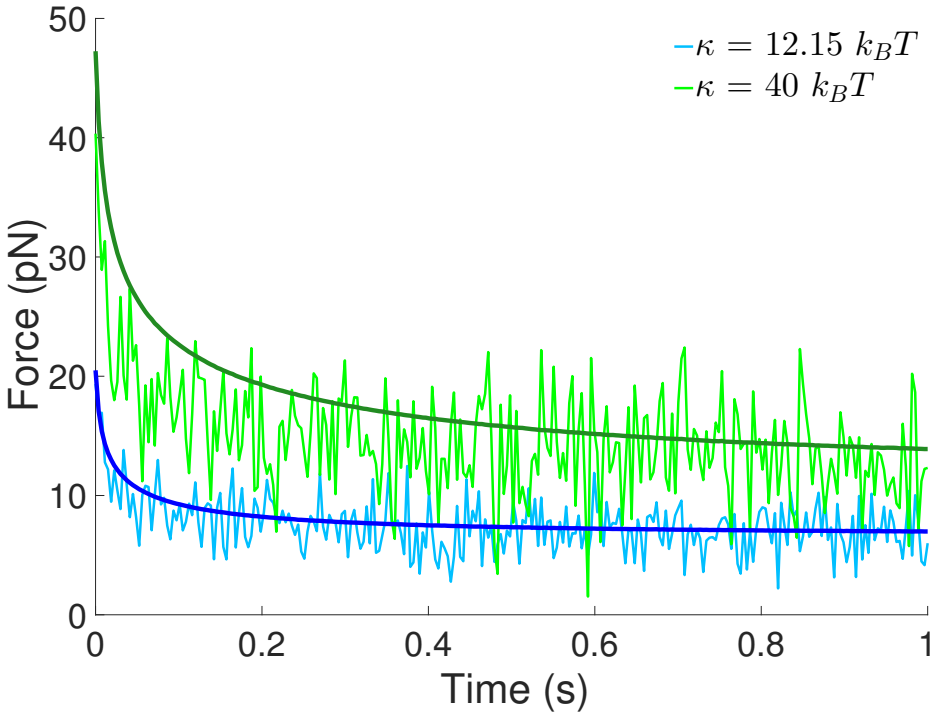

Figure B.4: Average bond tension as a function of time. The average tension at each time point is calculated by averaging the tension from ten independent simulation trajectories with $\kappa = 12.15$ $k_{\mathrm{B}}T$ (blue) and $\kappa = 40$ $k_{\mathrm{B}}T$ (green). The cases without fluctuations are shown in darker shades.

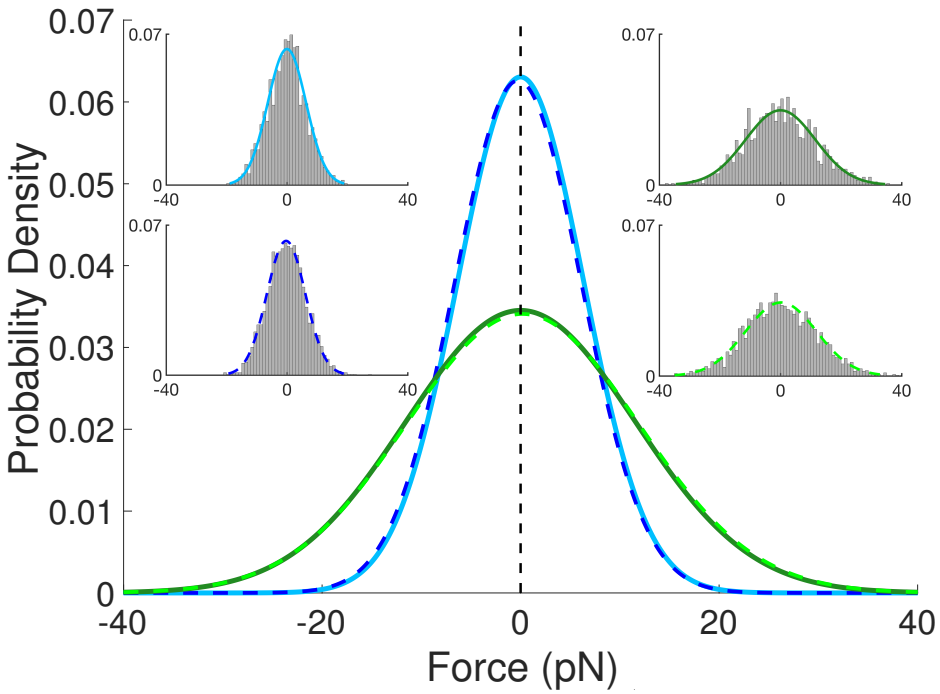

Figure B.5: Gaussian fits of the probability densities for the mean-centered forces obtained from simulations with and without surface molecules present. Results are shown for $\kappa = 12.15\ k_{\mathrm{B}}T$ (blue) and $\kappa = 40\ k_{\mathrm{B}}T$ (green). Histograms of mean-centered force data are included as insets for cases with (solid) and without (dashed) surface molecules. Each condition uses data from ten trajectories, with forces for $t > 0.5$ s used when surface molecules are present.

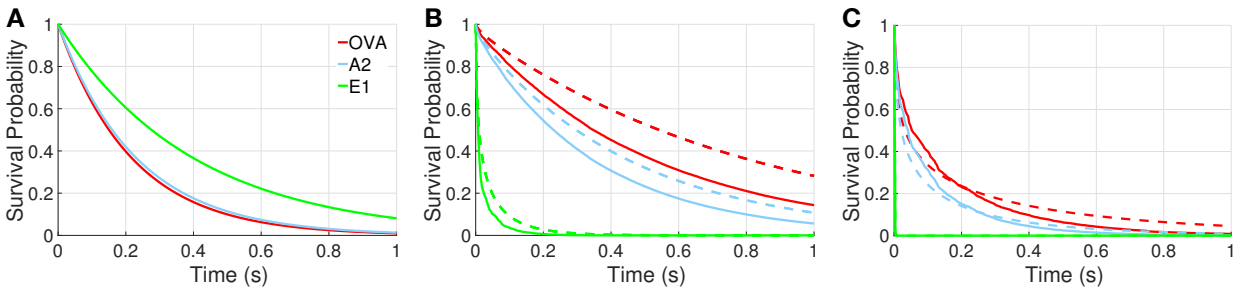

Figure B.6: Survival probabilities for different ligands. Each survival probability curve is calculated by averaging ten independent survival curves. Different ligands (OVA, A2, and E1) are considered with (solid) and without (dashed) thermal fluctuations. (A) Survival probabilities with zero applied force. In this case, the slip bond (E1) exhibits the longest average lifetime. (B) Survival probabilities with $\kappa = 12.15\ k_{\mathrm{B}}T$. (C) Survival probabilities with $\kappa = 40\ k_{\mathrm{B}}T$.

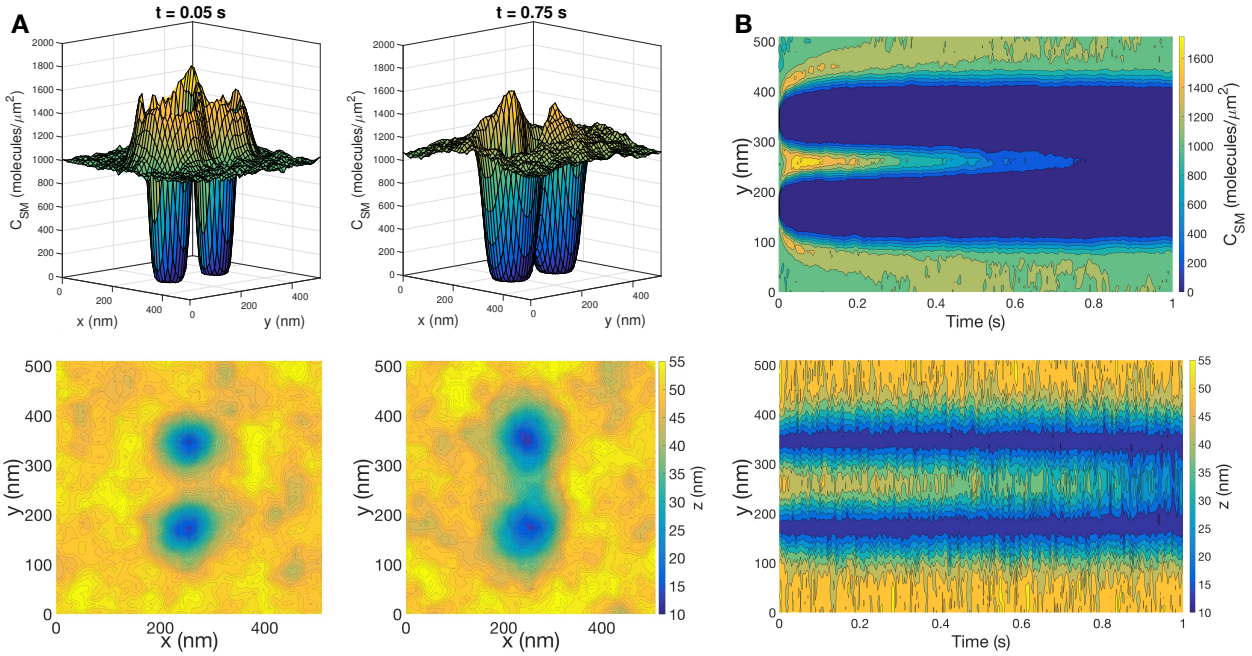

Figure B.7: Characteristic response to the formation of two bonds separated by 160 nm (with thermal fluctuations). (A) Snapshots of C_{SM} (top row) and z (bottom row) with $\kappa = 12.15\ k_{\mathrm{B}}T$. Each column corresponds to a different time point. (B) Kymographs of C_{SM} and z from a one-dimensional slice containing both bonds.

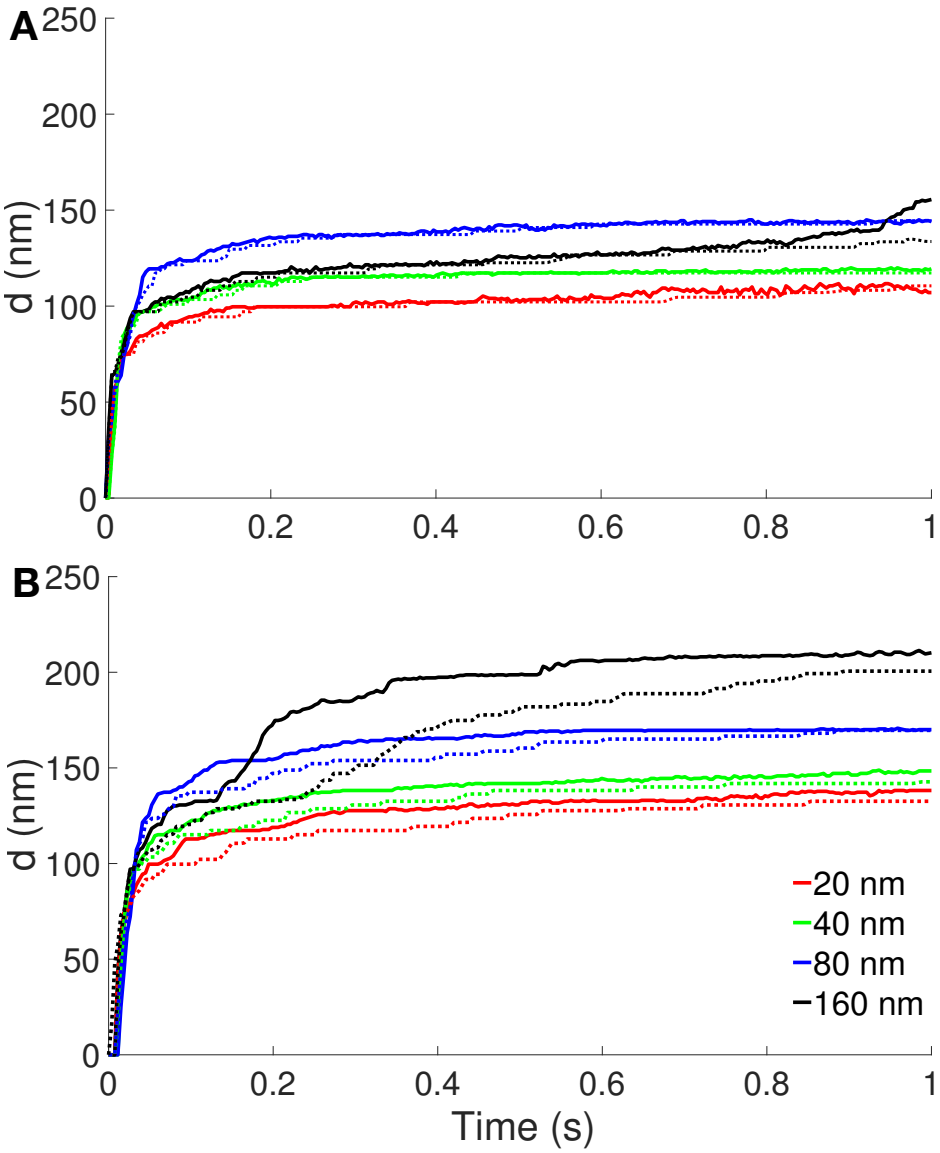

Figure B.8: Time evolution of the effective diameter (d) of the depletion zone for two bonds separated by different distances. Data is averaged over ten independent trajectories for each condition. (A) $\kappa = 12.15\ k_{\mathrm{B}}T$. (B) $\kappa = 40\ k_{\mathrm{B}}T$.

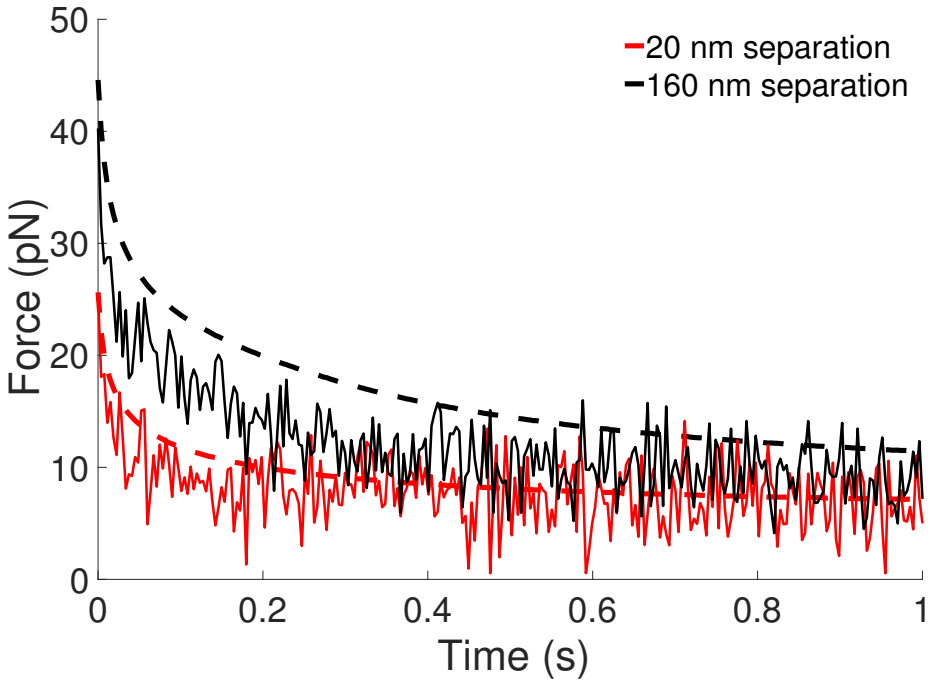

Figure B.9: Average force on a bond when a second bond is a fixed distance away. Results with (solid) and without (dashed) thermal fluctuations are shown for $\kappa = 40\ k_{\mathrm{B}}T$. For each case, data is averaged over ten independent trajectories. The average bond tension increases with increased separation.

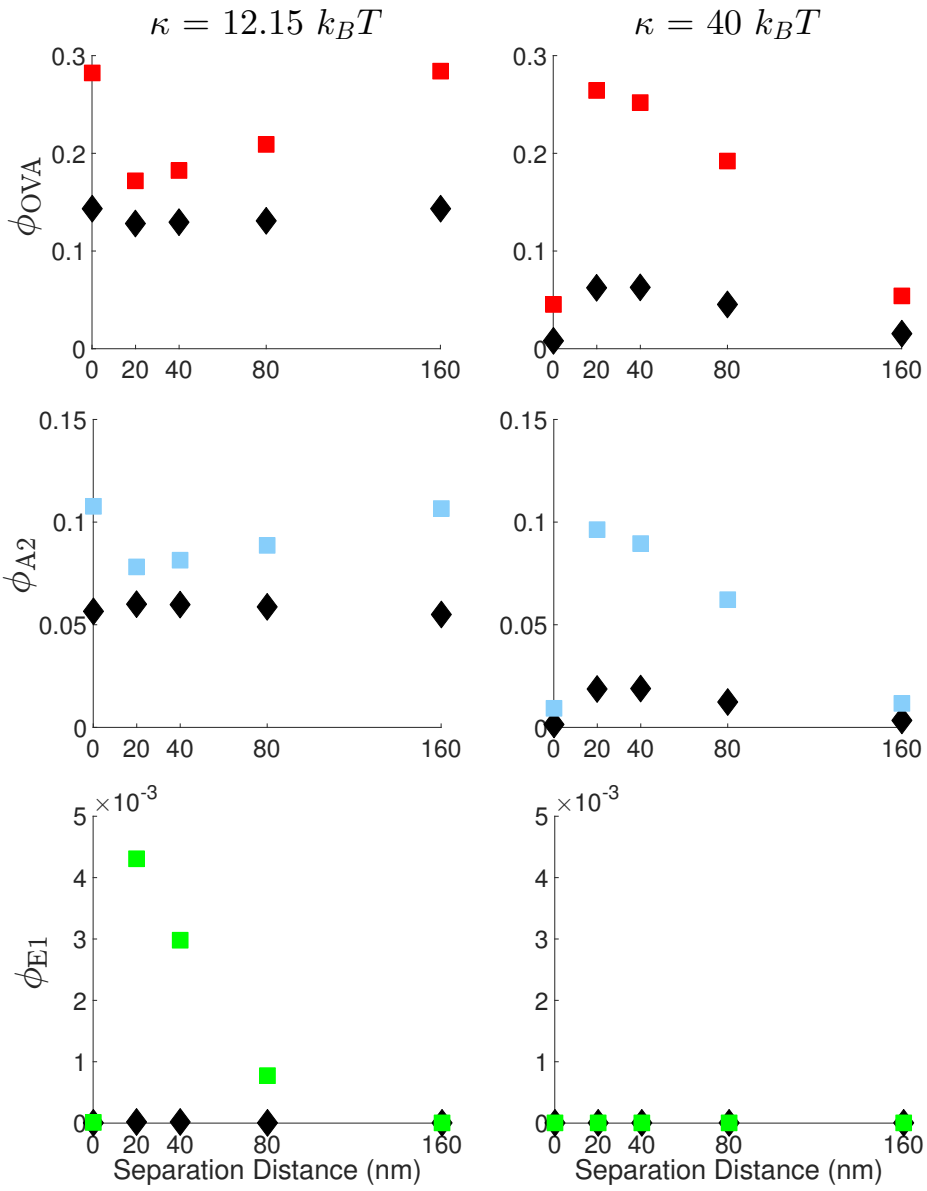

Figure B.10: Fraction of bonds that remain at $t = 1$ s as a function of bond separation distance. Rows correspond to different ligands (OVA, A2, and E1) and columns correspond to different values of κ. Results with (diamonds) and without (squares) fluctuations are shown. The values of ϕ reported with a separation distance of zero correspond to a single bond. All other cases have two bonds. For every condition tested, the catch bonds have a larger binding fraction that the slip bond.

B.1 Supporting Material

Catch bond parameter fitting and analysis of effective off-rates

In this section, we show kinetic parameter fits to experimental data, analysis of the time step given a discretized lattice size, the impact of zero thermal fluctuations, and analysis of effective off-rates for each TCR-pMHC complex given an average applied force with an exponentially-distributed random force.

Table B4: Receptor-ligand binding kinetics for TCR-pMHC complexes given Bell and two-pathway models.

	$k_0\ (1/s)$	f_0 (pN)	$k_c\ (1/s)$	f_c (pN)	$k_s\ (1/s)$	f_s (pN)
OVA	—	—	4.241	3.150	0.374	9.280
A2	—	—	3.610	4.466	0.735	10.460
E1	2.514	5.533	—	—	—	—

Parameters were obtained by a nonlinear least squares fit of the lifetime data from Liu et al. (76):

Methods: Determination of time step and system size

The explicit finite difference method is conditionally stable and relies on the relation between the dimensionality, spatial discretization, and time step of the system. The Courant-Friedrichs-Lewy (CFL) condition imposes a recurrence relation that relates the spatial discretization of a lattice to the time step for the general N-dimensional heat equation. However, with the addition of the advection term, it is necessary to consider additional stability arguments (47). For a general advection-diffusion PDE of the form

$$\frac{\partial \phi(\vec{x},t)}{\partial t} = \sum_{i=1}^{N} \left(D_i \frac{\partial^2 \phi}{\partial x_i^2} - u_i \frac{\partial \phi}{\partial x_i} \right),$$

both of the following conditions must be met to maintain numerical stability with a forward-time central-space scheme

$$(i)\ \sum_{i=1}^{N} \frac{2D_i \Delta t}{(\Delta x_i)^2} \leq 1 \quad \text{and} \quad (ii)\ \sum_{i=1}^{N} \frac{u_i^2 \Delta t}{2D_i} \leq 1.$$

The first inequality implies the CFL condition and is more restrictive for a diffusion-dominated system. The second inequality is more restrictive for an advection-dominated system. While these conditions do not map directly to our system as E_p depends on the changing intermembrane distance profile, they provide a good baseline to test for a stable time step that can be verified through subsequent simulations. After assuming an extreme case where numerical instability is most likely to be prevalent (initial time point), we calculate the appropriate time step as a function of the compressional stiffness at a given lattice spacing (Fig. B.11).

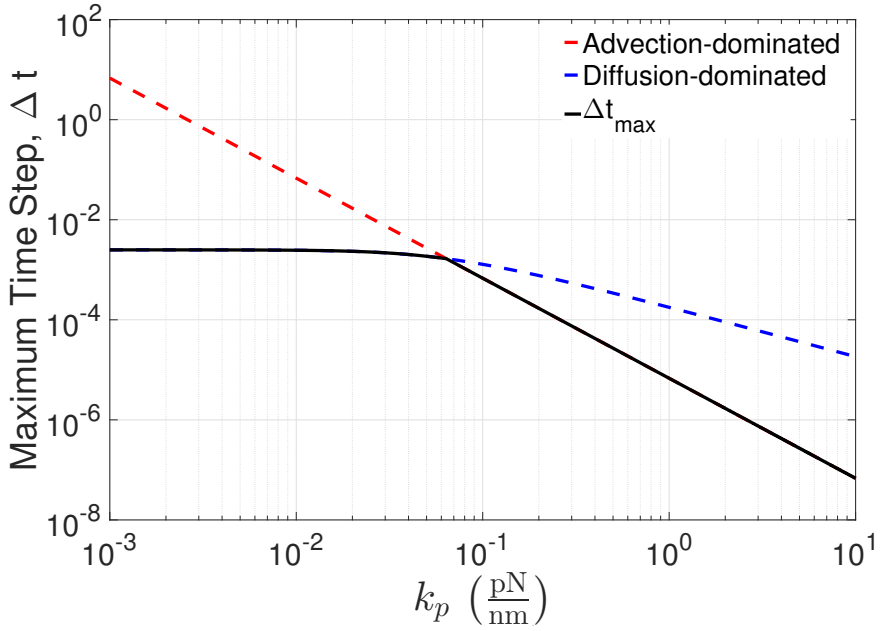

Figure B.11: Maximum time step as a function of the compressional stiffness (k_p) given a lattice spacing of 10 nm.

In addition to evaluating the time step, it is important to ensure that finite-size effects do not have an impact on the simulation results. We ran ten individual trajectories at several system sizes and calculated the effective depletion zone diameters at $t = 1$ s. There was no significant difference in the depletion zone diameter for periodic domains larger than 400 nm $\times$ 400 nm.

Dynamics with $\beta \to \infty$ (no thermal fluctuations)

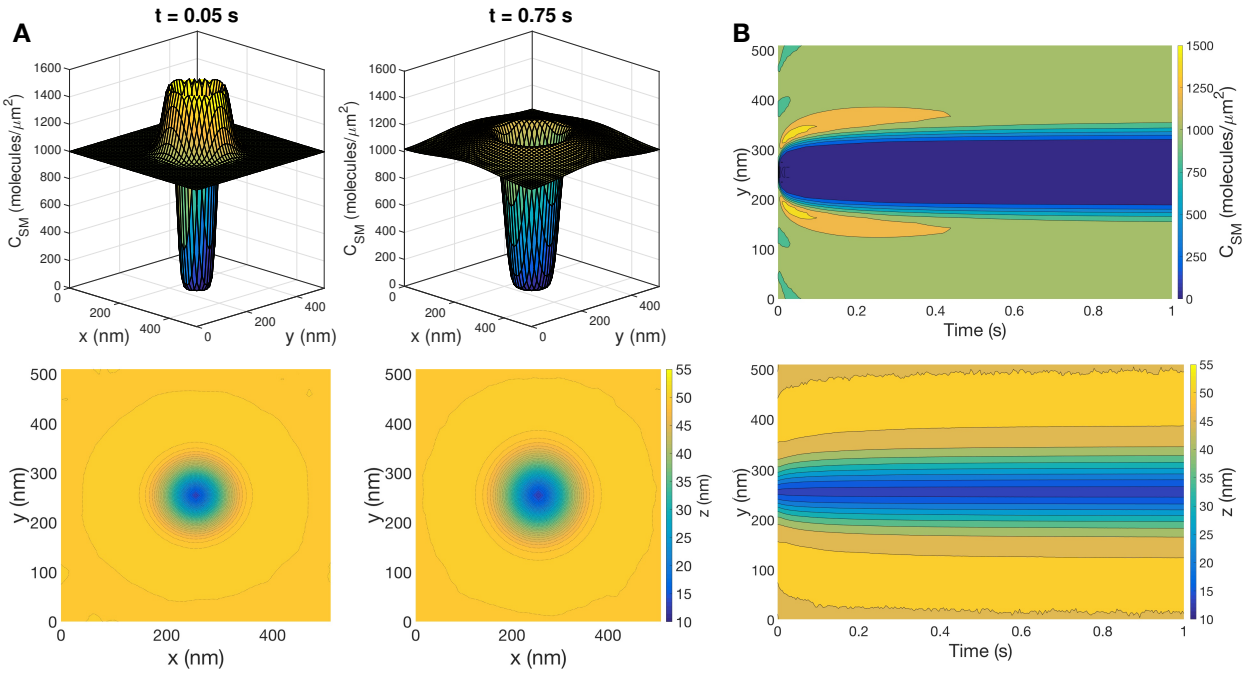

Figure B.12: Characteristic response to the formation of a bond without thermal fluctuations. (A) Snapshots of C_{SM} (top row) and z (bottom row) with $\kappa = 12.15\ k_B T$. Each column corresponds to a different time point. The bond is located at the center of the domain. (B) Kymographs of C_{SM} and z from a one-dimensional slice containing the bond.

Effective off rates

Here, we present results obtained by numerically evaluating Eqn. 2.8. Given an average force (f_A) on a bond, we compute the ratio of the effective off rate (averaged over fluctuations) to the off rate $k_{\text{off}}(f_A)$. We compute the quantity for OVA, A2, and E1 assuming that $k_{\text{off}}(-f) = k_{\text{off}}(f)$ and using the standard deviations obtained from simulations.

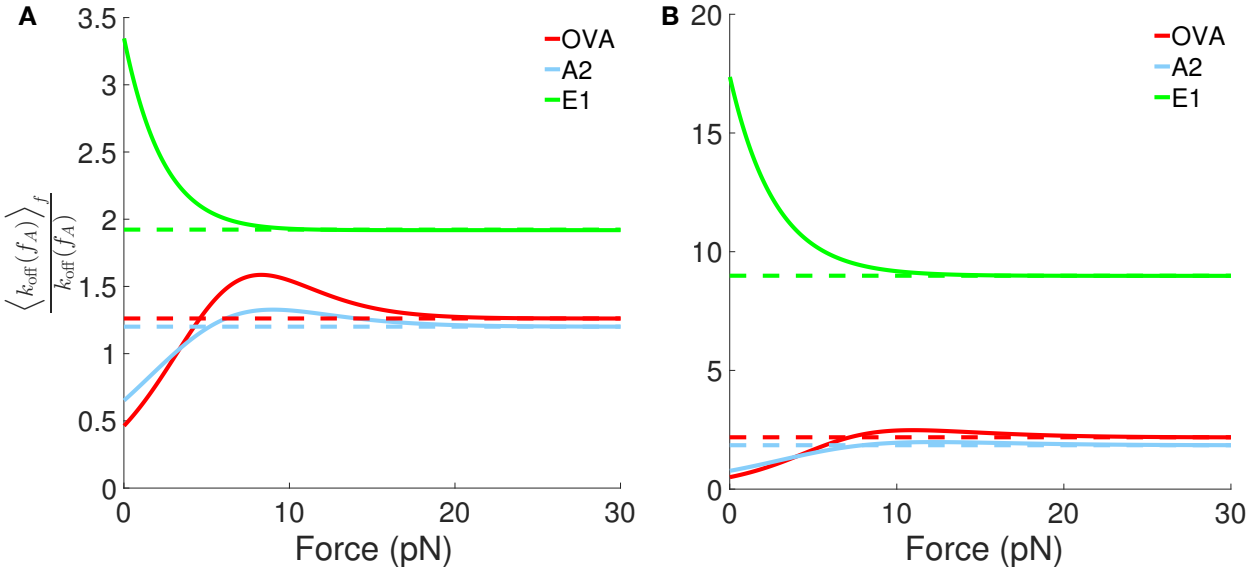

Figure B.13: Ratio of the effective off rate to $k_{\text{off}}(f_A)$ for different ligands. Solid lines are obtained by numerically integrating (Equation Number). Dashed lines are analytical results obtained in the limit $f \gg f_c$. (A) $\kappa = 12.15\ k_{\text{B}}T$. (B) $\kappa = 40\ k_{\text{B}}T$.

C Dynamics of T-cell receptor cluster formation: Tables and Figures

Table C1: Parameters used in the TDGL hybrid model.

Variable	Definition	Value	Units	Source
D_{bond}	Diffusion coefficient, TCR-pMHC bond	1.00×10^{-2}	$[\mu\text{m}^2/s]$	—
D_{CD45}	Diffusion coefficient, CD45	1.00×10^{-2}	$[\mu\text{m}^2/s]$	(2)
D_{pMHC}	Diffusion coefficient, pMHC	3.00×10^{-2}	$[\mu\text{m}^2/s]$	(143)
D_{TCR}	Diffusion coefficient, TCR	3.40×10^{-2}	$[\mu\text{m}^2/s]$	(18)
k_{bond}	Compressional stiffness of bonds	1.00	[pN/nm]	(144)
k_{CD45}	Compressional stiffness of CD45	1.00	[pN/nm]	(107)
$k^{\text{on}}_{\text{nonstim}}$	2D on-rate, nonstimulatory pMHC	2.60×10^{2}	$[\text{nm}^2/s]$	(54)
$k^{\text{on}}_{\text{stim}}$	2D on-rate, stimulatory pMHC	2.40×10^{5}	$[\text{nm}^2/s]$	(54)
M	Phenomenological constant	5.00×10^{3}	$[\text{nm}^3/(\text{pN} \cdot s)]$	—
z_{bond}	TCR-pMHC complex length	13	[nm]	(128)
z_{CD45}	CD45 length	40	[nm]	(23)
Δx	Lattice spacing	10	[nm]	(14)

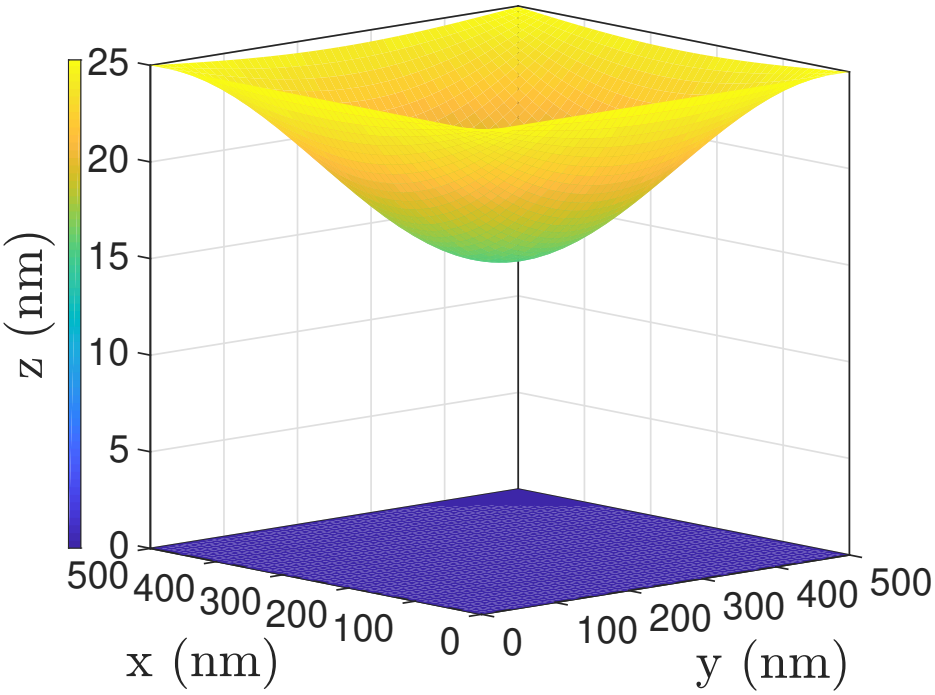

Figure C.1: Initial intermembrane distance profile. The system size is 500 nm $\times$ 500 nm with a spatial discretization of 10 nm, which is commensurate with the footprint of a single TCR complex within the T-cell membrane (14).

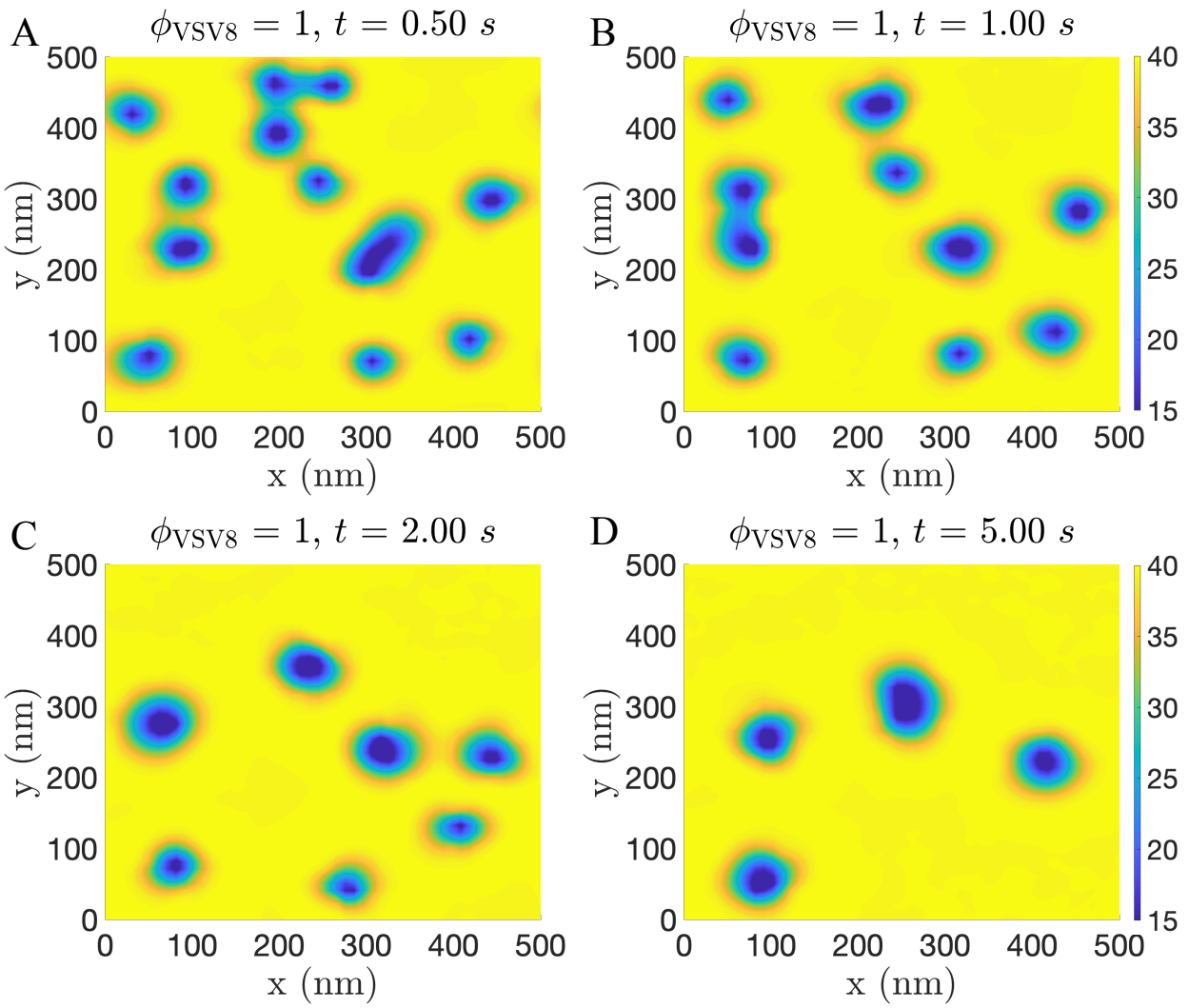

Figure C.2: Time evolution of the intermembrane distance profile given ρ_{pMHC} = 1000 molecules / μm^2, ϕ_{VSV8} = 1.00. Clusters rapidly form due to the close proximity of the two apposed membranes and the high on-rate for stimulatory TCR-pMHC interactions. As time progresses, smaller clusters coalesce to form larger aggregates. By the final time point, only four clusters remain.

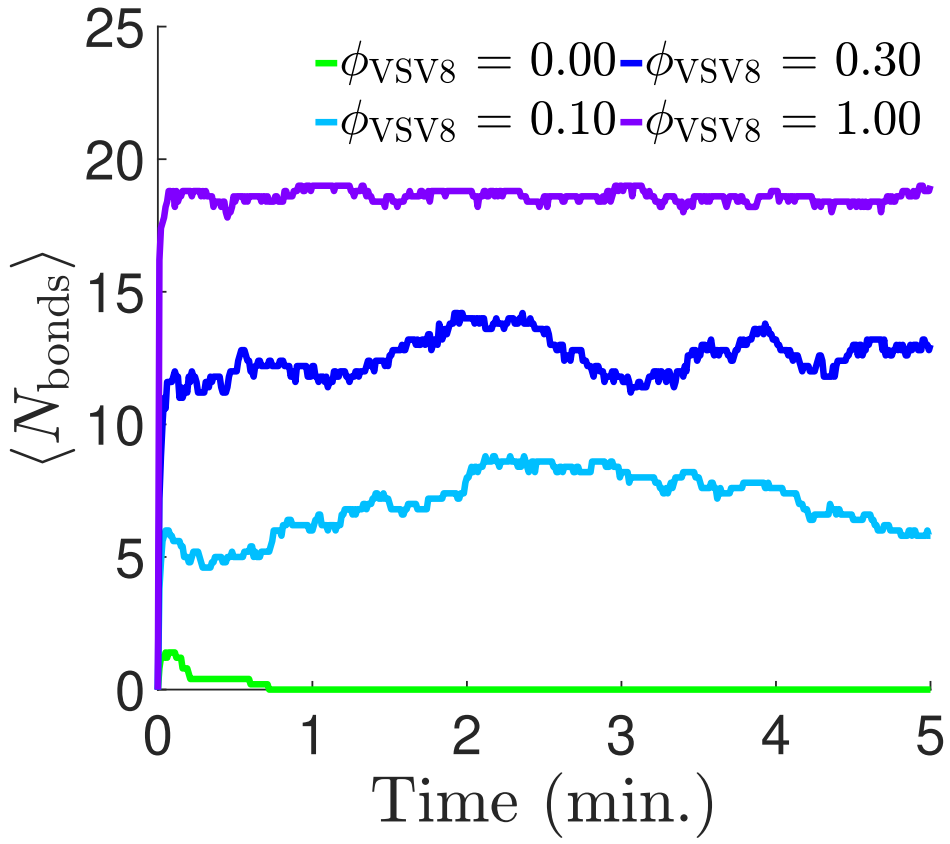

Figure C.3: Average total number of bonds as a function of time and fraction of agonist pMHC given a constant pMHC molecule density of 1000 molecules / μm^2. Due to the close proximity and energetically favorable initial configuration of the two membranes, TCR-pMHC complexes rapidly accumulate at early times. The average number of TCR-pMHC complexes fluctuates about a constant value at longer-lived times. A total of five independent trajectories were sampled for each case.

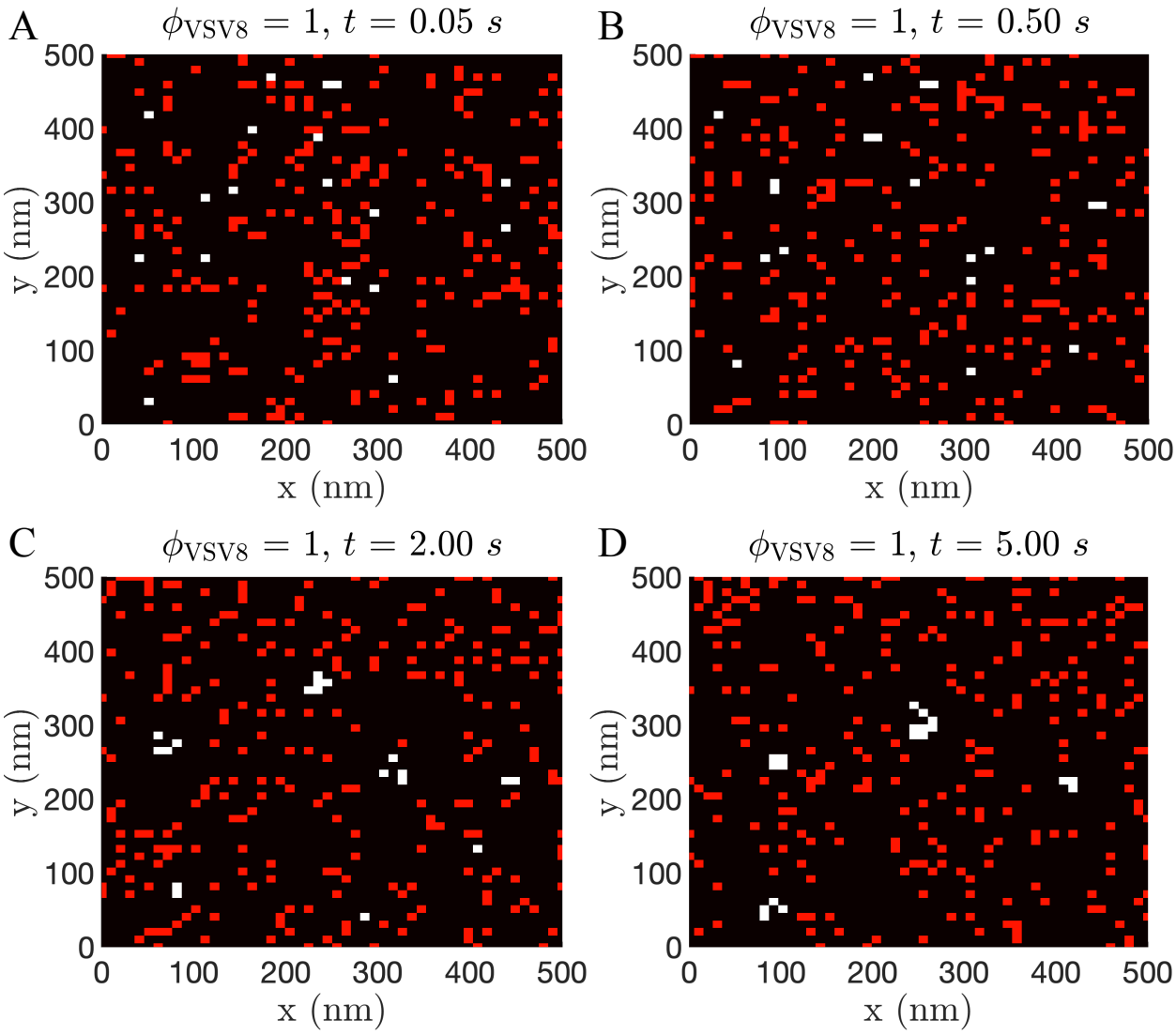

Figure C.4: The spatiotemporal evolution of TCR-pMHC complexes and CD45 phosphatases. TCR-pMHC complexes (white) coalesce over time and form separate protein domains from the longer CD45 surface molecules (red) within the intercellular junction.

D Scanning microvilli at T-cell surfaces: Tables and Figures

Table D1: Parameters used in the model.

Variable	Definition	Value	Units	Source
D_{pMHC}	Diffusion coefficient, pMHC	3.00×10^{-3}	$[\mu m^2/s]$	(143)
D_{TCR}	Diffusion coefficient, TCR	0.01	$[\mu m^2/s]$	(36)
Δr	Diffusive step length	10	[nm]	—
V_0	Microvillus velocity, no force	5.20	[μm/min]	(63)
f_{MV}	Threshold force, microvillus velocity	50	[pN]	—
k_{bond}	Compressional stiffness of bonds	1.00	[pN/nm]	(107)
$k_{\text{nonstim}}^{\text{on}}$	2D on-rate, nonstimulatory pMHC	2.6×10^2	$[nm^2/s]$	(54)
$k_{\text{stim}}^{\text{on}}$	2D on-rate, stimulatory pMHC	2.4×10^5	$[nm^2/s]$	(54)
z_{bond}	TCR-pMHC complex length	13	[nm]	(128)
Δt	Time step	2.5×10^{-5}	[s]	—

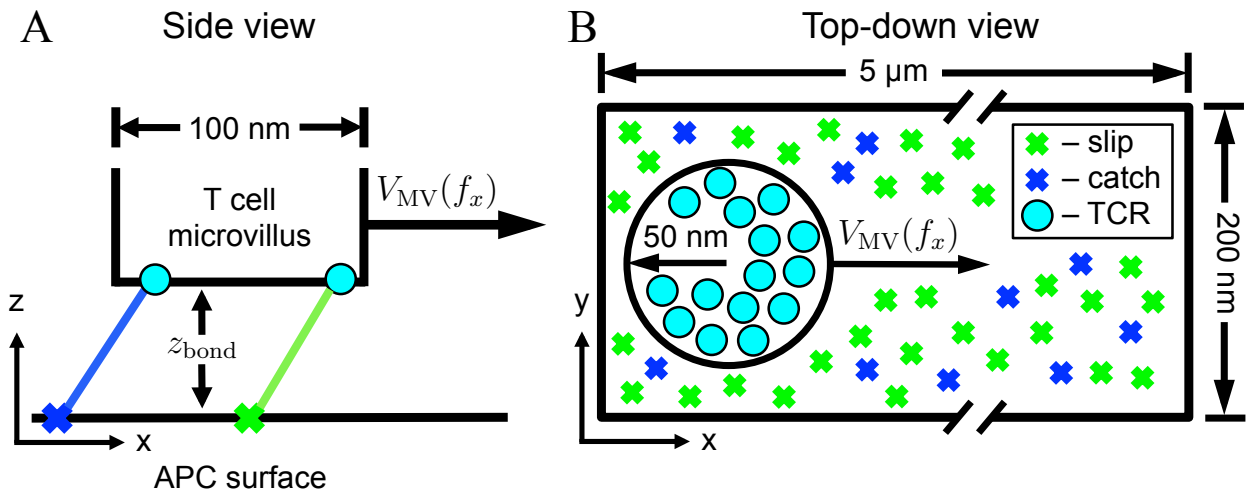

Figure D.1: Schematic of a T-cell microvillus scanning across the surface of an antigen-presenting cell. TCR-pMHC bonds stochastically form and dissociate as the microvillus moves across the APC surface. The velocity, V_{MV}, depends on the force exerted on the microvillus tip by TCR-pMHC complexes. (A) Side view of the system with the T-cell microvillus tip residing above the APC surface. (B) Top-down view. The microvillus moves in the x-direction. A mixed population of pMHC is shown; some form catch bonds upon binding TCRs while others form slip bonds.

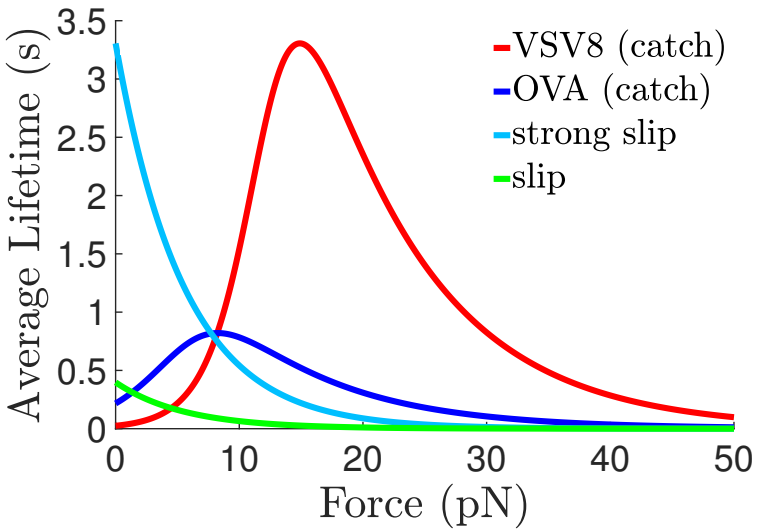

Figure D.2: Average TCR-pMHC lifetimes as a function of tensile force. Curves for VSV8, OVA, and slip were fit using nonlinear least square fits of experimental data from Refs. (76) and (37). The "strong slip" bond is a hypothetical control with the same maximum average lifetime as VSV8 and the same reference force as the slip bond.

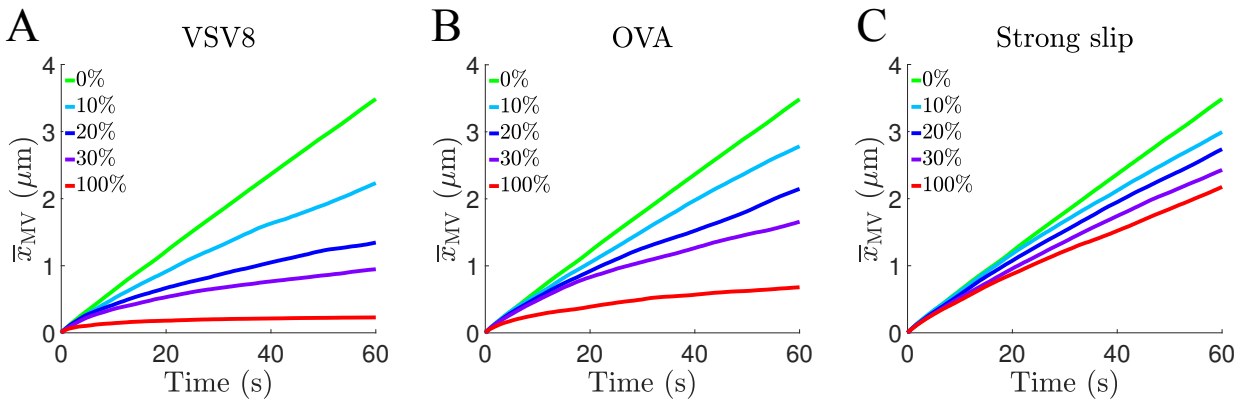

Figure D.3: The average microvillus displacement for different fractions of stimulatory pMHC: (A) VSV8, (B) OVA, and (C) strong slip. Each line shows the average displacement from 25 independent trajectories.

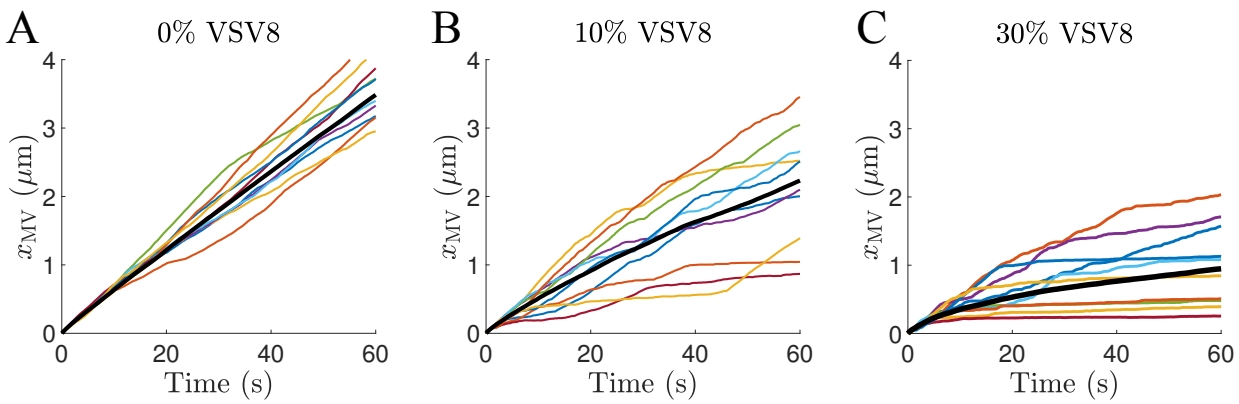

Figure D.4: Displacements of microvilli for (A) nonstimulatory pMHC, (B) 10% VSV8 pMHC, and (C) 30% VSV8 pMHC. Black lines show the average microvillus displacement calculated from 25 independent trajectories. Colored lines show the displacement of individual microvilli (10 shown).

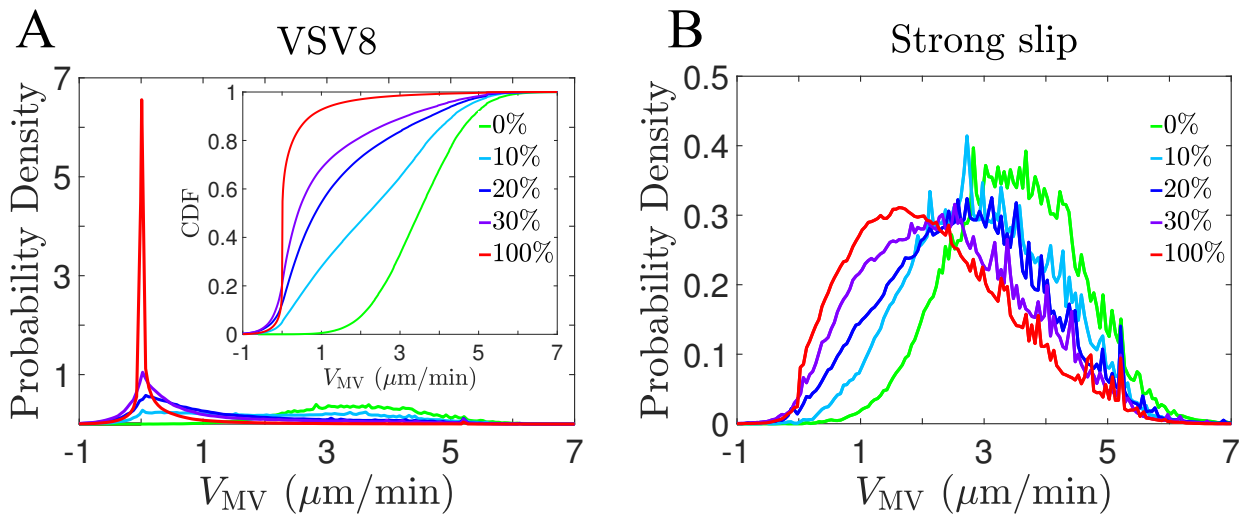

Figure D.5: (A) Probability density and cumulative distribution functions (inset) of the microvillus velocity at various fractions of VSV8 pMHC. (B) Probability density of the microvillus velocity at various fractions of strong-slip pMHC. Each distribution is constructed from the velocities obtained over the course of 25 independent trajectories. The green curve (0%) is the same on both figures.

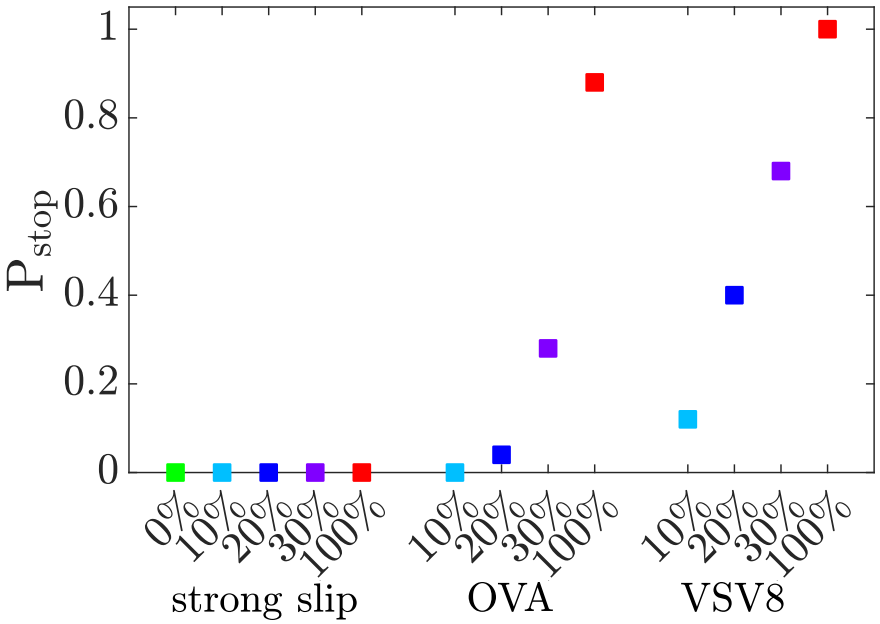

Figure D.6: The probability that a microvillus is immobilized ("stops") within 1 minute of scanning. A "stopping event" occurs when the average velocity is ≤ 0.25 μm/min for a continuous period of at least 10 s. Each point is obtained from 25 independent trajectories.

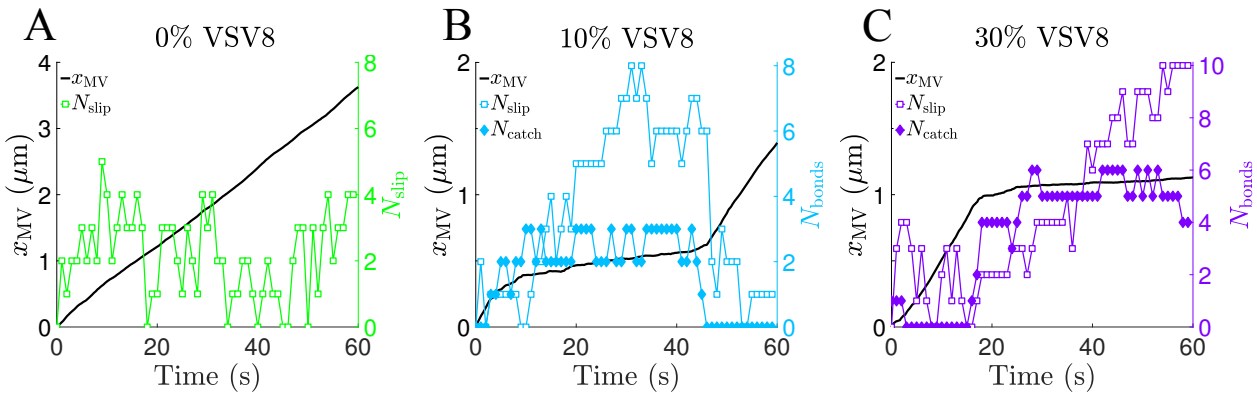

Figure D.7: The number of catch and slip bonds (colored lines, right axes) and the microvillus displacement (black lines, left axes) for sample trajectories at three fractions of VSV8 pMHC (A-C).

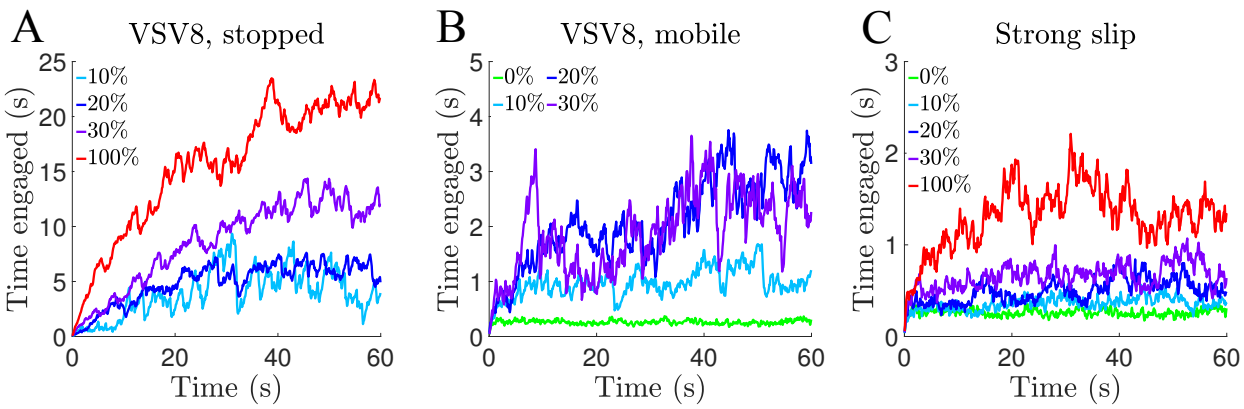

Figure D.8: The average cumulative time of receptor engagement for various systems: (A) VSV8 with stopped microvilli, (B) VSV8 with mobile microvilli, and (C) strong-slip pMHC. No stopping events were observed for the strong-slip case.

D.1 Supporting Material

In this section, we expand upon the computational details of the algorithm, parameterize receptor-ligand bond kinetics, and test a different functional form for the microvillus velocity.

Methods: Computational details

The dynamics of the system are described by a discrete-time, continuous-space stochastic algorithm. This choice was physically motivated by describing the microvillus position as a function of time. The time step (Δt) was chosen to be sufficiently small so that the discrete-time algorithm provides a good approximation of the underlying continuous-time process. During each time step, the algorithm allows for diffusive hops of particles, binding of TCRs and pMHCs, and dissociation of bonds. At the end of each time step, the position of the microvillus is updated in accordance with its velocity, which impacts the state of the system by changing the lengths of TCR-pMHC bonds and the positions of TCRs relative to the antigen-presenting surface.

Unbound pMHC molecules and TCRs diffuse on the antigen-presenting surface and microvillus tip, respectively. In time interval Δt, the probability that a given particle attempts a diffusive move is

$$P_{\text{diff}} = 1 - e^{-4D\Delta t/\Delta r^2} , \tag{1}$$

where D is the diffusion coefficient and Δr is the displacement. The diffusive step consists of the particle moving a distance Δr at a randomly generated angle. The move is accepted if the new position does not overlap with other particles and remains within the appropriate boundaries; otherwise it is rejected and the particle stays at the original location.

The binding of a TCR with a pMHC is governed by an intrinsic on-rate that decays like a Gaussian as the distance varies from the natural length of the TCR-pMHC complex. The total probability of binding for a particular TCR is

$$P_{\text{bind}} = 1 - \exp\left(-\Delta t \sum_{i=1}^{n_{\text{pMHC}}} k^{\text{on}} e^{-(L_i - z_{\text{bond}})^2/2\sigma^2} \right) , \tag{2}$$

where n_{pMHC} is the number of unbound pMHC molecules within binding distance, k^{on} is the 2D on-rate for the TCR-pMHC reaction, and L_i is the distance between the TCR and the i^{th} pMHC molecule. If a binding reaction occurs, the pMHC is chosen with a probability proportional to its individual on-rate with the TCR. We set $\sigma = 5$ nm and restrict the maximum distance for binding between two particles to be twice the natural length of the TCR-pMHC complex ($2z_{\text{bond}}$). The probability that a TCR-pMHC complex dissociates within the time interval Δt is

$$P_{\text{diss}} = 1 - e^{-k_{\text{off}}(f)\Delta t} , \tag{3}$$

where $k_{\text{off}}(f)$ is the ligand-dependent off-rate.

Upon completion of all diffusive and binding processes, the TCR positions and microvillus tip are updated by moving the microvillus a distance of $V_{\text{MV}}(t)\Delta t$ in the x-direction. The forces, microvillus velocity, and rates for binding and dissociation reactions are then evaluated given the new configuration. This process is repeated until the final simulation time point is reached.

Methods: Parameterization of dissociation rates

Table D2: Parameterization of TCR lifetime data

	k_0 $(1/s)$	f_0 (pN)	k_c $(1/s)$	f_c (pN)	k_s $(1/s)$	f_s (pN)
OVA	—	—	4.241	3.150	0.374	9.280
VSV8	—	—	40.00	2.286	0.050	9.413
slip	2.514	5.533	—	—	—	—
strong slip	0.303	5.533	—	—	—	—

Functional form of V_{MV}

Results obtained with different forms of V_{MV} are shown in Fig. D.12. We considered two variations of the velocity profile used in the paper. In the first, we increased and decreased the value of the force threshold f_{MV} by a factor of two. Increasing the threshold decreases the height of the peak near 0 μm/min in the 100% VSV8 system, while narrowing and shifting the range of observed velocities toward V_0 in the 100% slip pMHC case. Similarly, decreasing the threshold increases the height of the peak near 0 μm/min in the 100% VSV8 pMHC system, while broadening and

shifting the range of observed velocities toward a lower velocity in the 100% slip pMHC case. Because the peak lifetime of OVA occurs at a lower value of the force and for VSV8, decreasing f_{MV} would lead to systems with OVA behaving more like VSV8 in the paper.

We also considered velocity profiles with a Hill-like (sigmoidal) form:

$$V_{MV} = V_0 \left(\frac{1}{1 + \left(-f_x / F_{MV} \right)^{n_H}} \right) \tag{4}$$

for $f_x < 0$ and $V_{MV} = V_0$ for $f_x > 0$. Here, F_{MV} is the Hill reference force, n_H is the Hill exponent, and the microvillus velocity is constrained between 0 and V_0. Figure D.12 shows results from simulations of systems containing nonstimulatory pMHC, OVA pMHC, and VSV8 pMHC. We considered values of $F_{MV} = 25$ pN and $n_H = 4$. For both OVA and VSV8, the distributions of velocities are similar given a linear or Hill-like velocity function. However, the distribution of velocities for nonstimulatory pMHC has a significant peak near V_0 with the Hill function. This is consistent with the net horizontal forces on the microvillus tip being typically less than 25 pN. Thus, the Hill function results in an even more pronounced impact of catch bonds due to the inability of nonstimulatory ligands to significantly slow the microvillus tip on their own.

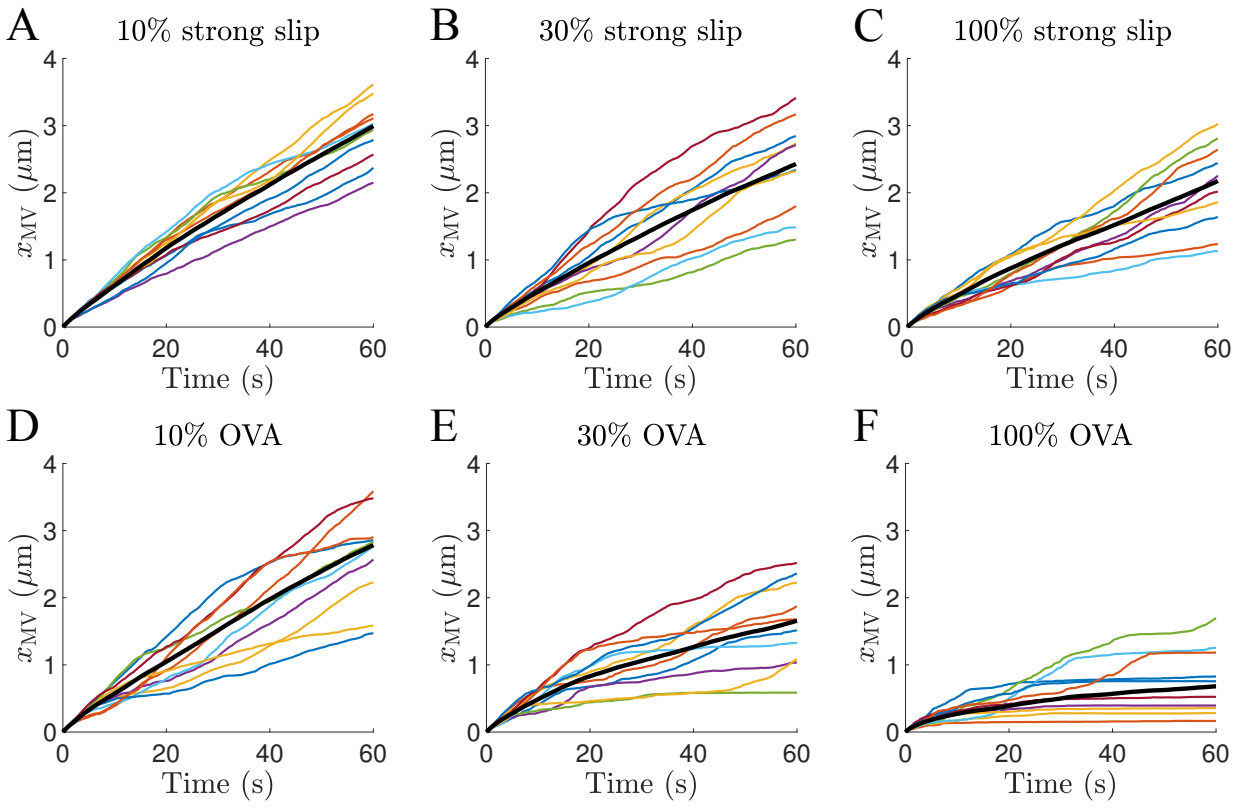

Figure D.9: Displacements of microvilli for different fractions of strong-slip (A - C) and OVA (D - F) pMHC. Black lines show the average microvillus displacement calculated from 25 independent trajectories. Colored lines show the displacement of individual microvilli (10 shown).

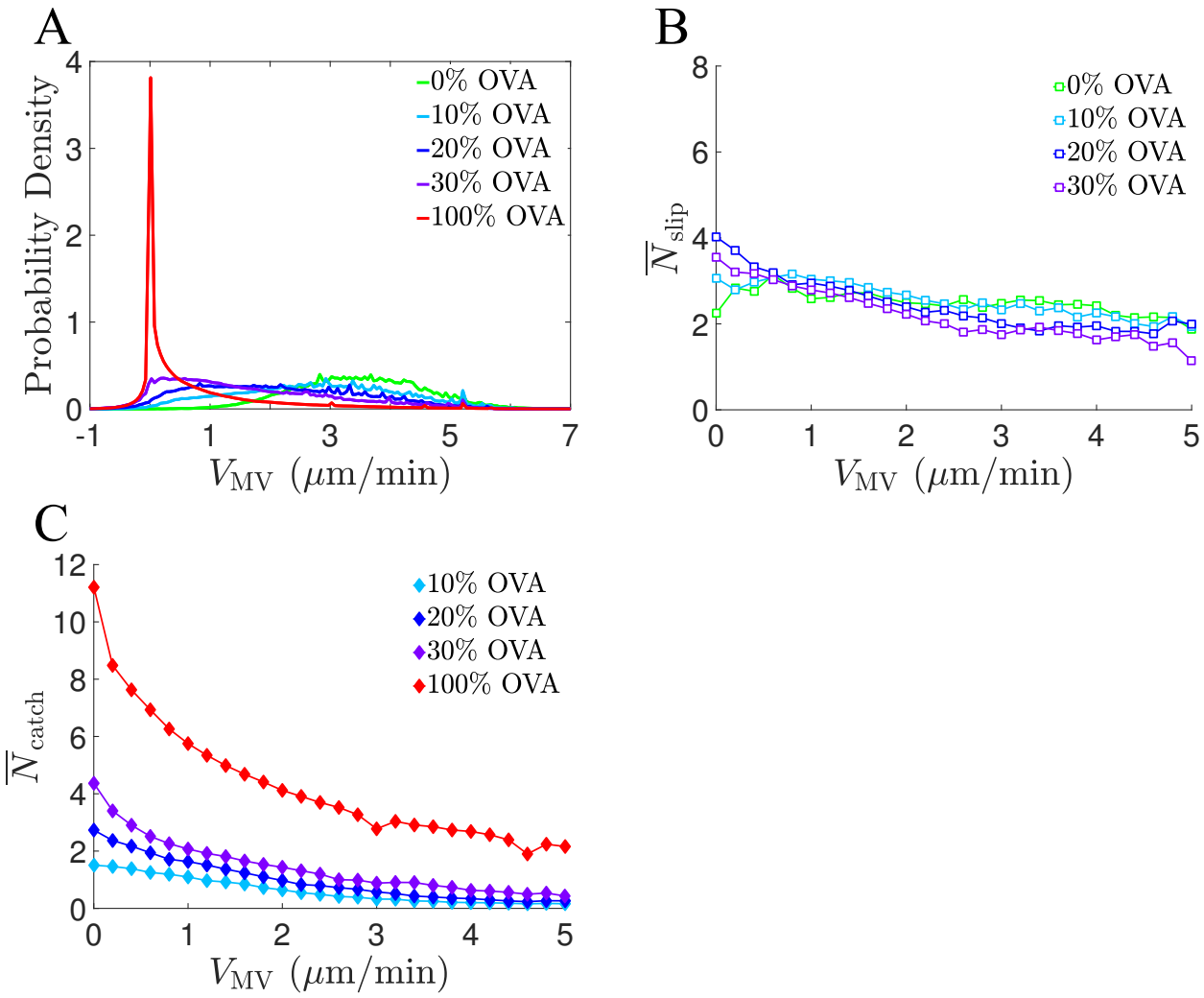

Figure D.10: (A) Probability density of the microvillus velocity at various fractions of OVA pMHC. (B, C) The average number of slip and catch bonds as a function of the microvillus velocity for the OVA system.

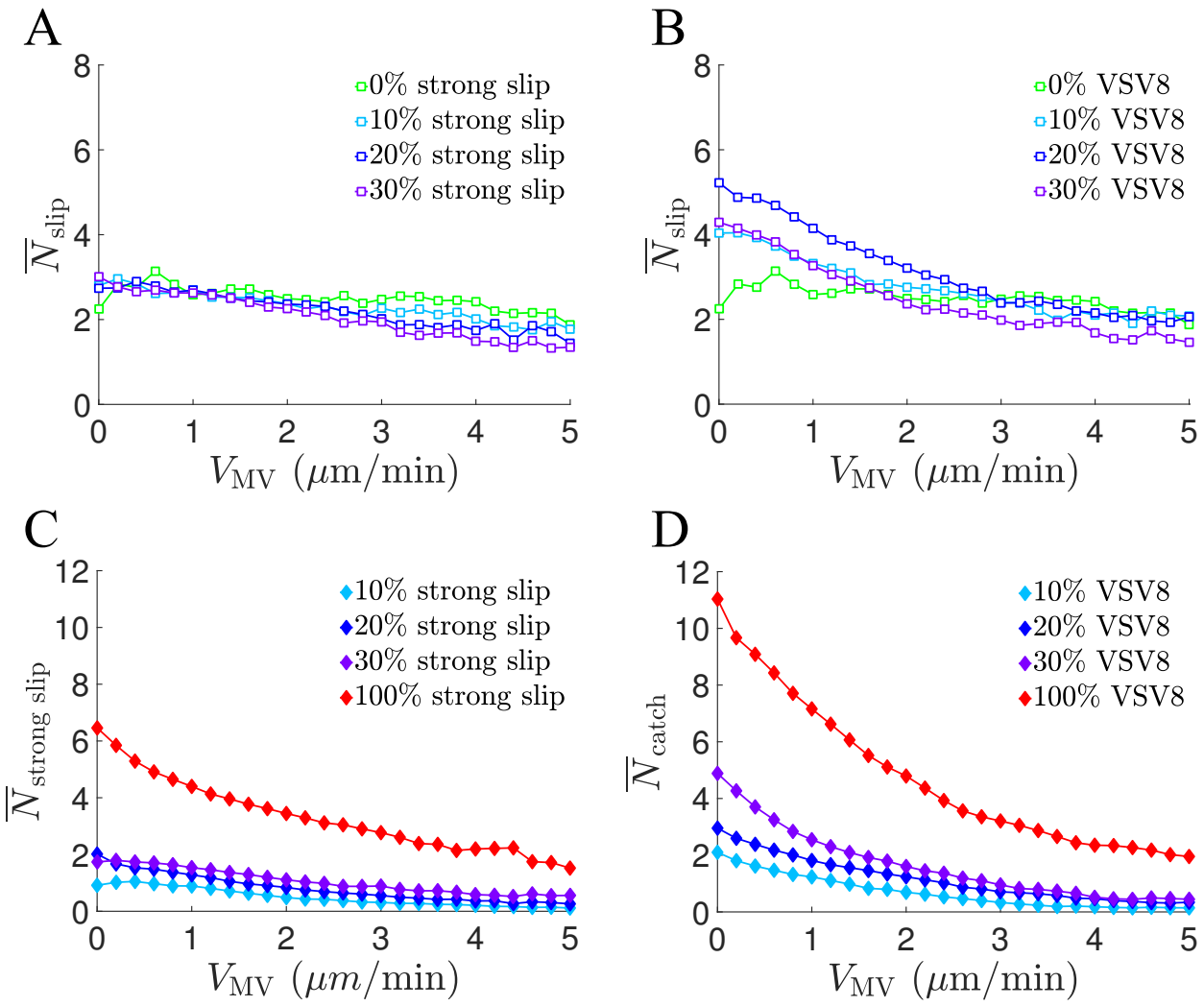

Figure D.11: (A, B) The average number of nonstimulatory slip bonds as a function of the microvillus velocity for varying fractions of strong-slip and VSV8 pMHC. (C, D) The average number of strong-slip and catch bonds for the same systems.

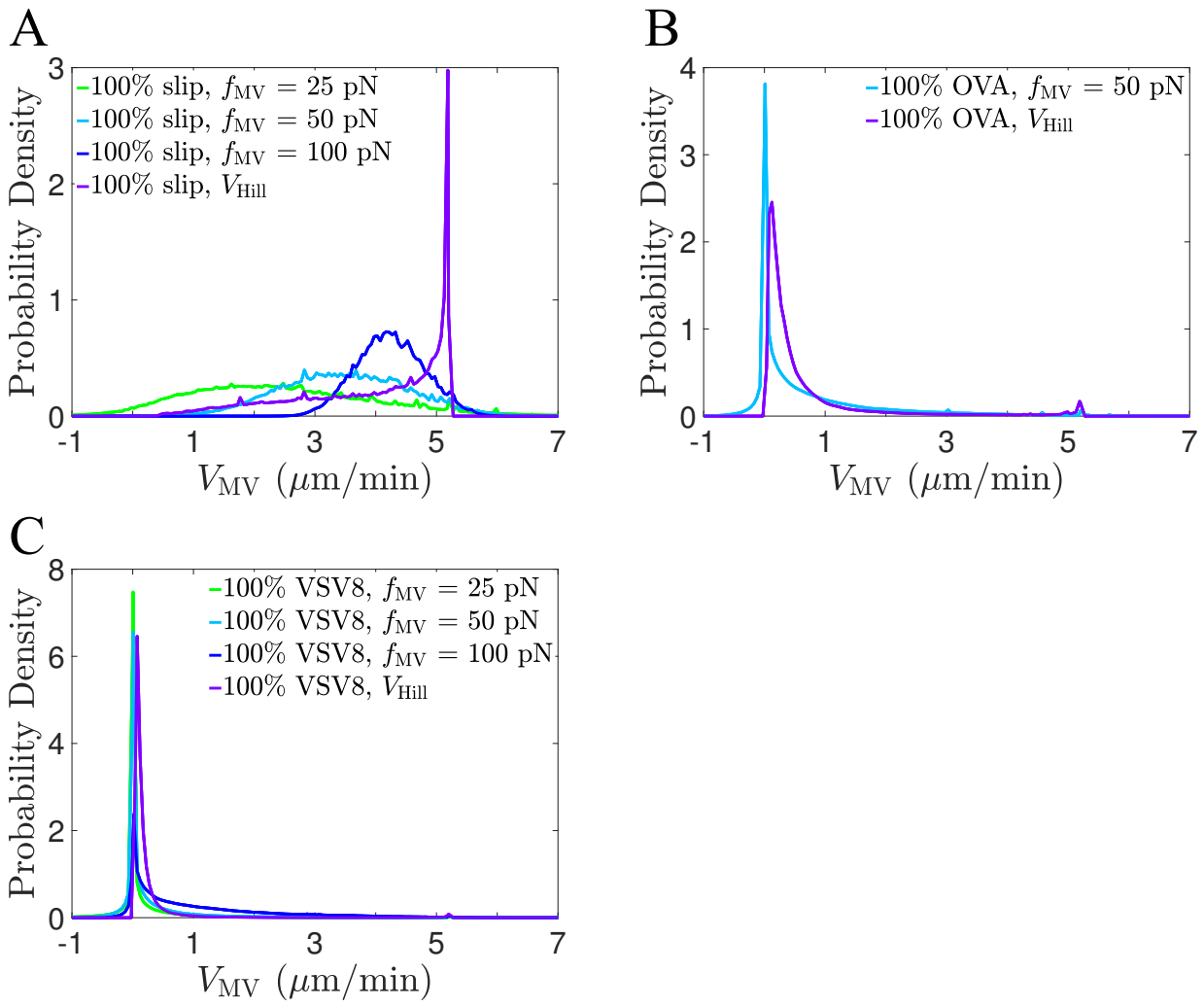

Figure D.12: Characterization of the velocity distribution for different forms of V_{MV} with 100% slip (A), 100% OVA (B), and 100% VSV8 (C). The linear response is considered with $f_{\mathrm{MV}} = 25$ pN and 100 pN (compared with $f_{\mathrm{MV}} = 50$ pN in the main text). The Hill-like response is considered with $F_{\mathrm{MV}} = 25$ pN and $n_{\mathrm{H}} = 4$.

Table D3: Average ± SD for the microvillus velocity, bond lifetimes, and number of bonds for systems with VSV8 (A), OVA (B), and strong slip (C). All values are calculated from 25 independent trajectories.

A		0% VSV8	10% VSV8	20% VSV8	30% VSV8	100% VSV8
V_{MV} (μm/min)		3.486 ± 1.030	2.232 ± 0.781	1.346 ± 0.555	0.948 ± 0.426	0.230 ± 0.083
τ (s)	slip	0.117 ± 0.110	0.141 ± 0.157	0.167 ± 0.193	0.178 ± 0.213	—
	catch	—	0.712 ± 1.022	0.671 ± 1.153	0.549 ± 1.261	0.417 ± 1.045
N_{bonds}	slip	2.361 ± 1.452	2.866 ± 1.811	4.037 ± 2.540	3.568 ± 2.116	—
	catch	—	0.804 ± 0.901	1.837 ± 1.446	3.316 ± 2.467	10.255 ± 3.890

B		0% OVA	10% OVA	20% OVA	30% OVA	100% OVA
V_{MV} (μm/min)		(see above)	2.785 ± 0.862	2.148 ± 0.668	1.658 ± 0.521	0.681 ± 0.313
τ (s)	slip	—	0.127 ± 0.128	0.140 ± 0.149	0.153 ± 0.170	—
	catch	—	0.445 ± 0.355	0.475 ± 0.402	0.530 ± 0.500	0.603 ± 0.614
N_{bonds}	slip	—	2.448 ± 1.540	2.498 ± 1.652	2.542 ± 1.719	—
	catch	—	0.514 ± 0.693	1.098 ± 1.114	1.978 ± 1.837	8.541 ± 4.507

C		0% strong slip	10% strong slip	20% strong slip	30% strong slip	100% strong slip
V_{MV} (μm/min)		(see above)	2.993 ± 0.880	2.738 ± 0.852	2.430 ± 0.787	2.176 ± 0.651
τ (s)	slip	—	0.122 ± 0.118	0.127 ± 0.128	0.133 ± 0.138	—
	strong slip	—	0.384 ± 0.263	0.414 ± 0.310	0.439 ± 0.342	0.466 ± 0.366
N_{bonds}	slip	—	2.179 ± 1.372	2.128 ± 1.378	2.077 ± 1.392	—
	strong slip	—	0.364 ± 0.601	0.694 ± 0.845	1.052 ± 0.982	3.479 ± 2.011

E Dynamics of EphA2 receptor clustering: Tables and Figures

Table E1: EphA2 model variables and parameters. PS denotes parameter sweep.

Variable	Definition	Value	Units	Source
D_{M}	Diffusion coeff. of EphA2 monomer and TYPE7 peptide	0.30	$\mu\mathrm{m}^2/s$	(4)
D_{D}	Diffusion coeff. of all dimers	0.18	$\mu\mathrm{m}^2/s$	(4)
$k_{\mathrm{I}}^{\mathrm{on}}$	Binding rate of the inactive interface	5×10^{-4}	$\mu\mathrm{m}^2/s$	(67)
$k_{\mathrm{I}}^{\mathrm{off}}$	Off-rate of the inactive interface	0.05	s^{-1}	(67)
$k_{\mathrm{A}}^{\mathrm{on}}$	Binding rate of the active interface	1×10^{-3}	$\mu\mathrm{m}^2/s$	PS
$k_{\mathrm{A}}^{\mathrm{off}}$	Off-rate of the active interface	20	s^{-1}	PS
$k_{\mathrm{C}}^{\mathrm{on}}$	Binding rate of clusters	0.05	$\mu\mathrm{m}^2/s$	PS
$k_{\mathrm{C}}^{\mathrm{off}}$	Off-rate of clusters	2×10^{-3}	s^{-1}	PS

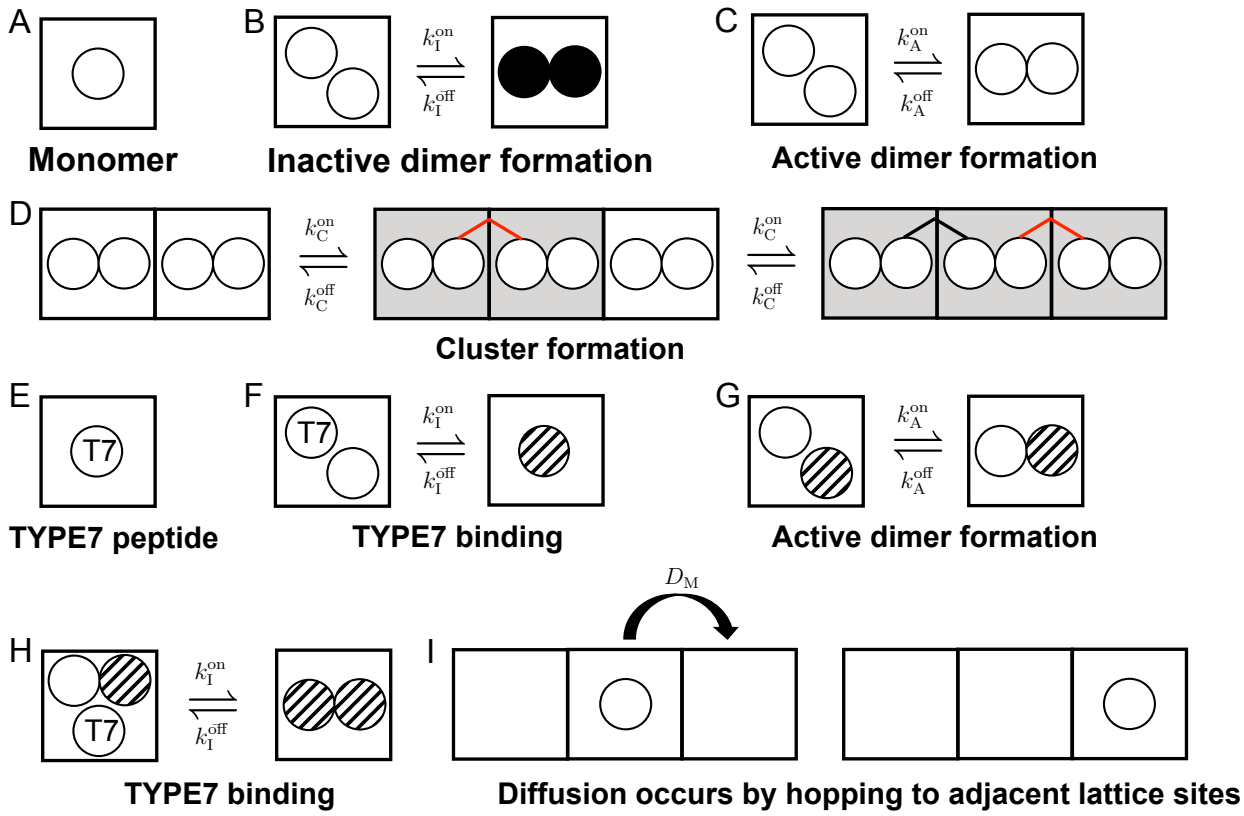

Figure E.1: Chemical species and binding interactions in the computational model. The EphA2 particle (monomer) has two binding surfaces that allow it to participate in dimer formation. Dimers that reversibly bind via the inactive interface (black) of the monomer cannot form larger aggregates. Dimers that reversibly bind via active monomer interface can participate in cluster formation. Cluster formation starts when two active dimers occupy adjacent lattice sites (red linker). TYPE7 binds to monomers via the inactive interface while leaving the active interface available for dimerization. Particles diffuse by hopping to neighboring lattice sites at a rate proportional to the diffusion coefficient.

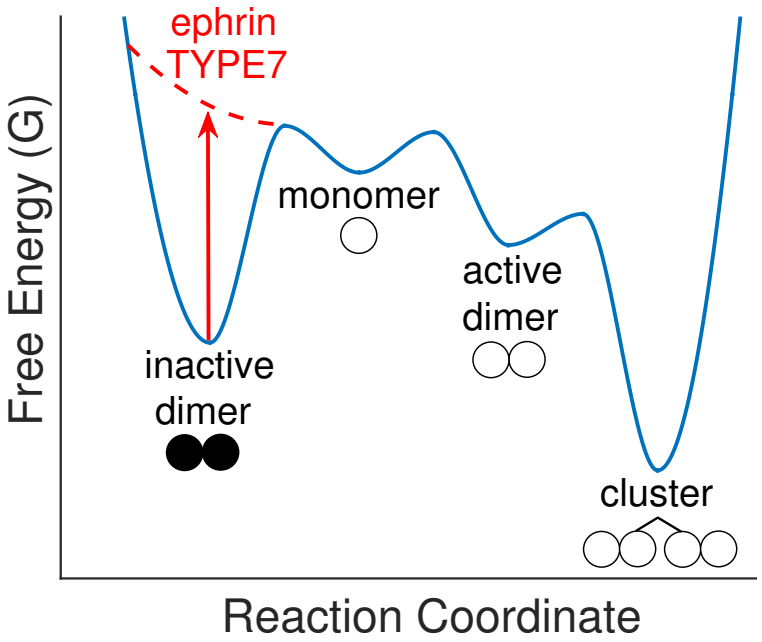

Figure E.2: EphA2 receptor clustering reaction coordinate diagram. This diagram relates the free energies of dimerization at the inacative and active interfaces as well as the free energy associated with the cluster reaction. Ephrin-A1 abrogrates the reaction via the inactive interface and thus forces the monomer to transition to the active dimer state.

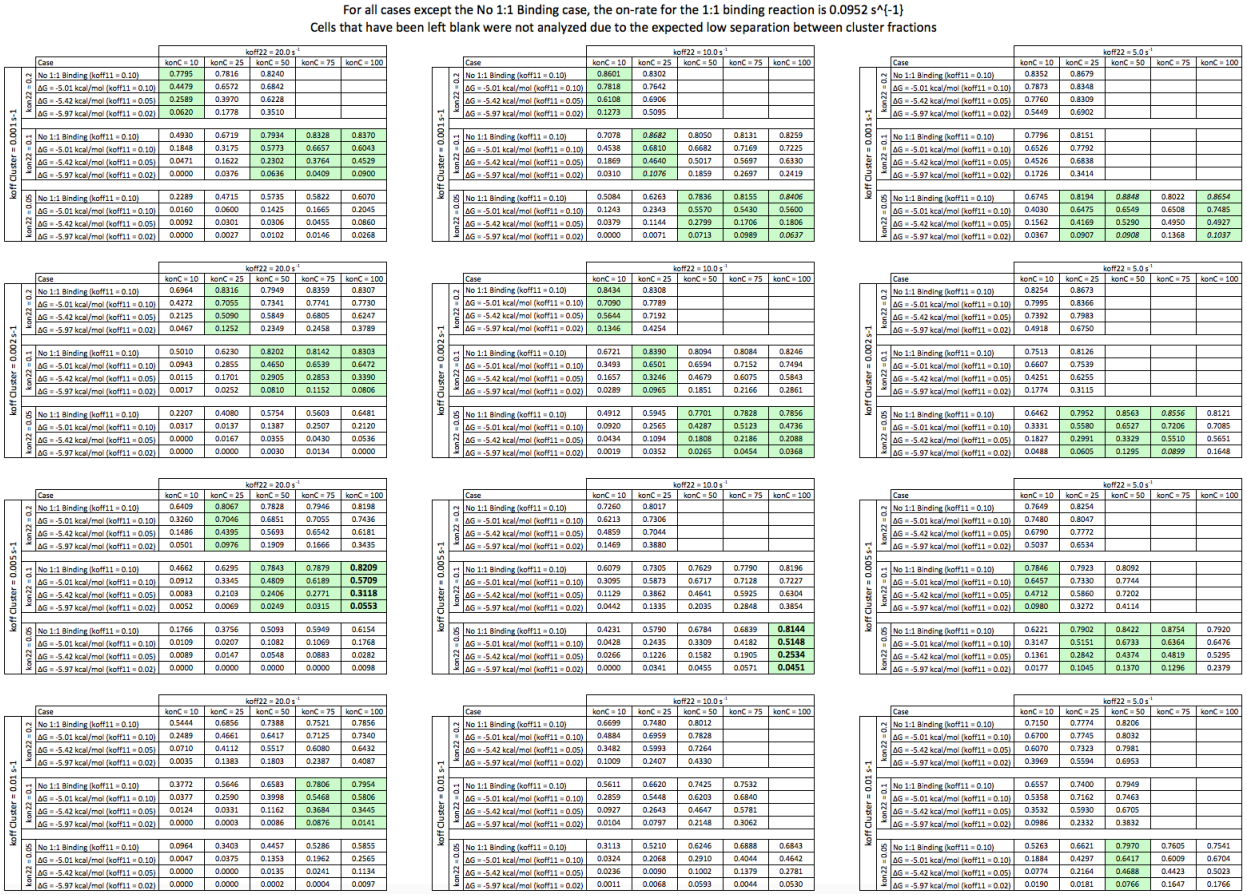

Figure E.3: Kinetic parameter sweep. This subset of the parameter sweep shows the average cluster fraction at a given parameter set after running one hundred independent trajectories. A desirable kinetic parameter set has a large difference in the cluster fraction between the TYPE7 = 0 and Ephrin cases (system limits). Cases that show significant differentiation between the two limits are highlighted in light green.

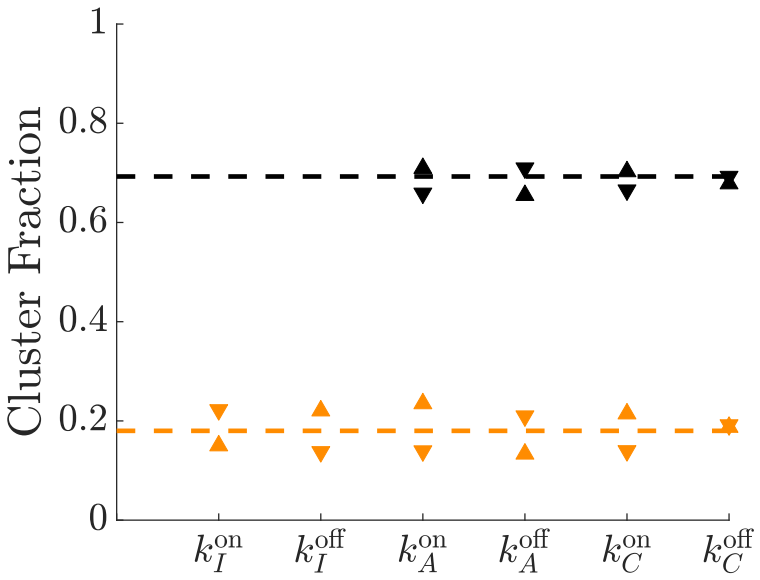

Figure E.4: Sensitivity analysis. Analysis was performed observing changes of cluster fraction that occur when parameters are varied. Triangle symbols correspond to the sensitivity analysis and correspond to results when increasing (upward triangle) or decreasing (downward triangle) a kinetic parameter by ten percent of its original value. The dashed lines represent the cluster fraction obtained using the parameters in the table. The black line gives the cluster fraction when ephrin-A1 is present, and the orange line gives the final cluster fraction without ephrin-A1 or TYPE7. Each result corresponds to the average of one hundred independent trajectories.

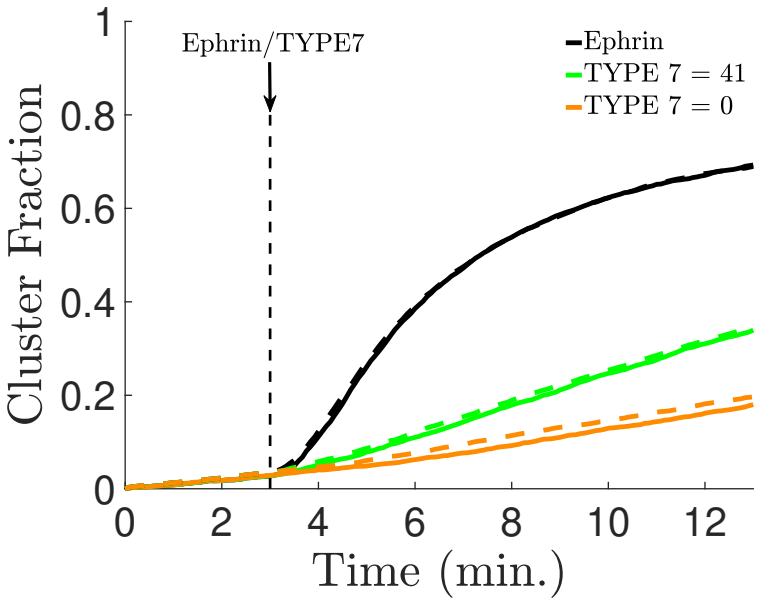

Figure E.5: Characterization of the effect of system size. We show the average cluster fraction of one hundred independent trajectories for the conditions considered in our study (solid lines) and for a system twice the size (dashed lines). The black vertical line at 3 minutes indicates the time at which TYPE7 peptides or ephrin-A1 ligands are introduced into the system. Doubling the system size does not significantly change the average cluster fraction for a given TYPE7 peptide density.

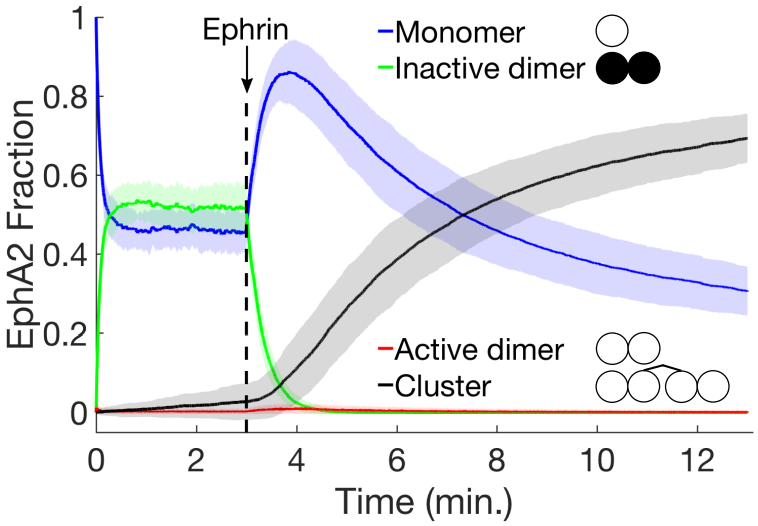

Figure E.6: Time-dependent chemical species fractions given the presence of ephrin-A1. The average chemical species fraction $\pm$ S.D. of each chemical species are shown. The black vertical line at 3 minutes indicates the time at which ephrin-A1 ligands are introduced into the system. Each result corresponds to the average of one hundred independent trajectories.

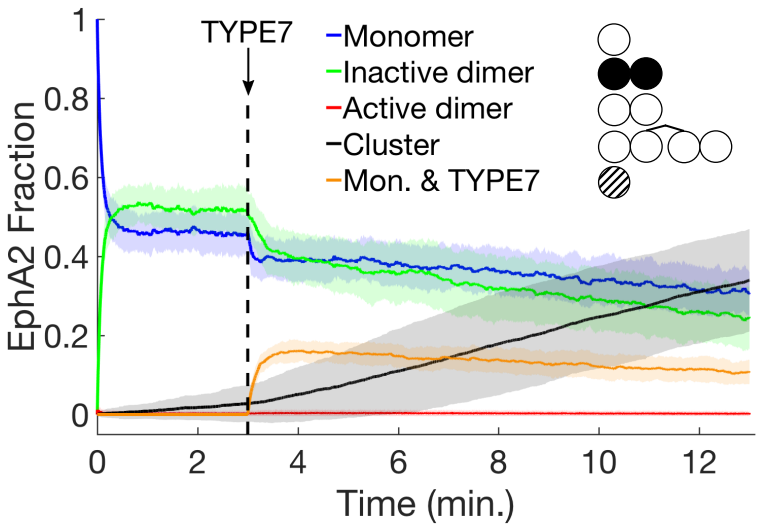

Figure E.7: Time-dependent chemical species fractions given the a TYPE7 peptide density of 41 molecules/μm^2. The average chemical species fraction $\pm$ S.D. of each chemical species are shown. The lack vertical line at 3 minutes indicates the time at which ephrin-A1 ligands are introduced into the system. Each result corresponds to the average of one hundred independent trajectories.

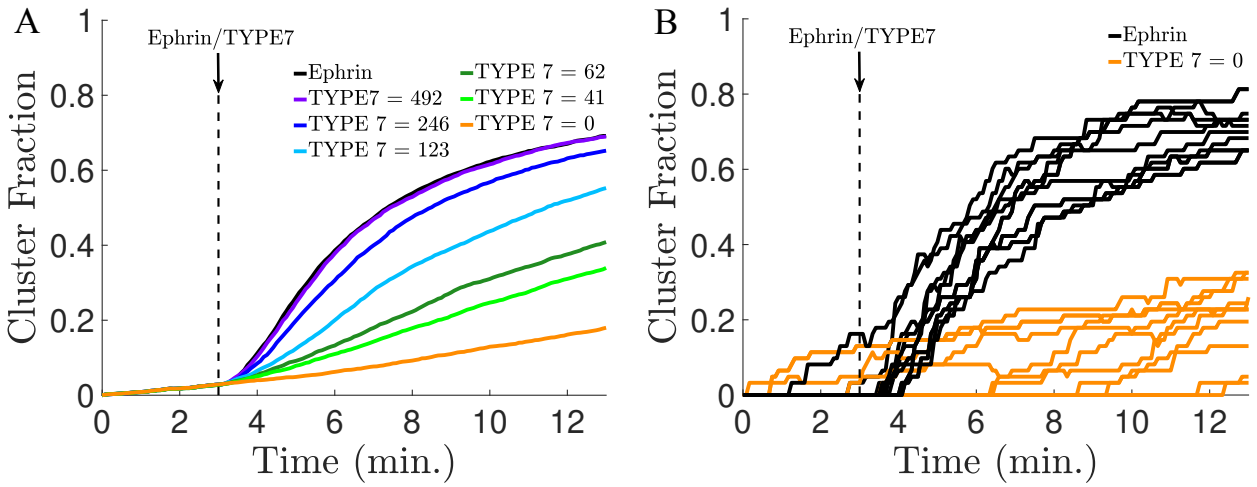

Figure E.8: EphA2 receptor clustering is dependent on the number of TYPE7 peptides present in the system. (A) Average cluster fractions as a function of time and TYPE7 peptide number. Averages were obtained from one hundred independent trajectories. (B) Time-dependence of cluster fractions for individual trajectories. The black vertical line at 3 minutes indicates the time at which TYPE7 peptides or ephrin ligands are introduced into the system. There is significant variation between individual trajectories at lower TYPE7 peptide densities due to the stochastic nature of the model.

Vita

Robert Henry Pullen, III was born in Atlanta, Georgia on June 3, 1991. At the age of 5, his family moved to New Market, MD where they would spend the next 17 years. After graduating from Linganore High School, he attended the University of Maryland, College Park in the Fall of 2009. He received his Bachelor of Science degree in Chemical Engineering in May 2013. In August of 2013, he came to the University of Tennessee and joined the research group of Prof. Steve Abel. In May 2015, he earned a Master of Science degree in Chemical Engineering concurrently during the doctoral program. His doctoral research focused on the biophysical modeling of interactions at the interface of T cells with target cells.